TNO

TU Delft

Stealth fiducial markers

Enhancing re-detection efficacy of defects on blank wafers

M. A. J. Bouwens

Stealth fiducial markers

Enhancing re-detection efficacy of defects on blank wafers

by

M. A. J. Bouwens

to obtain the degree of Master of Science
at the Delft University of Technology,
to be defended publicly on Monday November 2, 2015 at 01:00 PM.

Student number:	1508571	
Project duration:	January 19, 2015 – November 2, 2015	
Thesis committee:	Dr. P. F. A. Alkemade,	TU Delft, supervisor
	Prof. Dr. H. P. Urbach,	TU Delft
	Dr. G. A. Steele,	TU Delft
	Dr. ir. P. van der Walle,	TNO

An electronic version of this thesis is available at http://repository.tudelft.nl/.

TNO innovation for life

TU Delft Delft University of Technology

Abstract

In this thesis a stealth fiducial marker system for blank wafers is designed, fabricated and validated. The goal of this marker system it to map the coordinates of TNO's Rapid Nano (a fast optical inspection tool) to the coordinates of scanning electron microscopes and atomic force microscopes. This way defects, that have been detected in the Rapid Nano, can be re-detected with a higher efficacy in the scanning electron microscope or atomic force microscope for further study.

To develop the fiducial marker system, firstly a list of requirements for the markers and the marker system was drafted. To this end, experts on all three platforms were interviewed and previously tried fiducial markers for these platforms were studied. Also a Monte Carlo simulation was performed, to study the error propagation in the positioning accuracy of the markers and defects.

The list of requirements led to a design for the fiducial marker system. Multiple fiducial markers are spread across the blank wafer. Each marker has a unique shape, so they can be distinguished from one another. The design of the markers provides information about the position and orientation of the marker at a glance. Once a single marker is found, it is easy to locate the other markers.

The material and the height of the markers was optimised with finite element (COMSOL) simulations and experiments. The optimised fiducial markers are very visible in bright field, and almost invisible ("stealth") in optical dark field, the microscopy mode that is used in TNO's Rapid Nano. This results in markers that are are well-visible and accurately localisable in (dark-field) optical microscopy, scanning electron microscopy and atomic force microscopy.

The fiducial marker system was fabricated with e-beam lithography, evaporation of gold/platinum and lift off. The functioning of the fiducial marker system was validated by re-detecting programmed defects that have been mapped by the Rapid Nano.

The fiducial marker system greatly enhances the re-detection rate of defects. Without fiducial marker system a re-detection rate of 50% is considered challenging, but in the experiments with the fiducial marker system 100% of the programmed defects were re-detected on both a scanning electron microscope and the atomic force microscope. In fact, if the fiducial marker system is used, only one standard SEM (7x7 μm^2) image per particle is needed to comply with the ITRS requirement on re-detection probability for particles down to 70 nm.

The experimental results on the scanning electron microscope are in agreement with the results from Monte Carlo simulations on the propagation of inaccuracy in the position of markers/defects. The atomic force microscope performs worse than expected, because the stage precision in the used AFM model is worse than specified by the manufacturer.

The requirements on contamination, used materials and lifetime of the markers are not met. In a next design for the fiducial marker system, lift off should be avoided as a fabrication method. It proved very difficult to find a suitable material for the markers that is compliant with standards from the semiconductor industry. Therefore it should also be investigated if the markers are still visible enough in optical and scanning electron microscopes, if the contrast between the marker and the silicon substrate is only provided by topographical contrast. In this case, no "prohibited" material has to be used and the lifetime of the fiducial marker system would improve at the same time.

During the finite element analysis in COMSOL, a peculiar property of the scattering in the Rapid Nano was discovered: Two opposing edges of a fiducial marker scatter differently. The asymmetry was confirmed with experimental data. This effect could potentially be used for advanced defect classification in the Rapid Nano.

Acknowledgements

In January 2015 I started with my graduation research at TNO. I cannot believe it has already come to an end. I have learned so much during this project and so many exciting things have happened, like being a co-author of my very first paper and presenting my work at the Micro- and Nano-Engineering conference. All in all, I could not have been happier with my project and it feels great to finish my Master studies on this note. This project certainly would not have been such a success without the support I received from many, both at TNO and at the TU Delft:

I would like to start by thanking Paul Alkemade, my supervisor at the TU Delft, and Peter van der Walle, my supervisor at TNO. Thank you for your guidance during this project. I would not have been able to complete this thesis without our discussions and your feedback.

All my colleagues at the Nano-Instrumentation group made my time at TNO unforgettable. I would like to specifically thank two colleagues that worked closely with me on this project: Diederik Maas and Jacques van der Donck. Thank you for all the great advice, both project related and otherwise.

Ruud Schmits and Hans van den Berg have often helped me in the clean room. Their experience with nano-fabrication was really valuable: Their directions have saved me from having to re-invent the wheel many times.

All the members of the Kavli NanoLab group have really helped me find my way in the Van Leeuwenhoek Laboratory. They were always prepared help out and to discuss the problems I encountered during the fabrication of my samples. A special word of thanks to Gaurav Nanda, my clean room mentor, for learning me all the tricks of the trade and for all the fun times in the clean room. And also to Anja van Langen-Suurling, for fabricating one final sample for me, during the last stage of my thesis when I was too busy writing this report.

I owe much to the experts on all the imaging platforms, who were willing to be interviewed by me and who taught me how to operate the different machines: Emile van Veldhoven and Hozanna Miro on the scanning electron microscope, Maarten van Es on the atomic force microscope and, again, Peter van der Walle on the Rapid Nano.

Durk de Vries from COMSOL has supported me with the development of my model. His explanations and suggestions were always very clear and useful.

Paul Urbach and Silvania Pereira, from the Optics section at the TU Delft, have answered all my question regarding the optical theories.

Finally I would like to thank my parents, who have always supported and encouraged me to make the most out of my studies. And my boyfriend: Thank you Michiel, for always being there for me. You are the best partner I could wish for.

Maryse Bouwens
Delft, November 2015

Contents

1 Introduction

1.1. Research context

Following Moore's law, chips have and will continue to shrink in size [17]. This can be noticed in e.g. mobile phones and computers: As the years progress, these devices are becoming smaller, faster and more powerful. Today, state of the art chips have a critical dimension of 14 nm [4]. On such a small scale, a very small particle can already lead to a malfunctioning chip, for example by shorting a circuit. In fact, particle defects on masks and wafers are among the main contributors to yield loss in semiconductor manufacturing [10, sec. 2.2].

To minimise the particle contamination, chips and other nano-structures are fabricated in a "clean-room": As the name suggests, this is a very clean and almost dust-free environment. Despite these efforts some contamination can still occur. If it does, the particle defects need to be characterised. Properties of interest are, e.g.: size, shape and material of the particle. The characterisation aids to determine the origin, such that future defects can be avoided. Tools and processes are often qualified on particle cleanliness using blank substrates (masks or wafers), also known as "blanks", as witness samples [28]. To pass the cleanliness test, particle defects must occur at ultra-low densities. Typically, only a single particle may be added during every 100 or 1000 cycles in a tool.

Because of this low density and their small size, finding a particle for analysis is very difficult. It is comparable to finding a golf ball on a homogeneous and flat area as big as the Netherlands. Hence fast optical inspection techniques are in use, that are capable of scanning sufficiently large areas in a reasonable inspection time [19, 23, 24]. TNO has developed such an optical inspection system, the RapidNano3, which can detect particles down to 42 nm in diameter on substrates up to 150 mm in diameter [31].

Optical inspection detects defects, but offers no detailed information on the defect shape nor composition. To characterize a defect, further analysis at a much higher spatial resolution is needed. The defects can be classified using their attributes as measured by e.g. scanning electron microscopy (SEM) or atomic force microscopy (AFM). However, these techniques are much slower and have a very small field of view, and perhaps most important: They require the substrate to be transferred into another tool, hence losing the absolute position information of the defects. This loss of position information means that re-detection of the defects is not trivial; for the smallest defects, a re-detection success rate of 50% is considered challenging [10, Table 7]. An accurate translation of the defect map from the optical inspection to the stage coordinate system of the SEM or AFM is needed to meet this challenge.

For this purpose fiducial markers on a sample can be used. The coordinate transformation can be performed with the position of these markers in both the optical dark field and the local inspection tools. Fiducial markers are not yet used on blanks, because it is not trivial to design a marker that is easy to find *and* accurate in location on all three systems. The difficulties lie in the very different field of view and detection mechanism of each system. TNO has made some attempts to create these markers, but so far they have not been successful in meeting all requirements. These previously tried markers will be discussed in Chapter 3 of this report.

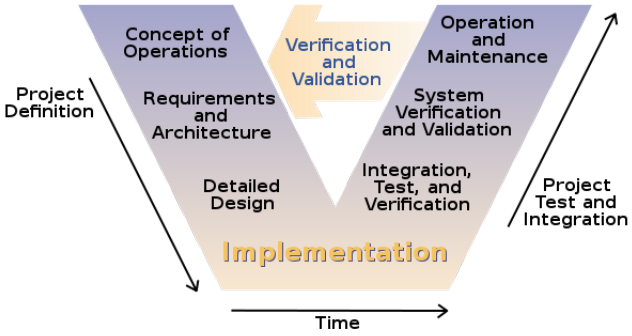

Figure 1.1: The research approach during this project is represented by the V-model. This model is often used in systems engineering processes. First the project is verified, then implemented and finally it is validated. Image source: Wikipedia.

1.2. Research objective

The objective of this Master thesis is to design, fabricate and validate a fiducial marker system for blanks that can be used in TNO's Rapid Nano, scanning electron microscopes, ánd atomic force microscopes.

1.3. Research approach

To develop the fiducial marker system the verification and validation model (V-model) approach was used. This model describes a systems engineering process. (See Fig. 1.1). The V-model consists of a sequential path of processes: The first step is to gain a concept of operations, from which a list of requirements is drafted, which leads to a design. This part is also referred to as the verification. After the verification the design is implemented. Finally, the implemented design is validated. This process is repeated multiple times, until (in an ideal case) all the requirements are met.

In this work, the familiarising with the concept of operations was accomplished by interviewing experts on all three imaging platforms. Because the position accuracy is an important feature of the fiducial marker system, the error propagation in the position accuracy of the markers and defects was studied with a Monte Carlo simulation. The previously tried fiducial markers for these platforms were also studied.

Using the acquired concept of operations as input, a list of requirements for the markers and the marker system was drafted.

The requirements led to a design for markers that are very visible in bright field, and almost invisible ("stealth") in optical dark field, the microscopy mode that is used in the Rapid Nano. To make the markers more stealth, the scattering of the markers was reduced by optimising the materials and height of the markers with finite element (COMSOL) simulations and experiments.

After the successful fabrication of a sample with markers, the design was validated by re-detecting defects, that have been detected on the Rapid Nano, with a scanning electron microscope and an atomic force microscope.

1.4. Outline of thesis report

The remainder of this thesis is divided in six chapters: Chapter 2 provides background information on the different imaging methods (Dark field microscopy, SEM and AFM), theory on optical scattering and explains the finite element model that was used this thesis.

Chapter 3 gives insight into the systems engineering process that resulted in the design for the fiducial markers. It shows the result of the verification steps in the V-model: The concept of operations, list of requirements and the resulting marker design.

Chapter 4 explains the cleanroom techniques that were used in the fabrication of the markers. (Specific recipes are included in the appendix.) It also describes the used methods for the validation of the markers.

The experimental results are presented and discussed in chapter 5.

The final chapter 6 contains the conclusions of this thesis and recommendations for further research.

2

Theory

2.1. Imaging methods

In order to design markers that will work on all three platforms that need to be coupled, it is important to understand how these imaging systems work. Therefore the working principles of the Rapid Nano (which is based on optical dark field microscopy), scanning electron microscopy (SEM), and atomic force microscopy (AFM) are explained in this section.

2.1.1. Optical dark field microscopy

In dark field microscopy, scattered instead of reflected or transmitted light is used for the imaging of a sample. (See Fig. 2.1.) The reflected and transmitted beams are dumped and the scattered light is viewed against a dark background. Fig. 2.2 shows the difference between a bright- and dark field optical image.

Because only a fraction of the incoming light is actually used for the image, a sample needs to be more strongly illuminated to be visible in dark field, compared to bright field microscopy. If a sample is very delicate, such a high intensity can be damaging to the sample.

As with all optical imaging techniques, the resolution, d, of a dark field image is limited by the diffraction, which depends on the used wavelength of light, λ, and the numerical aperture, NA, of the imaging system:

$$d = \frac{\lambda}{2NA} \tag{2.1}$$

Formula 2.1 is known as the Abbe diffraction limit. The Abbe limit of an imaging system that uses, for example, green light with a wavelength of 500 nm and that has a numerical aperture of 1 is equal to 250 nm.

The **Rapid Nano** (RN) uses dark field microscopy to detect very small particles on flat substrates. The substrates are illuminated with 532 nm laser-light under an angle of 60 degrees with respect to the surface normal. The light is p-polarised at the surface of the substrate to maximise the scattering signal. The scattered light is detected by a charged-coupled device (CCD) camera. (See Fig. 2.3) The numerical aperture of this imaging system is 0.42 [30]. This means that the Abbe diffraction limit of the Rapid Nano (with 532 nm light) is 633 nm.

However, resolution is not the same as sensitivity: The Rapid Nano can *detect* particles much smaller than the diffraction limit, down to 42 nm. The small particles can be seen as sub-resolution point-like radiating sources. These point objects are visible as blurry dots in the image plane. Their intensity profile is referred to as the **point spread function** (PSF). (See Fig. 2.4) Through curve fitting of the PSF, the particle centre can be found with a greater accuracy than the diffraction limit. However, if the distance between two particles is smaller than the diffraction limit, they will not be resolved but instead they will appear as one (bigger) particle.

The achievable localisation accuracy depends strongly on the **signal to noise ratio** (SNR) of the PSF. In the Rapid Nano, the surface roughness of the substrate limits the SNR: The background image looks like a speckle pattern. The variance in this background signal can be reduced by averaging over images taken from different azimuth angles, provided these images have an uncorrelated background

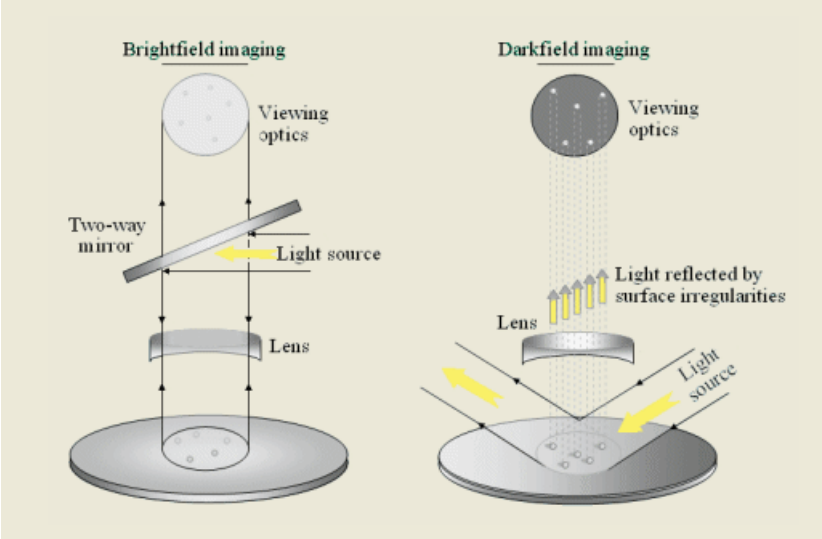

Figure 2.1: A schematic overview of optical bright- and dark field microscopy. In bright field microscopy the reflected light is used for the imaging, while in dark field microscopy the reflected light is dumped and only the scattered light is used. Image source: el-cat.com.

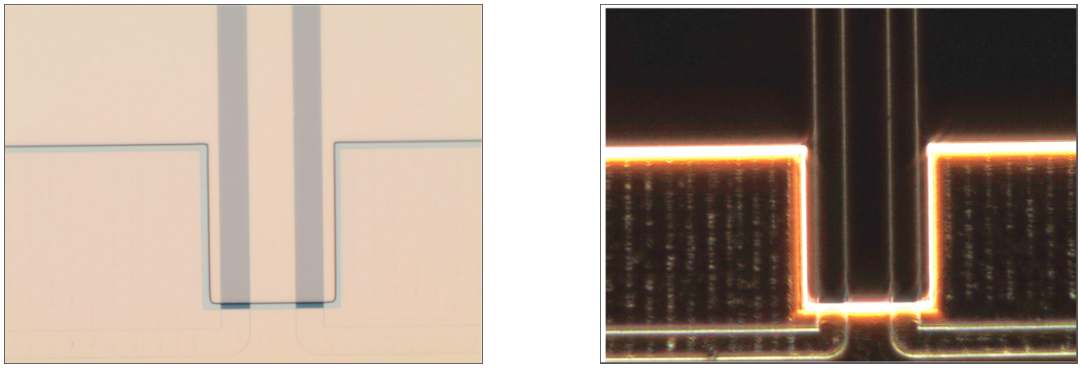

(a) Bright field image

(b) Dark field image

Figure 2.2: An image in optical bright- and dark field, to show the differences between the two. In the dark field image the scattered light is viewed against a dark background. Images source: Nanotechnology lecture slides.

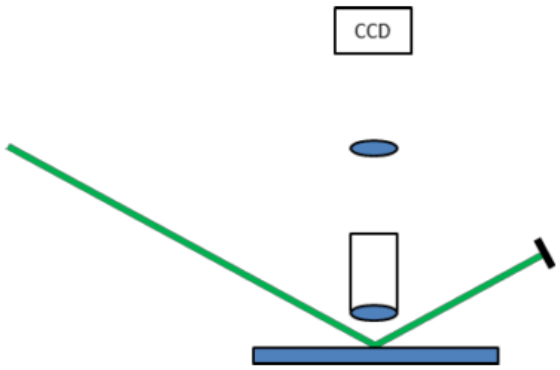

Figure 2.3: The Rapid Nano is a fast inspection tool that uses optical dark field to detect particles on flat substrates. This image shows a schematic overview of the Rapid Nano setup: A laser beam with a wavelength of 532 nm is used to illuminate a substrate under a grazing angle of incidence. The scattered light is detected by a CCD camera. Image source: Van der Walle et al. [30].

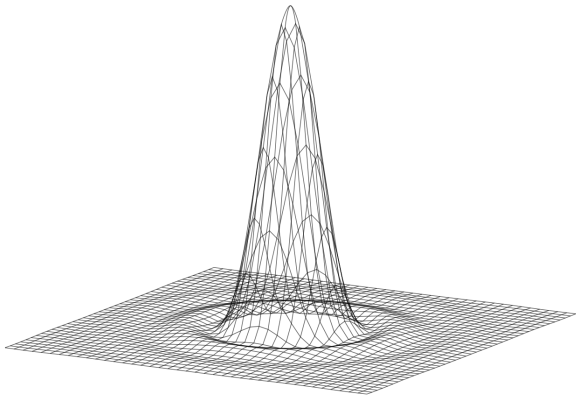

Figure 2.4: Particles that are smaller than the diffraction limit, will appear as blurry dots if they are imaged. Their intensity profile in the image plane is called the point spread function. This image shows a 3D impression of a point spread function. Image source: Wikipedia.

speckle. In the Rapid Nano 9 different azimuthal angles are used to increase the detection sensitivity in this way [30, 31].

The SNR can also be improved by increasing the incoming light intensity: The Rapid Nano can be operated at different laser power levels, ranging from 0.01 to 4.00 W. The higher the used laser power, the smaller the particles that are just visible. However, if a sample is very contaminated or has a high surface roughness, it may not be possible to operate at the highest power because the CCD camera will saturate.

The imaging is based on a step-and-repeat principle: The substrate is moved underneath the imaging system with a precise stage. The stage has a reproducibility of 1–2 micron. After each stage step a Rapid Nano image of approximately 1 square mm is made. These images are stitched together to create an overview image of the entire sample. The measurement time for each individual image is 50 ms. With fast image processing a defect map is created: A list of the detected particles on the substrate with their relative coordinates and sizes [29].

2.1.2. Scanning electron microscopy

Scanning electron microscopy (SEM) uses electrons instead of photons for imaging. The wavelength of electrons is very small, as described by the De Broglie relation, stated in terms of electron energy in volts, V_0:

$$\lambda = \frac{h}{\sqrt{meV_0}} \tag{2.2}$$

Here h is the Planck constant, m and e are the mass of an electron and the elementary charge. A SEM is usually operated at a few to tens of kV. If it is operated at for example 5 kV, this corresponds to an electron wavelength of 0.017 nm. This is much smaller than the wavelength of visible light. A scanning electron microscope also uses a smaller aperture angle (typically 10^{-2} rad) than an optical microscope, but even so the diffraction limit (Eq. 2.1) for a SEM is much smaller. Therefore scanning electron microscopy can achieve a higher resolution than optical microscopy. The resolution of SEM images typically lies between 1 and 20 nm. Because of the small aperture angle, a SEM also has a large depth of focus. Thus, large objects can be imaged with very little loss of resolution [15].

A scanning electron microscope consists of a source of electrons, a condenser lens and an objective lens, all placed inside a high vacuum chamber [15]. The electron source can be a thermionic emission gun or field emission gun. The condenser lens collects the electrons from the source and forms them into a beam. The objective lens focusses this beam into a small spot on the sample. The small spot is usually scanned over the sample in a raster pattern by magnetic deflection coils.

The SEM images can be formed from different signals [15]: (Also see Fig. 2.5)

- **Transmitted electron signal** from electrons that travel through the sample. This only happens if the sample is thin enough. This signal is used in Scanning Transmission Electron Microscopy (STEM).

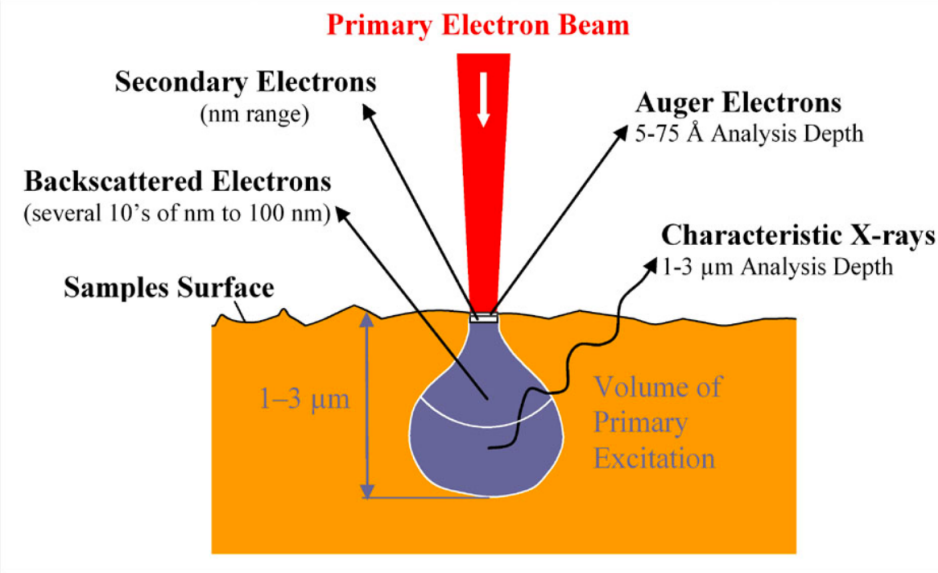

Figure 2.5: In a scanning electron microscope a primary electron beam is scanned over a sample. The primary electrons collide and release other types of electrons in the sample. This image shows the different types of released electrons and their origin. Image source: Nanotechnology lecture slides.

- **Elastically backscattered electrons** in thicker samples can be detected by a detector placed above the sample. The amount of backscattered electrons depends on the composition of the sample: heavier materials produce more backscattering. (See Fig. 2.6)

- **Inelastically scattered electrons**, also known as secondary electrons. They are excited from the sample by the incident beam, but due to inelastic scattering they return with a lower energy than the elastically backscattered electrons. They are collected using an energy resolving detector. The secondary electrons mostly originate from the surface of the sample. This explains the so-called edge-effect: More secondary electron can leave the sample at an edge, leading to increased brightness there. (See Fig. 2.7)

- **X-ray emission** from core electrons, which occurs if the incident electron beam is energetic enough. By using an energy sensitive X-ray detector the atomic composition of the sample can be mapped at very high resolution. This is called Energy-Dispersive X-ray spectroscopy (EDX). This technique uses the fact that each element has a unique X-ray emission spectrum. Because the origin of the X-rays is not from the surface, but from the bulk of the sample, it is difficult to determine the composition of a single small particle on the substrate with this technique.

These different signals give rise to different types of contrast in a SEM image. Figure 2.8 shows some examples.

2.1.3. Atomic force microscopy

In atomic force microscopy (AFM) a surface is scanned with a flexible cantilever that has a sharp tip. (See Fig. 2.9) An optical deflection scheme is used to monitor the bending of the force sensing cantilever: Light from a small diode laser is focused on to the back side of the cantilever and reflected onto a two-segment photo diode. (See Fig. 2.10) The deflection of the beam, δz, is measured by comparing the signal from the segments:

$$\delta z \propto \frac{i_A - i_B}{i_A + i_B} \tag{2.3}$$

A deflection of smaller than one part in a million of the cantilever length is already detectable: This results in sub-nanometre sensitivity in the z-direction. The limit on the smallest detectable signal lies in the thermal excitation of the cantilever [15].

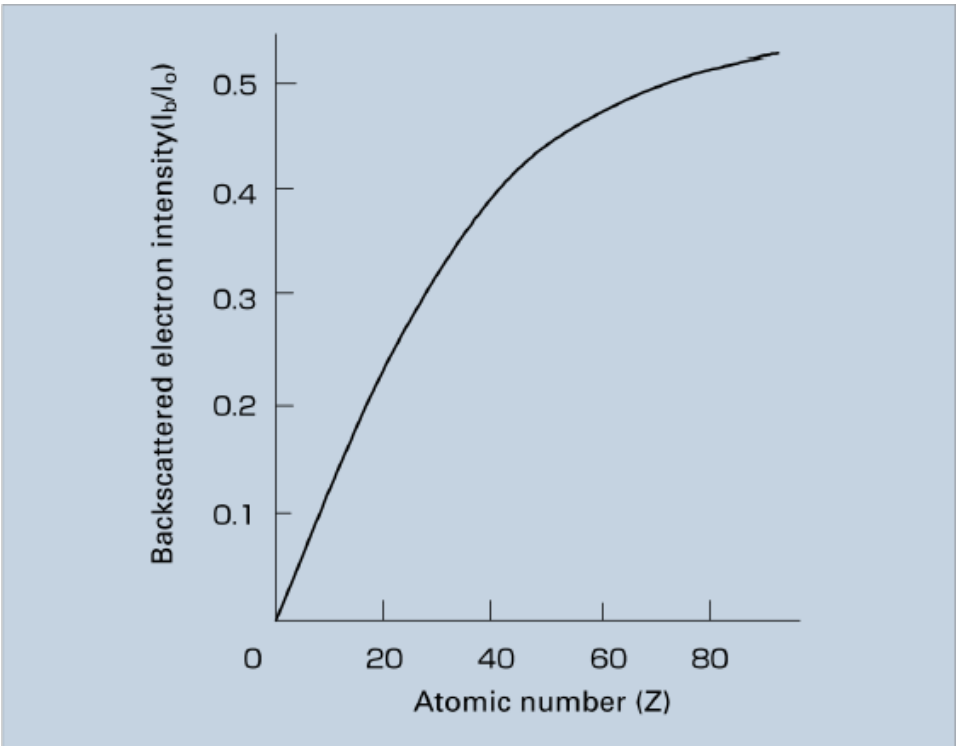

Figure 2.6: The amount of backscattered electrons depends on atomic number of the material: The heavier the material, the higher the intensity of backscattered electrons. Image source: Nanotechnology lecture slides.

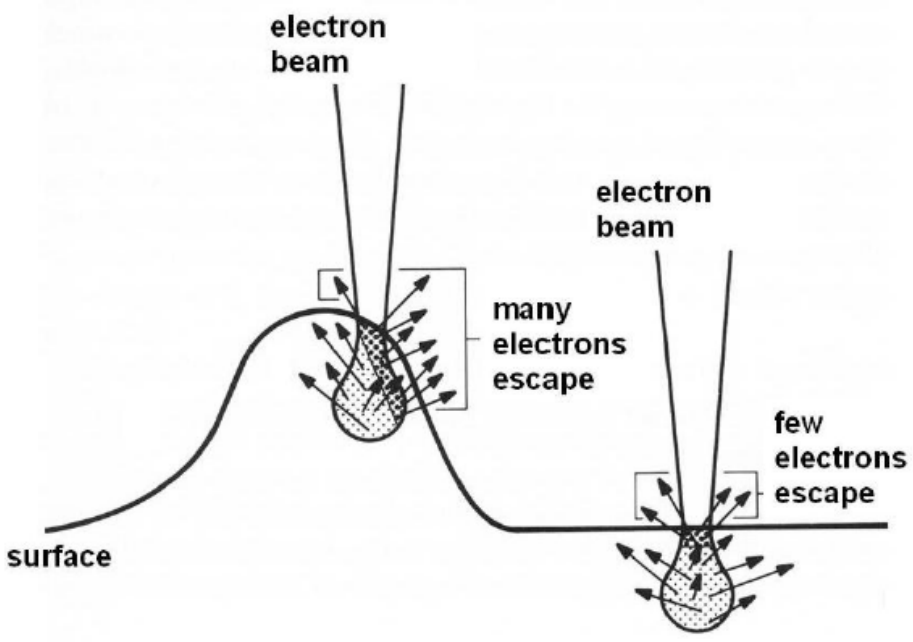

Figure 2.7: As this image shows, it is easier for secondary electrons to escape if the sample has a steep profile. Therefore edges will appear brighter in a SEM image. This is called the edge-effect. Image source: Nanotechnology lecture slides.

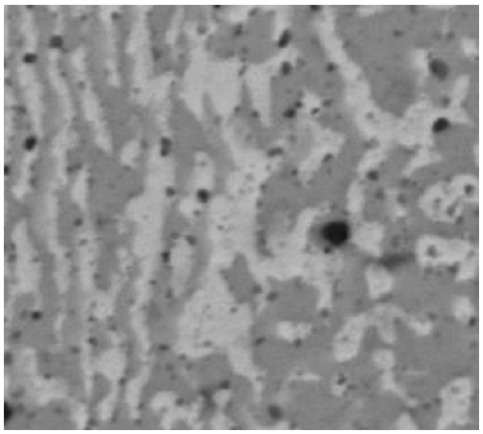

(a) Atomic number: As shown in Fig. 2.6, the amount of backscattered electrons depends on the atomic number of the imaged material. This image shows a lead/tin (Pb/Sn) alloy, imaged with a backscatter detector.

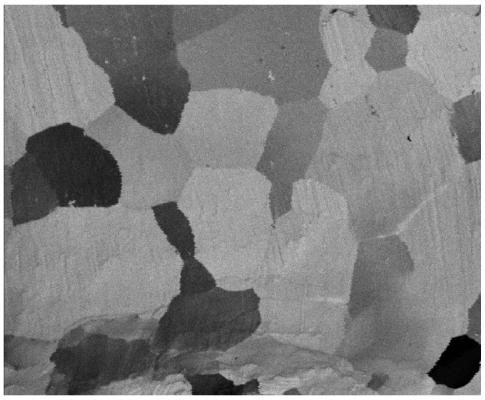

(b) Grain: The secondary electron emission depends on the crystal orientation of the material. Here grains in Tungsten (W) are shown.

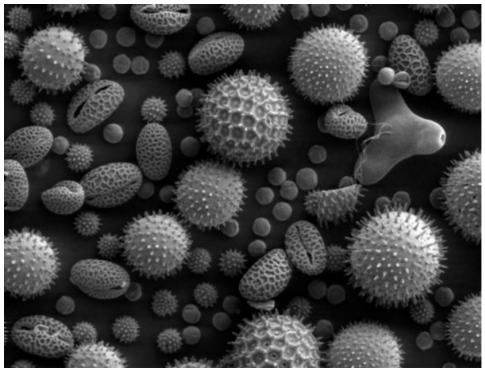

(c) Shadow: Due to the orientation of the detector, shadows can be seen: If a surface is pointing towards the detector, the measured signal will be higher.

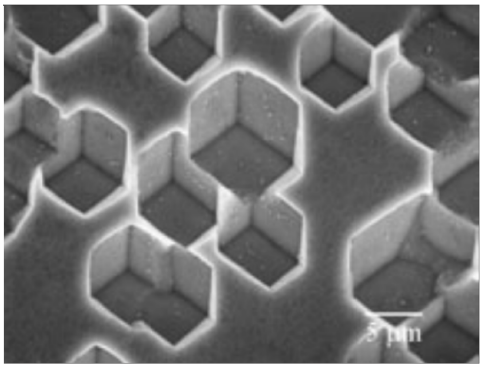

(d) Edge: As shown in Fig. 2.7, more secondary electrons can escape on the edges of these pits that are etched in steel.

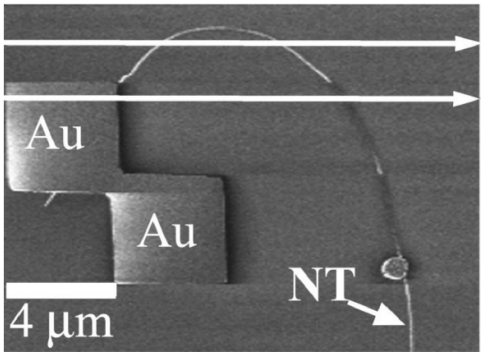

(e) Voltage: The interaction with the charged electron beam locally changes the electric potential at the surface of the sample. The trajectories of primary, secondary and backscattered electrons are influenced by this potential. Part of the secondary electrons will be prevented from reaching the detector. Thus, insulated structures will appear darker in the secondary electron image than grounded structures that do not charge [26]. The horizontal arrows in this image show the direction in which the electron beam is moving: from left to right and slowly from top to bottom.

Figure 2.8: These images give an overview of the different types of contrast in SEM images. Images source: Nanotechnology lecture slides.

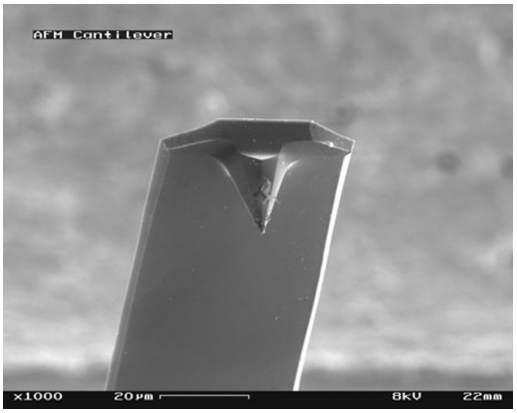

Figure 2.9: A scanning electron microscope picture of an cantilever that is used in atomic force microscopy. Image source: Lindsay [15].

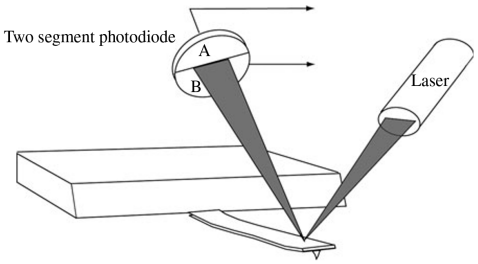

Figure 2.10: The detection scheme in atomic force microscopy: The bending of the cantilever is monitored by looking at the deflection of a laserbeam that is reflected on the backside of the cantilever. Image source: Lindsay [15].

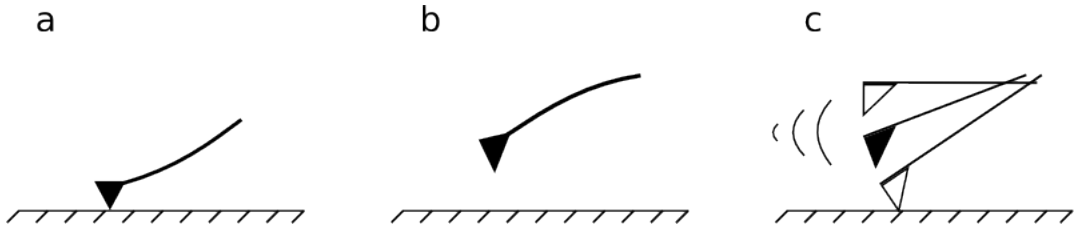

Figure 2.11: An AFM can be operated in different modes: a) Contact, b) non-contact and c) tapping mode. Image source: Wikipedia.

The cantilever has a resonant frequency that depends on its spring constant, k, and its mass, m:

$$f_0 = \frac{1}{2\pi}\sqrt{\frac{k}{m}} \tag{2.4}$$

An AFM has several distinct imaging modes [15]: (See Fig. 2.11)

- **Contact mode**: The probe is brought down to the surface until the desired contact force is measured. This contact force is kept constant as the image is created from the height correction signal. The tip is dragged over surface, which can be damaging to the surface.
- **Non-contact mode**: The probe is vibrated close to its resonance frequency, f_0. The amplitude of the oscillation is kept constant as the probe is scanned over the surface, by adjusting the probe height.
- **Tapping mode**: Uses the same principle as the non-contact mode, but now the probe hits the surface on its downward swing. This is less damaging than the dragging of the tip in contact mode.

The xy-resolution in the AFM image is dominated by the contact between probe and sample, because the shape of the probe limits the resolution that can be achieved [33]. The image is a convolution of the tip profile and surface profile. (See Fig. 2.12) Bumps will appear bigger and holes will appear smaller. Depending on the surface roughness, the horizontal resolution lies between a few and tenths of a nanometre.

2.2. Scattering of (sub-)wavelength features

As explained in subsection 2.1.1, the signal in the Rapid Nano depends on the amount of scattering. In this section some theory on scattering is provided: Rayleigh and Mie scattering, which describe

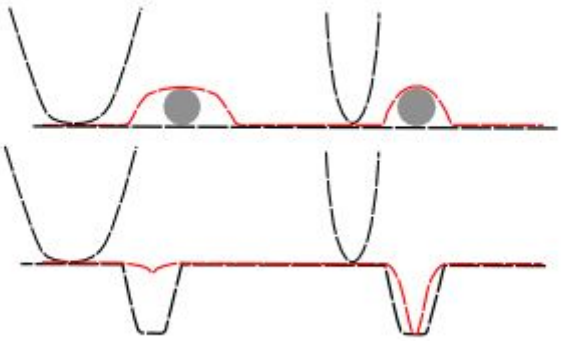

Figure 2.12: In AFM images the resolution is limited by the convolution of the tip- and the surface profile. Due to this convolution, bumps will appear bigger while pits will appear smaller. Image source: AFMhelp.com.

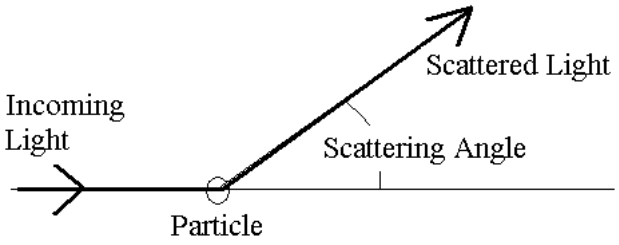

Figure 2.13: Scattering events can be described by a particle that is located at the scattering centre. This particle is hit by incoming light and some of the light will be scattered into different directions, that are defined by the scattering angle. The scattering angle is defined in spherical coordinates: (θ, ϕ). Image source: www.soest.hawaii.edu.

scattering by particles in a homogeneous medium, and the Bobbert-Vlieger model, which describes scattering from particles on a substrate, are covered. However, for reasons that are explained below, none of these existing models correctly describe the scattering behaviour of fiducial markers on a substrate. Therefore finite element analysis is necessary to get a full understanding of the scattering from these markers. Details on the developed finite element model are provided in the next section 2.3.

2.2.1. Scattering cross section

To describe scattering events quantitatively, the differential and total scattering cross functions are used. Consider incoming light with an intensity I_0 and a wavelength λ_0 in vacuum, that hits a particle. (See Fig. 2.13) The position of the particle is called the scattering centre and is placed at the origin for convenience. Some of the incoming light will be scattered by the particle.

The **differential scattering cross section** is defined as the power (W) scattered into the direction (θ, ϕ) per unit solid angle Ω (sr), divided by the incident power (W). It is denoted by:

$$\frac{d\sigma}{d\Omega}$$

The differential cross section is a function, that depends on the the scattering direction (θ, ϕ). It is given in units sr^{-1} and it is proportional to the probability of scattering in the direction (θ, ϕ).

The **intensity of the scattered light** under scattering angle (θ, ϕ) at a distance r from the scattering centre is given by:

$$I = I_0 \frac{1}{r^2} \frac{d\sigma}{d\Omega} \tag{2.5}$$

From the differential cross section the **total scattering cross section** can also be obtained by

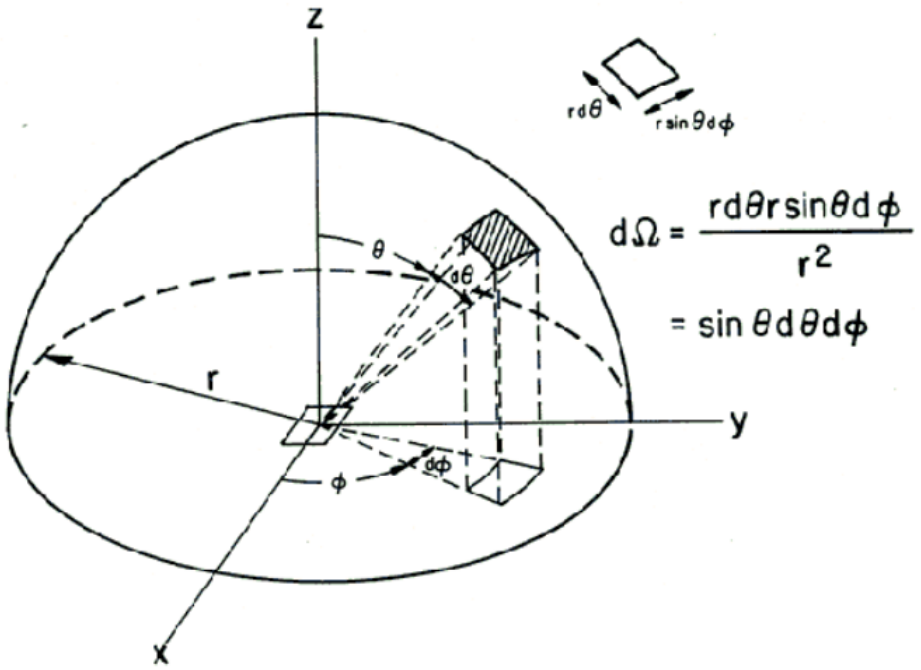

Figure 2.14: The differential cross section is used to describe scattering event quantitatively. To obtain the total scattering cross section, the differential cross section should be integrated over all solid angles (Ω). This image shows how the solid angle is expressed in spherical coordinates. $d\Omega$ represents the surface area element on the unit sphere, so formally $d\Omega = \sin\theta d\theta d\phi$. Image source: www.thermopedia.com.

integrating over all solid angles: (See Fig. 2.14)

$$\sigma = \int \frac{d\sigma}{d\Omega} d\Omega = \int_0^{2\pi} d\phi \int_0^{\pi} d\theta \sin\theta \frac{d\sigma}{d\Omega} \tag{2.6}$$

σ is unit-less and proportional to the probability of scattering in any direction.

2.2.2. Rayleigh scattering

Now consider a dielectric sphere with a radius a and a real (non-absorbing) refractive index n_{sph} as the scattering particle. If the size of the sphere is much smaller than the wavelength of the incoming light ($2\pi n_{\text{sph}} a/\lambda_0 \ll 1$), the scattering can be described by **Rayleigh scattering** [34]. The differential scattering cross section is then given by:

$$\left.\frac{d\sigma}{d\Omega}\right|_{\text{Ray}} = \frac{1}{2}\left(\frac{n_{\text{sph}}^2 - 1}{n_{\text{sph}}^2 + 2}\right)^2 \left(\frac{2\pi}{\lambda_0}\right)^4 a^6 (1 + \cos^2\theta) \tag{2.7}$$

For a derivation of this formula see Cox et al. [7]. If the sphere is not surrounded by vacuum, but by a medium, the refractive index of the sphere is replaced by $m = n_{\text{sph}}/n_{\text{med}}$ and the wavelength in vacuum by the wavelength in the medium λ_0/n_{med}.

From formula 2.7 the total scattering cross section can be determined:

$$\sigma_{\text{Ray}} = \frac{8\pi}{3}\left(\frac{2\pi n_{\text{med}}}{\lambda_0}\right)^4 a^6 \left(\frac{m^2 - 1}{m^2 + 2}\right)^2 \tag{2.8}$$

2.2.3. Mie scattering

In contrary to Rayleigh scattering, **Mie scattering** is valid for spheres of any size [7]. The Mie total scattering cross section is expressed as the infinite series:

$$\sigma_{\text{Mie}} = \left(\frac{2\pi}{k_{\text{med}}^2}\right) \sum_{n=1}^{\infty} (2n+1)(|a_n|^2 + |b_n|^2) \tag{2.9}$$

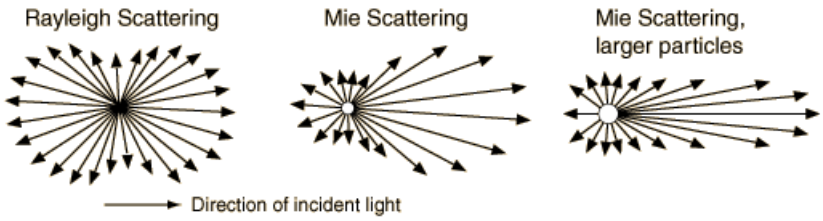

Figure 2.15: The Rayleigh theory describes the scattering by spherical particles smaller than the wavelength of the incoming light. Mie scattering is valid for spherical particles of all sizes. This image shows the scattering pattern for both types of scattering. Image source: Hyperphysics.

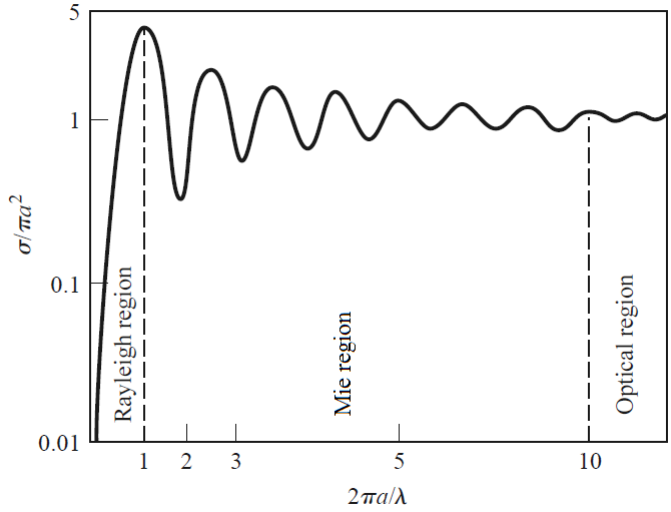

Figure 2.16: Here the Mie scattering cross section is plotted versus the particle diameter. For very small particles the Mie solution is equivalent to the Rayleigh solution. Image source: Pozar [21].

Here $k_{\text{med}} = 2\pi n_{\text{sph}}/\lambda_0$ and the coefficients a_n and b_n are given by:

$$a_n = \frac{\mu m^2 j_n(mx)[x j_n(x)]' - \mu_1 j_n(x)[mx j_n(mx)]'}{\mu m^2 j_n(mx)[x h_n^{(1)}(x)]' - \mu_1 h_n^{(1)}(x)[mx j_n(mx)]'},$$

$$b_n = \frac{\mu_1 j_n(mx)[x j_n(x)]' - \mu j_n(x)[mx j_n(mx)]'}{\mu_1 j_n(mx)[x h_n^{(1)}(x)]' - \mu h_n^{(1)}(x)[mx j_n(mx)]'}.$$

j_n is a spherical Bessel function of the first kind, h_n is a spherical Hankel function, μ and μ_1 are the magnetic permeability of respectively the medium and the sphere.

The solutions for Mie scattering are considerably more complex than those for Rayleigh scattering. Fortunately the infinite series can be evaluated by computer programs.

Fig. 2.15 shows the scattering patterns for both types of scattering. In the small particle limit, the Mie scattering is equivalent to the Rayleigh solution, as shown in Fig. 2.16.

2.2.4. Bobbert-Vlieger model

Rayleigh and Mie scattering are only valid for spheres in a homogeneous medium. The particles that are detected in the Rapid Nano however, are lying on a substrate. Bobbert and Vlieger have developed a model which takes this substrate into account [1, 2, 11, 32].

The Bobbert-Vlieger model calculates an exact solution to the scattering of light by a sphere above a surface. It combines the Mie scattering solution for a sphere in free space, that is discussed in the previous section, with the reflection of dipole radiation by a flat surface. The total scattered field consists of both the original Mie scattered field and the scattered field that is reflected back from the surface.

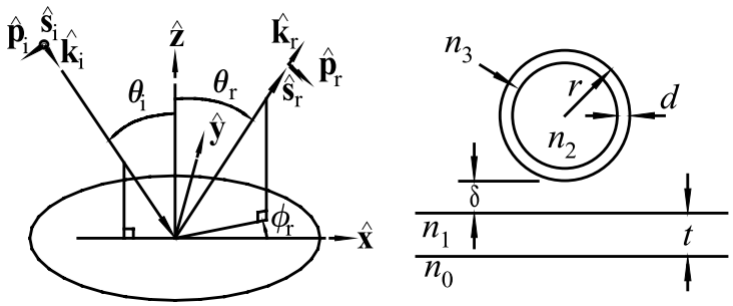

Figure 2.17: The Bobbert-Vlieger model is used to calculate the scattering of light by a sphere above a surface. This image shows the coordinate system and the different parameters that are used in tis model. Image source: Kim et al. [11].

Fig. 2.17 shows the coordinate system and the parameters that are used in the model. Both the sphere and the surface can have (multiple) coatings. The particle can either touch or float on top of the substrate, but the distance between the substrate and the particle, δ, cannot be negative. $n_0 \ldots n_3$ are the indices of refraction of the substrate, the substrate coating, the particle and the particle coating.

The Bobbert-Vlieger model has been included in the SCATMECH library of the National Institute of Standards and Technology (NIST) [18].

2.3. Finite element analysis of scatterers on substrate

For particles much larger than a wavelength, shape is an important factor in the resulting scatter pattern. As discussed in subsection 2.2.4, the Bobbert-Vlieger model assumes a spherical scatterer, while a fiducial marker corresponds to a non-spherical scatterer on a substrate, that posses both sub- and supra-wavelength features. It can be concluded that the Bobbert-Vlieger model will not provide a correct solution for this situation. Because a good understanding of their scattering behaviour is necessary to design properly functioning fiducial markers, finite element analysis (FEA) must be performed. Software for this FEA model is commercially available, in this work COMSOL Multiphysics was used.

In the subsection 2.3.1 the set-up of the FEA model and the underlying physics principles will be explained. In subsection 2.3.2 the validation of the model is discussed.

2.3.1. Setup of COMSOL model

The *Wave Optics module* in *COMSOL Multiphysics* is used for the FEA models in this thesis. This module covers electromagnetic fields and waves in two-dimensional and three-dimensional spaces. All modeling formulations are based on Maxwell's equations together with material laws for propagation in various media [6].

The **Maxwell's equations** state the relationships between the fundamental electromagnetic quantities. These quantities are [9]

- Electric field intensity $\mathbf{E}$
- Electric displacement $\mathbf{D}$
- Magnetic field intensity $\mathbf{H}$
- Magnetic flux density $\mathbf{B}$
- Current density $\mathbf{J}$
- Electric charge density ρ

Equation 2.10 gives the Maxwell's equations in their differential form. This form leads to the differ-

ential equations that can be solved with the finite element method.

$$\begin{aligned} \nabla \times \mathbf{H} &= \mathbf{J} + \frac{\partial \mathbf{D}}{\partial t} \\ \nabla \times \mathbf{E} &= -\frac{\partial \mathbf{B}}{\partial t} \\ \nabla \cdot \mathbf{D} &= \rho \\ \nabla \cdot \mathbf{B} &= 0 \end{aligned} \tag{2.10}$$

The first two of these equations are also called the **Maxwell-Ampère's law** and **Faraday's law**, respectively.

The **constitutive relations** describe the macroscopic properties of a medium:

$$\begin{aligned} \mathbf{D} &= \varepsilon_0 \mathbf{E} + \mathbf{P} \\ \mathbf{B} &= \mu_0 (\mathbf{H} + \mathbf{M}) \\ \mathbf{J} &= \sigma \mathbf{E} \end{aligned} \tag{2.11}$$

Here ε_0 is the permittivity of vacuum, μ_0 the permeability of vacuum, and σ the electrical conductivity. $\mathbf{P}$ and $\mathbf{M}$ are the electric polarisation and magnetisation vectors. For linear materials, these vectors are directly proportional to the electric and magnetic field: $\mathbf{P} = \varepsilon_0 \chi_e \mathbf{E}$ and $\mathbf{M} = \chi_m \mathbf{H}$. χ_e and χ_m are the electric and magnetic susceptibility. For these linear materials, the constitutive relations can be re-written to:

$$\begin{aligned} \mathbf{D} &= \varepsilon_0 (1 + \chi_e) \mathbf{E} &&= \varepsilon_0 \varepsilon_r \mathbf{E} = \varepsilon \mathbf{E} \\ \mathbf{B} &= \mu_0 (1 + \chi_m) \mathbf{H} &&= \mu_0 \mu_r \mathbf{H} = \mu \mathbf{H} \end{aligned} \tag{2.12}$$

ε and μ are the permittivity and permeability of the material, while ε_r and μ_r are the relative permittivity and relative permeability of the material.

In COMSOL, the *Electromagnetic Waves, Frequency Domain interface* is used to solve a **frequency-domain wave equation for the electric field**. This equation can be derived from the Maxwell-Ampère's law and Faraday's law (Eq. 2.10) [9]. Combining these equations with the constitutive relations for current and linear materials (Eq. 2.11 and 2.12), they become:

$$\begin{aligned} \nabla \times \mathbf{H} &= \sigma \mathbf{E} + \varepsilon \frac{\partial \mathbf{E}}{\partial t} \\ \nabla \times \mathbf{E} &= -\mu \frac{\partial \mathbf{H}}{\partial t} \end{aligned} \tag{2.13}$$

The electric and magnetic fields can be written in a time-harmonic form, assuming a sinusoidal excitation with angular frequency ω and again linear media:

$$\begin{aligned} \mathbf{E}(x, y, z, t) &= \mathbf{E}(x, y, z) e^{j\omega t} \\ \mathbf{H}(x, y, z, t) &= \mathbf{H}(x, y, z) e^{j\omega t} \end{aligned} \tag{2.14}$$

In this notation j is the imaginary number: $j = \sqrt{-1}$. Combining equations 2.13 and 2.14 results in a time harmonic equation for the electric field, or a similar equation for the magnetic field:

$$\begin{aligned} \nabla \times (\mu^{-1} \nabla \times \mathbf{E}) - \omega^2 \varepsilon_c \mathbf{E} &= \mathbf{0} \\ \nabla \times (\varepsilon_c^{-1} \nabla \times \mathbf{H}) - \omega^2 \mu \mathbf{H} &= \mathbf{0} \end{aligned} \tag{2.15}$$

The first of these equations is the wave equation that is used in the COMSOL interface. Here ε_c is the complex permittivity: $\varepsilon_c = \varepsilon - j\sigma/\omega$.

When dealing with optics and photonics applications, the **refractive index** is often used instead of the relative permittivity. They are related in the following way:

$$n = \sqrt{\varepsilon_r \mu_r} \tag{2.16}$$

For most materials the relative permeability, μ_r, is very close to 1 at optical frequencies. In those cases:

$$n = \sqrt{\varepsilon_r} \tag{2.17}$$

Table 2.1: This table lists the refractive indices and extinction coefficients of all the materials that were used in the COMSOL model. Source: Polyanskiy [20].

Material	**Refractive index n at λ = 532 nm**	**Extinction coefficient κ at λ = 532 nm**
Vacuum	1	0
Silicon	4.1360	0.010205
Gold	0.54410	2.1404
Platinum	2.0382	3.661

The refractive index, n, can be written as a complex number:

$$\overline{n} = n - j\kappa \tag{2.18}$$

The imaginary part of the refractive index, κ, is also called the **extinction coefficient**. Eq. 2.17 and 2.18 can be used to express the complex relative permittivity in terms of n and κ:

$$\varepsilon_{rc} = \overline{n}^2 = \varepsilon' - j\varepsilon'' \tag{2.19}$$

where

$$\begin{aligned} \varepsilon_r' &= n^2 - \kappa^2 \\ \varepsilon_r'' &= 2n\kappa \end{aligned} \tag{2.20}$$

The real part of the relative permittivity, ε_r', is related to the stored energy within the medium, while the imaginary part, ε_r'', is related to losses within the medium.

Now the frequency domain wave equation for the electric field (Eq. 2.15) can be expressed using the refractive index:

$$\nabla \times (\nabla \times \mathbf{E}) - k_0^2 \overline{n}^2 \mathbf{E} = \mathbf{0} \tag{2.21}$$

The wave number in vacuum, k_0, is defined by:

$$k_0 = \omega\sqrt{\varepsilon_0 \mu_0} = \frac{\omega}{c_0} \tag{2.22}$$

where c_0 is the speed of light in vacuum. The complex indices of refraction of all the materials that were used in the model, are listed in Table 2.1.

To fully describe the electromagnetic problem, **boundary conditions** are specified at all the material interfaces and physical boundaries:

$$\begin{aligned} \mathbf{n}_{\mathrm{i}+1} \times (\mathbf{E}_{\mathrm{i}} - \mathbf{E}_{\mathrm{i}+1}) &= \mathbf{0} \\ \mathbf{n}_{\mathrm{i}+1} \cdot (\mathbf{D}_{\mathrm{i}} - \mathbf{D}_{\mathrm{i}+1}) &= \rho_s \\ \mathbf{n}_{\mathrm{i}+1} \times (\mathbf{H}_{\mathrm{i}} - \mathbf{H}_{\mathrm{i}+1}) &= \mathbf{J}_s \\ \mathbf{n}_{\mathrm{i}+1} \cdot (\mathbf{B}_{\mathrm{i}} - \mathbf{D}_{\mathrm{i}+1}) &= 0 \end{aligned} \tag{2.23}$$

ρ_s and $\mathbf{J}_s$ denote the charge density and the current density at the surface of the interface. $\mathbf{n}_{\mathrm{i}+1}$ is the normal vector pointing outward from medium i + 1.

In FEA models a **Perfectly Matched Layer** (PML) can be used to model a domain with open boundaries, i.e. a domain that extends to infinity [5]. A PML is a layer of virtual domain surrounding a physical domain. This layer absorbs all outgoing wave energy in frequency-domain problems, so that no spurious reflections occur: The PML acts as a perfect absorber at the domain boundary. Fig 2.18 shows different domains in the 2D COMSOL simulation that was used to model the scattering from a fiducial marker on a substrate. The PMLs are indicated by the shaded regions. The shape of the PMLs is adapted to the propagation direction of the waves that it should absorb, because perpendicular incoming waves are better absorbed than parallel waves.

The **source of incoming light** is defined as an incident field on a boundary: See Fig. 2.19. On this boundary a wide smoothed beam is excited. To mimic the conditions in the Rapid Nano, this incoming light has a total power of 1 Watt and a wavelength of 532 nm. It is TM-polarized and enters the model under an angle of 60 degrees with respect to the substrate normal. (See section 2.1.1)

The Electromagnetic Waves Frequency Domain interface has an option to solve for the **scattered field**, a perturbation to the **background field** caused by a local scatterer (the fiducial marker in this

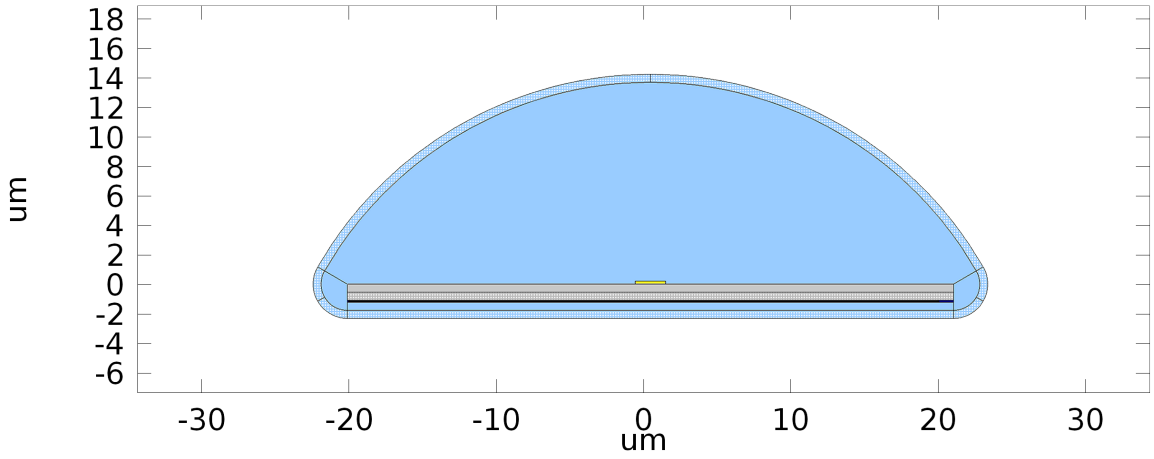

Figure 2.18: This image provides an overview of the domains in the 2D COMSOL simulation. The blue area corresponds to air/vacuum, the grey area to a silicon substrate and the yellow area to a metal fiducial marker (which is made from either gold or platinum). The shaded regions are perfectly matched layers. The model contains an external PML on the outer boundary of the computational domain and an internal PML under the silicon substrate. The internal PML absorbs the light that is transmitted into the substrate. This light is not of interest in the model and this way the computation domain can be reduced.

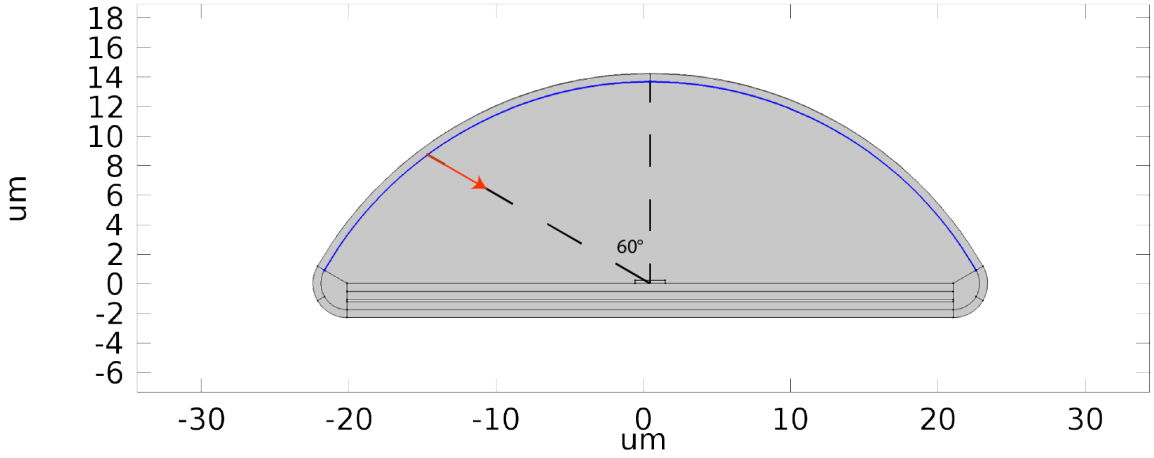

Figure 2.19: In the COMSOL simulation, the incoming light is defined on the boundary that is marker blue. It is excited as a smoothed beam with a total power of 1 W. The light has a wavelength of 532 nm, is TM-polarized and enters the simulation under an angle of 60 degrees with respect to the surface model.

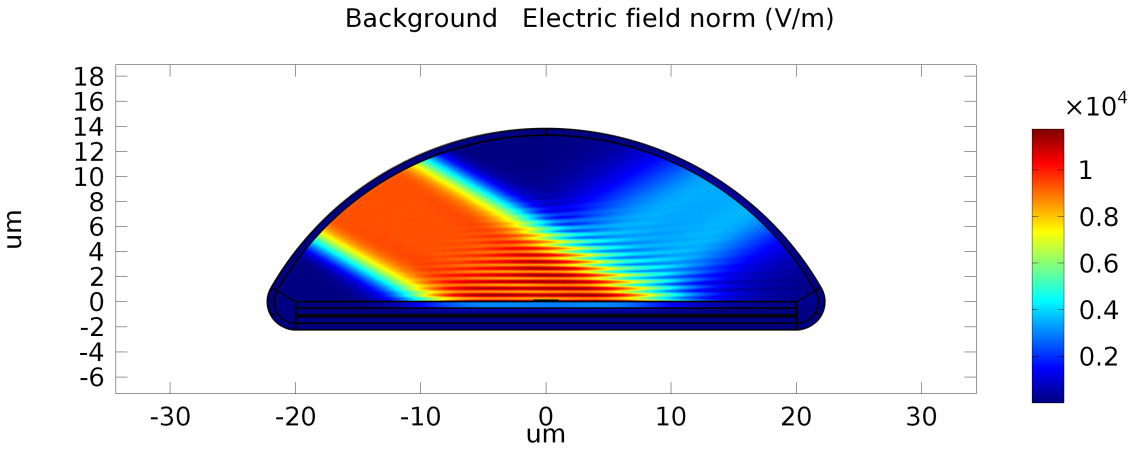

Figure 2.20: The background field in 2D COMSOL simulation is the solution to the wave equation without the presence of the fiducial marker. It consists of the incoming and specular reflected beam of light. Due to interference between these two, a standing wave pattern appears above the silicon substrate.

model) [6]. The background field is the solution to the wave equation without the presence of the fiducial marker.

To calculate this background field, the material of the fiducial marker is temporary set to air/vacuum, so the incoming wave only encounters the substrate. Fig. 2.20 shows the calculated background field: The light enters the model from the left and is reflected on the substrate. Due to the interference of the incoming and the specular reflected wave, a standing wave pattern appears above the substrate. Part of the incoming light is also transmitted into the substrate, but this light is absorbed by the internal PML.

Once the background field has been calculated, the material of the fiducial marker is changed to a metal and the solution for the background field is used to calculate the scattered field. The **total field** is the sum of the background and the scattered field.

So far, the simulations provide information about the electromagnetic field in the vicinity of the substrate, also known as the **near field**. However, the Rapid Nano images the **far field**, which is defined much further from the substrate. In COMSOL, the far electromagnetic field can be derived from the near field using the **Stratton-Chu formula** [5]. In a 3D situation this formula is:

$$\mathbf{E}_p(\mathbf{r}_0) = \frac{jk}{4\pi}\mathbf{r}_0 \times \int [\mathbf{n}\times\mathbf{E} - \eta\mathbf{r}_0 \times (\mathbf{n}\times\mathbf{H})] \exp(jk\mathbf{r}\cdot\mathbf{r}_0) dS \tag{2.24}$$

And in 2D it is:

$$\mathbf{E}_p(\mathbf{r}_0) = \sqrt{\lambda}\frac{jk}{4\pi}\mathbf{r}_0 \times \int [\mathbf{n}\times\mathbf{E} - \eta\mathbf{r}_0 \times (\mathbf{n}\times\mathbf{H})] \exp(jk\mathbf{r}\cdot\mathbf{r}_0) dS \tag{2.25}$$

For these calculations the scatterer should be located close to the origin. $\mathbf{r}_0$ is a unit vector pointing from the origin to a point in the far-field, defined by the angular position (θ, ϕ). $\mathbf{E}_p$ is the far field at this point. S is a surface in the near field that encloses the scatterer, with corresponding normal vector $\mathbf{n}$ and radius vector $\mathbf{r}$. $\mathbf{E}$ and $\mathbf{H}$ are the electric and magnetic field on this surface. η is the impedance: $\eta = \sqrt{\mu/\varepsilon}$. k is the wave number and λ is the wavelength. See Fig. 2.21 for the chosen far-field domains and the boundaries where the near field is integrated in the 2D model. The Stratton-Chu formula requires that the scattering object is completely enclosed by these boundaries and the far-field domains should have homogeneous material properties.

$\mathbf{E}_p$ is also known as the **scattering amplitude**, which is related to the differential scattering cross section by:

$$|\mathbf{E}_p|^2 = \frac{d\sigma}{d\Omega} \tag{2.26}$$

2.3.2. Validation of COMSOL model

The model has been qualitatively verified by experiments that confirm the findings of the scattering properties in the Rapid Nano. The findings of the COMSOL simulations are discussed in 5.1 and the

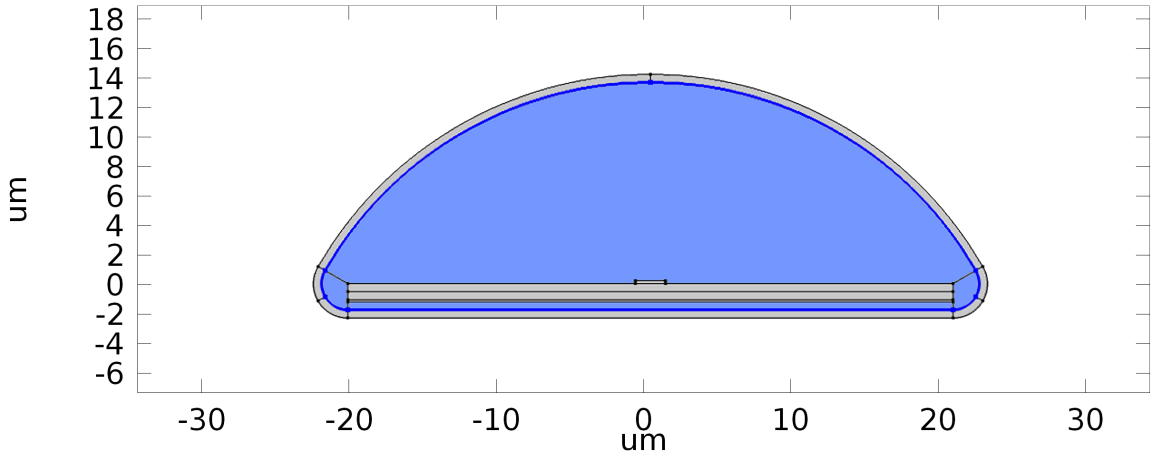

Figure 2.21: The Stratton-Chu formula is used to calculate the far field solution from the near field solution in the COMSOL model. Here the far field domain that is used in this calculation is indicated with light blue. The boundaries that form the closed surface S, are depicted in dark blue.

experiments that confirm these findings in section 5.2.

However, the 2D model does not correspond to an existing physical situation. Therefore it can not be used for a quantitative verification of the COMSOL model. For this purpose a 3D model should be made. This 3D model can also be compared with existing scattering theories, by simulating the scattering of particles that correspond to the Rayleigh, Mie and Bobbert-Vlieger theory.

The first steps in creating the 3D model have been made, but the model is not completed yet at the time of the printing of this thesis.

3

System engineering

In this chapter the verification process of the fiducial marker system is documented. Section 3.1 gives an overview of the concept of operations. The requirements for the fiducial marker (system) are listed in section 3.2) and the design is presented in section 3.3.

3.1. Concept of operations

As explained in section 1.3, the first step in the development of the fiducial marker system is to gain a proper concept of operations: Why is a fiducial marker system needed and how exactly will it be used?

To answer these questions, it will first be discussed how the Rapid Nano, a scanning electron microscope, and an atomic force microscope are used to characterise defects on blank wafers. The work flow with and without fiducial marker system will be presented in sections 3.1.1–3.1.4. All the information that is mentioned in these section, was gathered through interviews with experienced operators of the three imaging platforms. (The operators are named in the Acknowledgements of this thesis.)

As will be discussed, the fiducial marker system needs to provide accuracy in position. This begs the question: What is the effect of an error in the measured position of a marker or a defect on the different imaging systems? Monte Carlo simulations are used to understand how these errors propagate during the use of the fiducial marker system. The outcome of the simulations are used to quantify the maximal positioning accuracy that the fiducial marker system can provide. The results of the Monte Carlo simulations are presented in subsection 3.1.5.

The fiducial markers that were previously tried on blank wafers are also discussed in subsection 3.1.6. Special attention is paid to the shortcomings of these markers. This subsection concludes the section on the concept of operations.

3.1.1. Why is a fiducial marker system needed?

Fig. 3.1 shows a schematic overview of how the Rapid Nano, a scanning electron microscope, and an atomic force microscope are used to detect and classify defects. The detection and classification are used to qualify tools and processes on cleanliness. For the qualification process unpatterned substrates, known as blanks, are used as witness samples [3, 28].

The Rapid Nano scans are used to keep track of the particles that are added in the tool or process that is being qualified. This is done by making two Rapid Nano scans. First a reference Rapid Nano scan of the blank is made (the pre-scan). The blank then goes through multiple cycles in the tool, until some particles are added for analysis. Typically a single particle is added during every 100 or 1000 cycles. After these cycles, a second Rapid Nano scan is made (the post-scan). The pre- and post-scan are compared to see which particles were added by the tool or process. The output of the review with the Rapid Nano is a defect map: A list of particles that were added, their respective sizes and their location in the coordinates of the Rapid Nano stage. To further characterise the added particles, the substrate is transferred to another tool: Either a scanning electron microscope (See section 3.1.3) or an atomic force microscope (See section 3.1.4).

Once the blank is transferred to a SEM or AFM, for a further investigation of the particles that were found in the Rapid Nano, the operators need to re-detect the particles on the defect list. This forms a

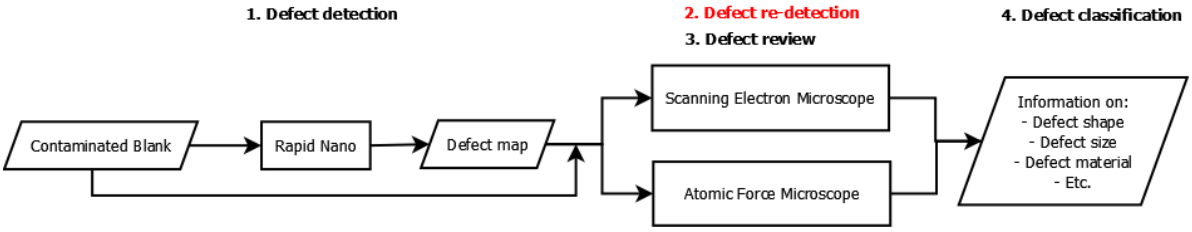

Figure 3.1: This diagram shows how the Rapid nano, a scanning electron microscope, and an atomic force microscope are used to classify defects. First the Rapid Nano detects the defects on a contaminated. The output of this process is a defect map. (1) Then the contaminated blank is transferred to a SEM or AFM, where the defects on the defect map are re-detected (2) and reviewed. (3) The review provides further information on the defect, which is used to classify it. (4) A problem occurs at the re-detection of defects, step 2, because the defects are so small they they are very difficult to re-detect in the SEM or AFM. A fiducial marker system will increase the re-detection rate of defects.

challenge because these particles are very small [12]. Take for example a particle with a diameter of 50 nm. To be visible in a SEM image, these 50 nm should correspond to at least 10 pixels. So the entire field of view, of approximately 1000 pixels, should be 5000 nm (5 µm) at the most. This almost corresponds to the smallest field of view possible in SEM. In other words: In order to be able to see a particle, the SEM should be operated while maximally zoomed in.

Because the tools and processes that are being qualified do not produce much contamination, the density of particles on the blanks is low. For very clean processes, there could be less than 10 added defects on the blank. In a small field of view, only a small area (e.g. 5×5 µm) of the sample is viewed per image. If the position of the particle is not accurately known, many of these images need to be made before a particle is found. This makes the re-detection of a particle very time consuming. Interviewed operators indicate that often times the search process takes too long. If this happens, they abort the search for a certain defect and move on to the next defect on the defect list. This means that many particles on the defect list are not re-detected at all. This can cause a biased or incomplete defect classification. Narrowing the search area is necessary to increase the re-detection rate.

This is were the fiducial marker system comes in: The fiducial markers are much bigger than the defects, so operators can easily find the markers in a big field of view. Once the markers are found, they will aid the operators in finding the defects: If the position of a marker system ánd the position of a particle relative to the marker system are known, the absolute location of the particle can also be calculated.

For this purpose, the fiducial markers should be applied on the blank before it is scanned with the Rapid Nano. The resulting defect map then does not only contain the size and position of the added defects, but also the position of the markers in the coordinate system of the Rapid Nano. After the Rapid Nano scan, the sample is transferred to the SEM or AFM. The operators need to find the location of at least 3 markers in the SEM/AFM, to have enough data points to determine a transformation function. (This process will be fully explained in section 3.1.5.) The transformation function maps the coordinate system of the Rapid Nano to the coordinate system of the SEM/AFM. Once this function is found, it can be used to calculate the position of a particle on the defect map in SEM/AFM coordinates. Then, the operators can go directly to these coordinates and if they are accurate enough, they will find the particle at the pinpointed position without having to search [22].

In Chapter 2 the working principles of the Rapid Nano, the scanning electron microscope, and the atomic force microscope have been explained. In the following subsections (3.1.2–3.1.4) the work flow with the fiducial markers system will be explained for these tools. Relevant specifications of the used machines are provided and some practicalities to keep in mind are also described. This information was gathered by interviewing experts on the different machines.

3.1.2. Using the fiducial marker system on the Rapid Nano

The fiducial markers should be applied to the blank before the pre-scan on the Rapid Nano is made. Then the e output of the Rapid Nano scans are the positions of the markers and the particles in Rapid Nano coordinates. Every position has an error in the x- and y-direction. The Rapid Nano images of the markers and the size of the detected are also provided as output.

Because the Rapid Nano has a left-handed coordinate system, the coordinates of the markers and the particles that are selected for review are transformed to right-handed coordinates.

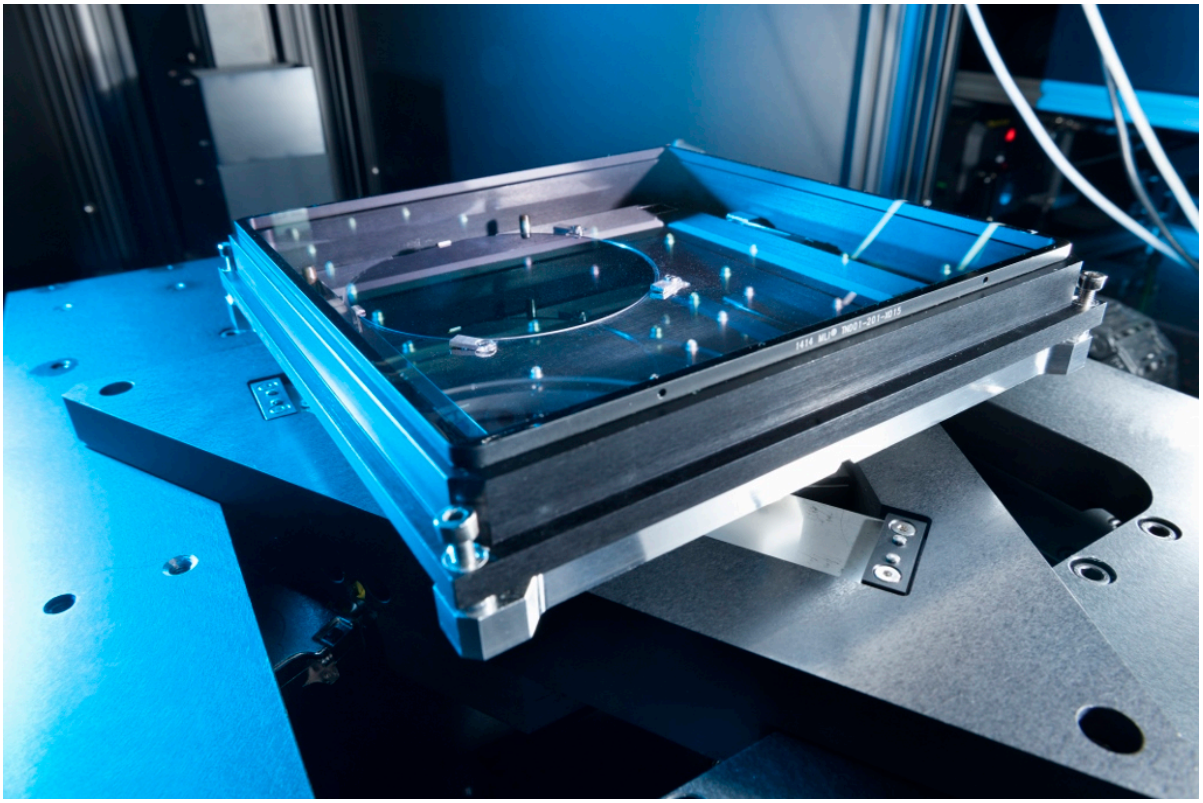

Figure 3.2: During the Rapid Nano scans, the blank wafer is placed in a scanbox. The scanbox protects the blank from contamination. Here it is depicted with a 4 inch blank wafer inside the Rapid Nano.

The operators of the Rapid nano should be familiar with the design of the fiducial marker system. They can use this information and the Rapid Nano images of the marker to determine if the markers have been identified correctly. If this is the case, the operators can proceed with the defect review on the scanning electron microscope.

The field of view (FOV) in the Rapid Nano is 1600×1200 pixels, corresponding to approximately 1500 μm^2. It is not possible to zoom in. A single pixel corresponds to 800 nm^2. If scatting features are located too close to each other, they will not be distinguishable. The stage of the Rapid Nano has a repeatability of 1 µm.

Because the Rapid Nano detects scattered light, the used substrates cannot be transparent and they should be very smooth. Usually polished silicon wafers are used. During the inspection with the Rapid Nano, the blank is placed inside a scanbox, which will protect the blank from contamination during the scan. (See Fig. 3.2) The maximal substrate size that can fit into the scanbox is 152 × 152 mm.

3.1.3. Using the fiducial marker system on a scanning electron microscope

The flowchart in Fig. 3.3 shows an overview of the sequential processes and information flows during the defect classification with the Rapid Nano and a scanning electron microsope. The work flow and results from the Rapid Nano have been discussed in the previous section.

The first step in the scanning electron microscope is to find the position of (at least) three fiducial markers. All scanning electron microscopes have the possibility to zoom in and out: Normally the field of view can vary from 1–3 mm to 1 µm. Operators use this zoom function while searching for the markers: Initially they start at the largest FOV and once they find a marker, they zoom in to accurately determine the position of the marker in SEM coordinates. This position also has an error in the x- and y-direction. The dwell time per pixel can also be altered: During the search for a marker, a shorter dwell time is used to quickly scan the surface of the sample. Once the marker is found, the dwell time is increased to produce an image with less noise. It normally takes about one minute to build one high-quality image.

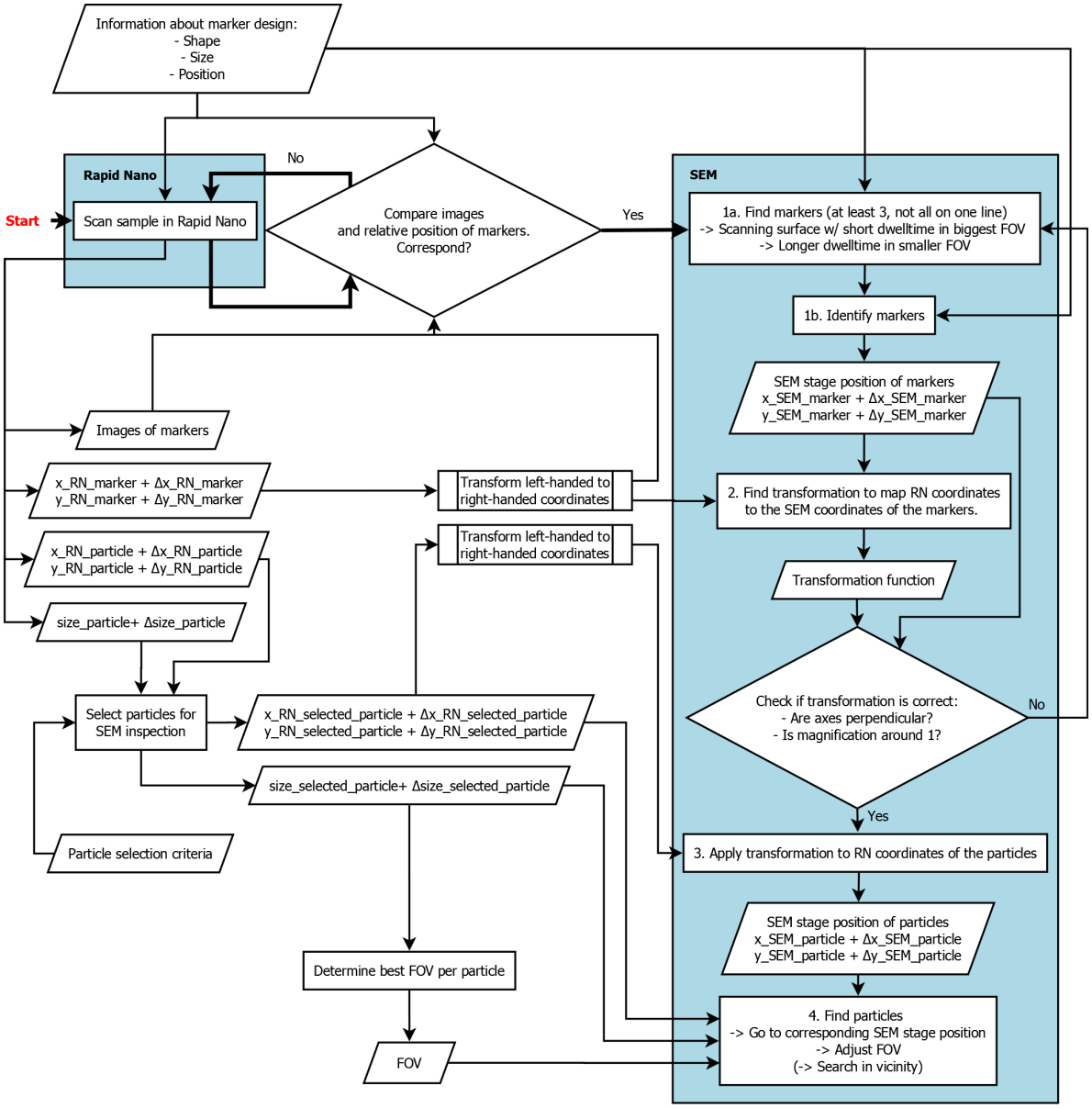

Figure 3.3: This flowchart shows the sequential steps and flows of information during the defect classification with the Rapid Nano and a scanning electron microscope. The scan and output of the Rapid Nano are explained in 3.1.2, the processes in the scanning electron microscope are explained in 3.1.3. The error in the (measured and transformed) x- and y-positions are denoted with the Δ's in this flowchart.

The determined SEM marker coordinates and the Rapid Nano coordinates of the corresponding markers are used to determine the transformation function. (See section 3.1.5.) Some easy checks are performed to determine if the transformation function is correct. Most SEM software supports the use of “user units”. In these cases the coordinate transformation is done automatically, if the Rapid Nano coordinates of the identified markers are provided.

The transformation function is used to transform the Rapid Nano coordinates of the defects, that are selected for review, to SEM coordinates. The transformed coordinates will also have an error. The size of this error is studied with Monte Carlo simulations in section 3.1.5.

Once the defect coordinates are transformed, the operators can directly send the SEM stage to the calculated positions. The field of view of the scanning electron microscope should be adjusted to the size of the corresponding defect: The defect should comprise at least 10 pixels to be visible in the SEM image. The dimension of SEM images is typically 1024×884 pixels. So if a particle has a diameter of 50 nm, the horizontal field width should be 5 micron. If the error in the transformed coordinates is small enough, the particle will be visible immediately. Otherwise the operators should search for the particle in the vicinity of the predicted position.

There are many different scanning electron microscopes commercially available. The specifications on resolution and stage accuracy are slightly different for every model. The scanning electron microscope that was used in this thesis is the FEI Nova NanoSEM 450. This model can reach a resolution of 1 nm and has a stage with a repeatability of 2 µm.

In section 2.1.2 the different types of contrast in SEM were explained. These contrast types should be kept in mind when designing a marker that should be visible in a SEM. For example, markers are preferred to have a profile with high straight edges because of the edge contrast.

The markers should be made from a conducting material: Otherwise the marker can become charged during the inspection in the SEM. This will increase the uncertainty in the marker position, because the charged material will deform the electron beam.

Possible carbon contamination should also be considered: In a bad vacuum hydrocarbons can deposit on the sample. They will form a thin layer of graphite. This can form a problem if, for example, the blank is first studied in a SEM and sub-sequentially in an AFM.

3.1.4. Using the fiducial marker system on an atomic force microscope

Currently atomic force microscopy is not yet used to characterise defects after a Rapid Nano scan, because it is a slow inspection method: Typically a few lines per second are scanned. Building an entire image takes a few minutes. Re-detection with the relative fast SEM already forms a challenge, so re-detecting defects on an AFM within a reasonable amount of time is an impossible task without proper fiducial markers.

However, using an AFM for defect classification is desirable: In a SEM it can be difficult to determine e.g. the atomic composition of a defect, the EDX signal from the substrate overwhelms the the signal from the defects. The AFM on the other hand can be used to determine mechanical properties from individual particles [8]. It also provides information on the height of structures on a sample. Therefore it can be favourable to also use an AFM for the defect classification [12, 25]. To enable this, the fiducial marker system should also work on an AFM.

The process for the re-detection of the defects on an AFM is very similar to the process on a SEM. For a schematic overview of the process see Fig. 3.5. The process in the Rapid Nano goes exactly the same, but the search for the fiducial marker is different in an atomic force microscope than on a scanning electron microscope:

To find a marker on a sample in an AFM, an optical microscope in bright field reflection mode is used. If a marker is found, the tip of the AFM is dropped in the vicinity of the marker. This happens, depending on the used AFM, with a positioning accuracy of approximately 10 µm. The used tip influences this positioning accuracy: Some tips are positioned at the very end of the cantilever, but with others it is set back slightly. (See Fig. 3.4) The exact tip position can vary with a few µm, even with cantilevers from the same batch. Because the optical microscope images the sample and the tip from above, it is not possible to see the tip as it approaches the surface. Therefore cantilevers that have their tip located at the end can be positioned more precisely.

After the tip is dropped in the vicinity of a marker, it will scan the marker to accurately determine the position of the marker. The marker positions are used to find the transformation function in the same way as on a SEM. The transformation function is used to calculate the positions of the selected defects

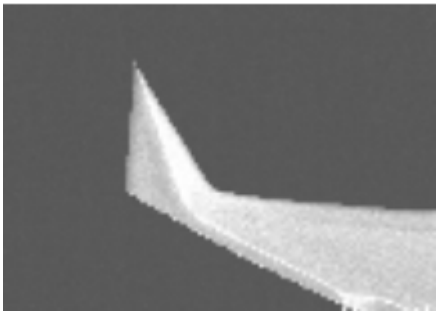

(a) Tip located just at the end of the AFM cantilever. Image source: probe.olympus-global.com

(b) Tip set back with approximately 15 µm. Image source: www.budgetsensors.com

Figure 3.4: The location of the tip on an AFM cantilever influences the positioning accuracy of the tip on the sample. Tips that are placed just at the end of the cantilever are the most accurate.

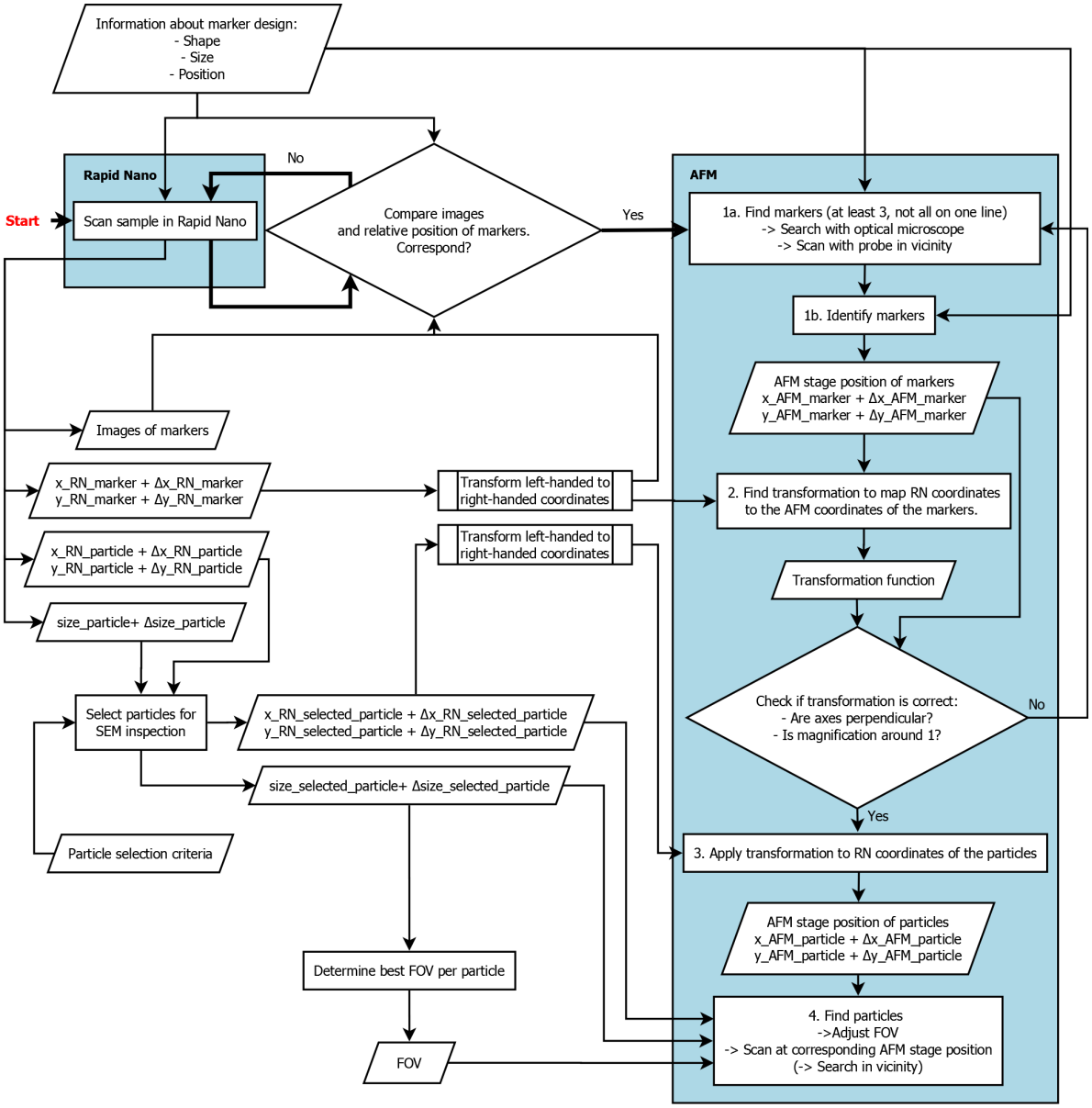

Figure 3.5: This flowchart shows the sequential steps and flows of information during the defect classification with the Rapid Nano and an atomic force microscope. (See previous flowchart in Fig. 3.3) The process is almost identical to the process with the scanning electron microscope, but the way the markers and particles are detected is different.

in AFM coordinates. Once these coordinates are known, the tip can be dropped immediately at the calculated position to scan the defect. The scanning range should be altered, depending on the size of the defect, so that the defect will be visible in the AFM image. If the error in the transformed defect coordinates is small enough, the particle will be scanned in the first image. Otherwise the vicinity of the predicted location should also be scanned, until the particle is found.

In this work, the Bruker Dimension FastScan AFM is used. It has a stage repeatability of 3 micron. The resolution of an AFM image depends on the scanned surface. On a very smooth surface the resolution can be atomic or even smaller. If the surface is rougher, the resolution will be between 1 and 10 nm.

Because an optical microscope is used for the navigation on the samples, fiducial markers should mainly be optimised for this system. The AFM does impose a height restriction: A low marker takes less time to scan and it will prevent damage to the AFM tip, caused by the tip crashing into the steep walls of a high marker.

As described in chapter 2, the AFM tip may damage the sample depending on the used mode. Biological and soft materials are damaged easily and are therefore less suited as marker materials. A hard material is also incompressible and this prevents deviations in the height measurements.

Finally, some things to keep in mind regarding the size and position of the fiducial markers: The maximum scanning range of a single image typically lies between 10–100 µm and images consist of a few hundred by a few hundred pixels. So for a big scanning range, a single pixel consists of tens of nanometres. Depending on the design of the AFM, it may not be possible for the cantilever to reach every area on a sample. This applies particularly for large samples, such as 4 inch wafers.

3.1.5. Propagation of error in position of markers and defects

As discussed in section 3.1, the transformation matrix T relates the coordinates of a single point in two different coordinate systems to each other. For example, if the coordinates of a particle in the Rapid Nano are known, the coordinates of the same particle in the SEM can be calculated by:

$$\vec{x}_{SEM} = T\vec{x}_{RN} \tag{3.1}$$

For a two dimensional system, where every position on the sample has a x- and y-coordinate, eq. 3.1 is written as:

$$\begin{bmatrix} x' \\ y' \\ 1 \end{bmatrix} = \begin{bmatrix} a & b & c \\ d & e & f \\ 0 & 0 & 1 \end{bmatrix} \begin{bmatrix} x \\ y \\ 1 \end{bmatrix} \tag{3.2}$$

Note that the coordinates on the SEM are indicated with a prime and the coordinates on the Rapid Nano without a prime. First, the transformation matrix needs to be found. The matrix contains 6 unknowns, so there are 6 equations needed to determine the matrix elements a–f. Eq. 3.2 can be re-written into the equations:

$$\begin{aligned} x' &= ax + by + c \\ y' &= dx + ey + f \\ 1 &= 1 \end{aligned} \tag{3.3}$$

So if the x- and y- position of three different markers are known on both platforms, the matrix can be solved.

$$\begin{aligned} x'_1 &= ax_1 + by_1 + c \\ y'_1 &= dx_1 + ey_1 + f \\ x'_2 &= ax_2 + by_2 + c \\ y'_2 &= dx_2 + ey_2 + f \\ x'_3 &= ax_3 + by_3 + c \\ y'_3 &= dx_3 + ey_3 + f \end{aligned} \tag{3.4}$$

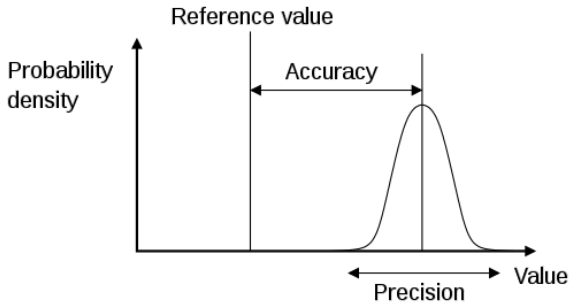

Figure 3.6: Accuracy and precision are not the same thing. Accuracy refers to a bias or systematic error, while precision refers to an error, standard deviation or variability of a measurement. Manufacturers of imaging platforms do not specify the accuracy, but only the precision of their tools. In the Monte Carlo simulation it is assumed that the deviations in the measured positions are indeed only caused by the precision of the tools. Image source: Wikipedia.

These 6 equations can also be written in matrix form:

$$\begin{bmatrix} x_1' \\ y_1' \\ x_2' \\ y_2' \\ x_3' \\ y_3' \end{bmatrix} = \begin{bmatrix} x_1 & y_1 & 1 & 0 & 0 & 0 \\ 0 & 0 & 0 & x_1 & y_1 & 1 \\ x_2 & y_2 & 1 & 0 & 0 & 0 \\ 0 & 0 & 0 & x_2 & y_2 & 1 \\ x_3 & y_3 & 1 & 0 & 0 & 0 \\ 0 & 0 & 0 & x_3 & y_3 & 1 \end{bmatrix} \begin{bmatrix} a \\ b \\ c \\ d \\ e \\ f \end{bmatrix} \tag{3.5}$$

Which is defined as:

$$\vec{u} = M\vec{v} \tag{3.6}$$

Then it is easy to find $a \ldots f$, by solving for vector $\vec{v}$:

$$\vec{v} = M^{-1}\vec{u} \tag{3.7}$$

The fact that the positions of at least *three* markers are needed to find the transformation function, can also be explained in the following way: At least three points that do not lie on a single line are needed to define two vectors, that can span a 2D vector space. So if three markers are chosen as the point references, the transformation function for the entire 2D coordinate plane can be determined. Note that the three markers should also not lie on a single line.

The accuracy of the transformed coordinates of a defect depends on the error in the marker position (both on the Rapid Nano and SEM), the error in the defect position (on the Rapid Nano), and the positions of the markers that are used to find the transformation function. To understand exactly how these errors propagate if the marker system is used, a Monte Carlo simulation is performed. The full MATLAB script that is used for this simulation is included in Appendix A.

In this simulation it is assumed that the stages of the imaging platforms are accurate: i.e. they do not have a bias or a systematic error. (See Fig. 3.6) The error in the stage position is completely attributed to the repeatability of the used stage, as specified by the manufacturers of the used imaging platforms. The specified repeatability of the Rapid Nano is 1 micron, 2 micron for the FEI Nova NanoSEM 450 and 3 micron for the Bruker Dimension FastScan AFM.

In the simulation, the marker positions of a real sample are used: 12 markers that are distributed across a blank wafer, with a mutual spacing of 20 mm and 90° angles. The measured coordinates on both systems (the Rapid Nano and the scanning electron microscope) are noted. For each iteration in the simulation, a different deviation is added to position of the markers. The size of the error has a normal distribution, with zero mean and a standard deviation that corresponds to the positioning precision of the used machine. In each iteration a new transformation matrix is calculated, using the positions of three markers including error. Once the T matrices are calculated, they are used to map the positions of all Rapid Nano coordinates (also with an added error in their position) to SEM coordinates. In every iteration these calculated SEM coordinates have a small deviation, due to the error in the Rapid Nano position and the error in the transformation matrix. Over all the iterations, the standard deviation in the predicted SEM coordinates is calculated for every position.

If the operators send the SEM stage to a certain position, the stage will not land exactly on the predicted coordinates. Therefore the positioning precision of the SEM stage should again be taken into account: To get the total error in the final SEM position, the error in the predicted position and the error of the SEM stage are averaged.

The results of the Monte Carlo simulation are shown in the 2D plot in Fig. 3.7. Note that not the error, but the 3σ number in the predicted position is plotted. 99.7% of the particles will be located within a radius of the 3σ number from their pinpointed position. The diagonal distribution of the error is caused by the position of the markers that are used to find the transformation function: The markers on the top left, bottom left and bottom right (marked in white).

The error in the transformed coordinates that are very close to a marker, should be dominated by the error in the position of that marker. If this is the case, the error in the transformed coordinates on the SEM should be 2 micron in both the x- and y-direction at those locations. $\sigma_{\text{tot}}^2 = \sigma_x^2 + \sigma_y^2$, so the total error in the predicted location is $\sqrt{8}$. In the Monte Carlo simulation, the error in the transformed coordinates and the error in the landing position of the SEM stage are added. The error in the landing of the SEM stage will also be 2 micron in both the x- and y-direction. The total error close to a marker should therefore be $\sqrt{\sqrt{8}^2 + \sqrt{8}^2} = 4$. In Fig. 3.7 it can be seen that the 3σ value close to the markers is approximately 12 micron, so indeed σ = 4 micron here.

In the simulation, the error in the predicted position of particles that lie between the markers is the smallest. This suggests that the markers should be applied at the edges of the blank, to achieve a high position accuracy on the entire blank. However, this is only valid if the stages of the imaging platforms are indeed accurate. If this is not the case, interpolations of the markers are not necessarily more accurate than extrapolations. In general, the overall accuracy of the fiducial marker system can be improved by using more than 3 marker positions to find the transformation function.

3.1.6. Previously tried markers

The concept of operations is concluded by looking at the markers that were previously tried on blanks in the Rapid Nano and a scanning electron microscope. There is a record of three types of markers. The pros and cons of each type has been discussed with an expert on the Rapid Nano.

The first attempt at a fiducial marker for blanks was a **marker from permanent ink**. These marker consists of a line with a dot at the end, like an exclamation mark, that is manually drawn on the blank as finely as possible. The dot has a diameter of approximately 100 µm. Three of these markers are applied on the blanks. If the sample is cleaned the markers will disappear, but cleaning is not necessary because this method barely causes contamination. Applying these markers is easy and cheap, however the accuracy in position that these markers provide (tens of micron) is not sufficient. This is visible in Fig. 3.8: In the scanning electron microscope image the marker does not provide a distinguishable reference point and in the Rapid Nano image the scatter pattern is very erratic.

A second attempt consisted of small square pits of 2 × 2 × 2 µm **markers that are milled in the substrate with a focussed ion beam** (FIB). (See Fig. 3.9) 6 of these pits are distributed across the blank. Because of their small size, these markers are accurate but it also makes them difficult to find in the scanning electron microscope. In the Rapid Nano images it is difficult to distinguish the markers from particles. For the FIB process the sample needs to be in a vacuum. During the pumping and venting of the vacuum chamber the blank can be contaminated. However, the sample can be cleaned after the FIB process without damaging the markers.

The final previously tried fiducial marker was a **direct laser written marker**. This marker consists of a large cross and a series of dots with a diameter of 25 µm, spaced 50 µm apart. Fig. 3.10 shows a Rapid Nano and an optical image of this marker. In this design the markers are easy to find and the corners of the cross provide an accuracy of around 1–2 µm in optical and SEM images. In the Rapid Nano however, a problem arises at the high laser intensities that are needed to detect small particles: The markers produce too much scattering, which results in a blurry image. It is possible to produce smaller dots if an UV laser is used: The minimal writing sizes of this laser is 1–2 micron.

The problems with all the previously tried markers can be summarised as follows: The markers are not both easily visible ánd accurately localisable on all imaging platforms. This is visualised in Table 3.1.

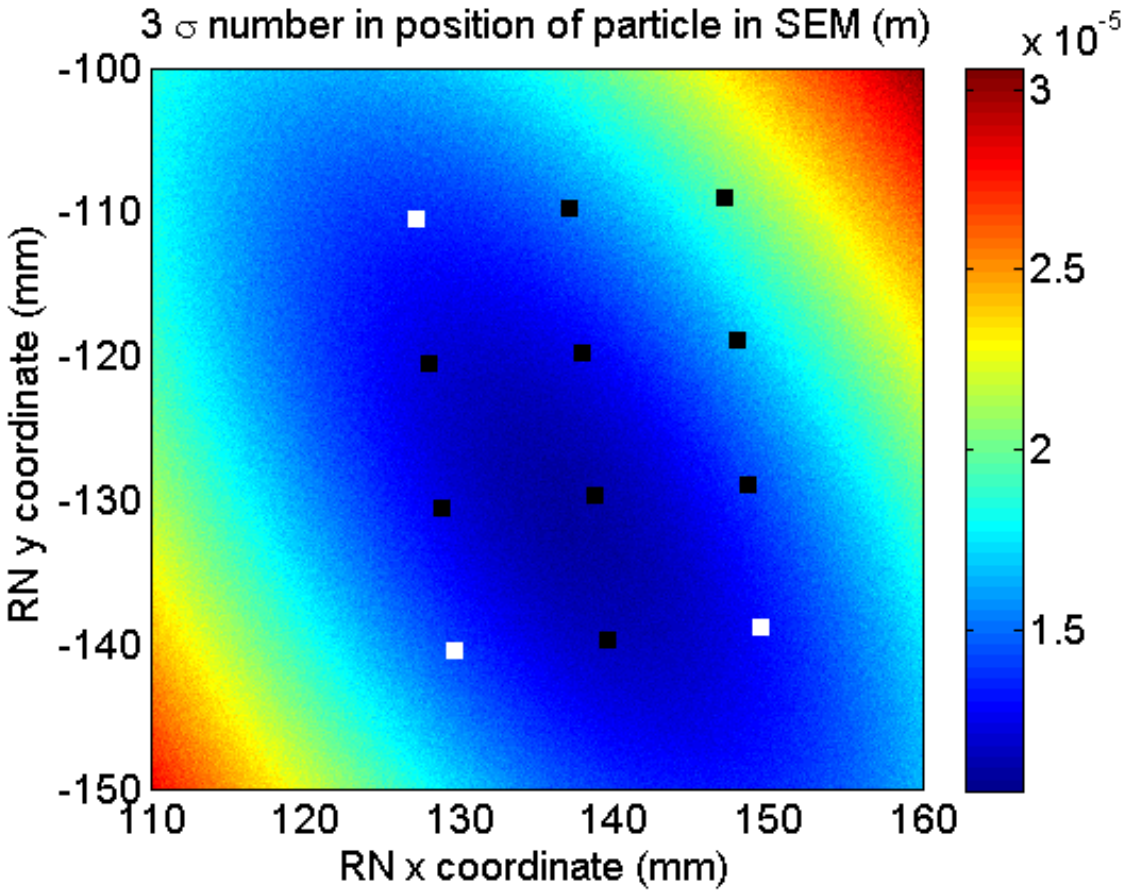

Figure 3.7: The 3σ plot for the pinpointed position of a particle in the scanning electron microscope. 99.7% of the particles will be located within a radius of the 3σ number from their pinpointed position. This plot is the results from a Monte Carlo simulation with a sample size of 100. The standard deviation in Rapid Nano position was taken as 1 micron and the standard deviation in the SEM as 2 micron. The squares indicate the position of the 12 makers on the sample. The markers that are used to find the transformation function are coloured white. The chosen markers cause the diagonal shape of the plot.

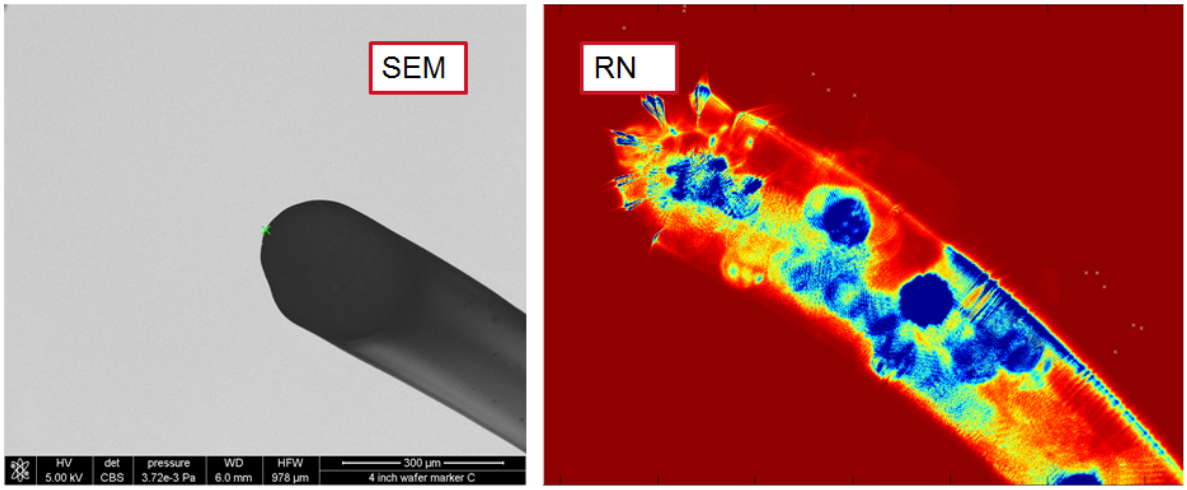

Figure 3.8: One of the previously tried fiducial markers is a marker from permanent ink. Here a scanning electron microscope and Rapid Nano image of such a marker is shown. The Rapid Nano image is falsely colored: Red corresponds to a low and blue a high measured light intensity. The markers are manually drawn as finely as possible. Still they are at least 100 micron wide. This makes them easily visible in both systems, but they are not accurately localisable.

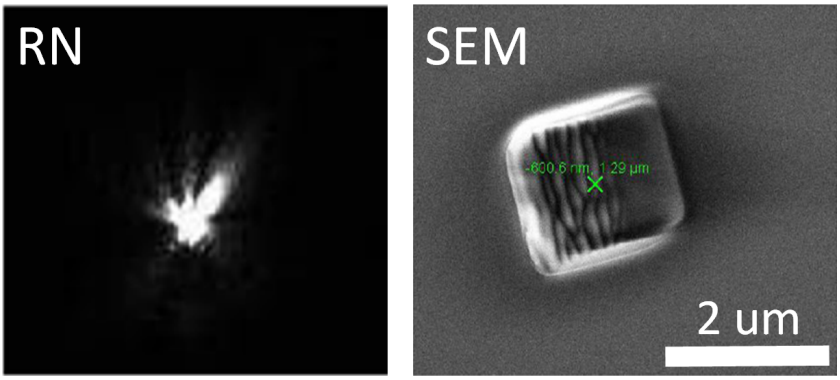

Figure 3.9: A second tried fiducial marker are these small wells that were made with a Focussed Ion Beam in the silicon substrate. A Rapid Nano image and scanning electron microscope image are shown. Because these markers are so small, they are accurately localisable, but difficult to find/distinguish in the SEM and Rapid Nano.

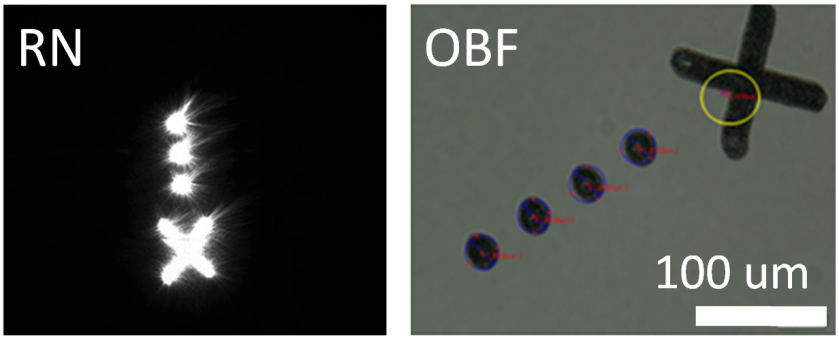

Figure 3.10: The final previously tried fiducial markers were directly written with a laser. Here Rapid Nano image at 0.10 W laser power and an optical bright field image are shown. These image are quite big. This makes them easily visible in all system. However, the markers scatter too much in the Rapid Nano, which makes it impossible to accurately localise them in this system.

Table 3.1: This overview of the previously used markers summarises the shortcomings of these makers. The markers are not both easily visible ánd accurately localisable on all imaging platforms. Note that the atomic force microscope is not present in this overview, because it has not yet been used in combination with the Rapid Nano.

	Rapid Nano		**SEM**	
Marker	**Easily visible?**	**Accurately localisable?**	**Easily visible?**	**Accurately localisable?**
Permanent ink	Yes	*No*	Yes	*No*
FIB	*No*	Yes	*No*	Yes
Direct laser write	Yes	*No*	Yes	Yes

3.2. Requirements

From the concept of operations in the previous section, a list of requirements for the fiducial markers and the fiducial marker system was drafted. The requirements roughly fall into one of three categories: Size and shape, material, location. The remaining requirements concern the fabrication, contaminating properties and lifetime of the fiducial marker system. In this section, all the requirements are listed per category.

3.2.1. Size and shape

- It is important that a fiducial marker possess a well defined and distinguishable point that can be used as reference point. (E.g. a small dot or two crossing lines.) The accuracy of the reference point eventually determines the error in the predicted position of the defects.
- The marker shape should be a-symmetrical, so that information about the position and orientation of the marker is provided at a glance.
- The markers should not posses features that scatter too much, to prevent saturation of the CCD camera in the Rapid Nano.
- The markers should be easily distinguishable from particles in the Rapid Nano.
- The markers should consist of at least 10 pixels in the biggest FOV of a SEM. This corresponds to approximately 10 µm.
- To be clearly visible in SEM, AFM and optical microscopy (used in AFM), the markers should provide topographical contrast: Ideally they posses steep walls of at least 10 nm.
- The markers should not be too high (between 10–100 nm), to prevent long AFM scanning times and damage to AFM tip.

3.2.2. Material

- To increase the visibility of the markers in SEM and optical microscopy (used in AFM), it is ideal if the markers also provide material (and possibly doping) contrast.
- The material that the marker is made of, should be compliant with processes that are used in the semi-conductor industry. This is because the blanks will be used to qualify tools from external parties, and they want to prevent that their tools are contaminated with these materials. More information on this subject will be provided in section 3.3.3.
- The markers should be made of a conducting material, to prevent charging in SEM.
- And the material should be incompressible, so that height measurements in AFM are reliable.

3.2.3. Location

- A sample should contain at least 3 markers, to span the vectors that are needed for the coordinate translation. (See section 3.1.5)
- The AFM cantilever should be able to reach the location of the markers on the sample.

3.2.4. Fabrication, contamination and lifetime

- The fiducial marker system should be cheap to fabricate.
- The marker system should not cause (too much) contamination of the sample. If the sample is contaminated during the fabrication, it should be possible to clean the sample without removing the markers.
- The marker system should be durable and stable.

3.3. Design

Using the list of requirements in the previous section, a design for the fiducial markers and the fiducial marker system was made. This design is presented in section 3.3. This section also discusses how the design meets the requirements. It also explains which parameters can be tuned to optimise the fiducial marker system.

3.3.1. Design for the markers and the marker system

In the design for the fiducial marker system, 12 markers are spread across the blank wafer, as shown in Figure 3.12. The markers are placed at right angles with a pitch of 20 mm.

Each marker consists of an elongated cross, a T- or L-shape of 20 µm thick, that is combined with one or two triangles that points to the “north side” of the blank wafer. Every marker has a unique shape, so they are distinguishable from one another. If the design and the distribution of the markers on the blank wafer are known to the operators of the imaging platforms, the unique design of the markers will help the operators to find the markers they want to use to calculate the transformation function. Once a single marker is found, it is easy to locate the other markers.

The design combines large and small features, so that the markers are both visible ánd accurate on the Rapid Nano, the scanning electron microscope and the atomic force microscope.

The large features are provided by the big surface of the fiducial marker. The markers are made from a different material than silicon, so the marker has material contrast. In this work, the markers are made from gold and platinum. In section 3.3.3 the selection of the material for the markers is discussed. Because the markers are applied on top of the substrate, they have raised edges that also provide topological contrast.

The small features are provided by small dots on the marker surface, with a diameter of approximately 150 nm. In the centre of each marker 5, 4 or 3 small dots are located. The central dot is used as the reference point of each marker.

3.3.2. Optimising the design

The designed markers are very visible in the bright field scanning electron and optical microscopy images. But they should also be nearly invisible (“stealth”) in the optical dark field of the Rapid Nano. To decrease the scattering of the markers in the Rapid Nano, certain parameters of the marker design can be optimised: Specifically the material and the height of the fiducial markers.

The height and material of the fiducial markers were optimised with experiments and the finite element model that is described in Chapter 2. The results of the optimisation are presented in Chapter 5.

Based on the list of requirements, the height of the markers can lie between 10 and 100 nm. The possible materials for the markers will be treated in the next section.

3.3.3. Material selection

The list of requirements for the material of the marker (provided in section 3.2) was supplemented with additional requirements for this specific marker design. These extra requirements ensure the used material is compatible with the marker design and fabrication method:

- The materials have to be available for thermal or e-beam evaporation in the clean room facilities of the VLL.
- They should be non-toxic and non-flammable.
- They should adhere well to silicon substrate.
- They should form a smooth surface.
- They should not form oxides.

A list of all possible materials was made and assessed on every requirement. To acquire this knowledge, scientific and technical staff of TNO, the Kavli Nanolab and Else Kooi Lab were interviewed. The material contrast with respect to a silicon background was determined with scanning electron microscope and optical images of the sample pictured in Fig. 3.13.

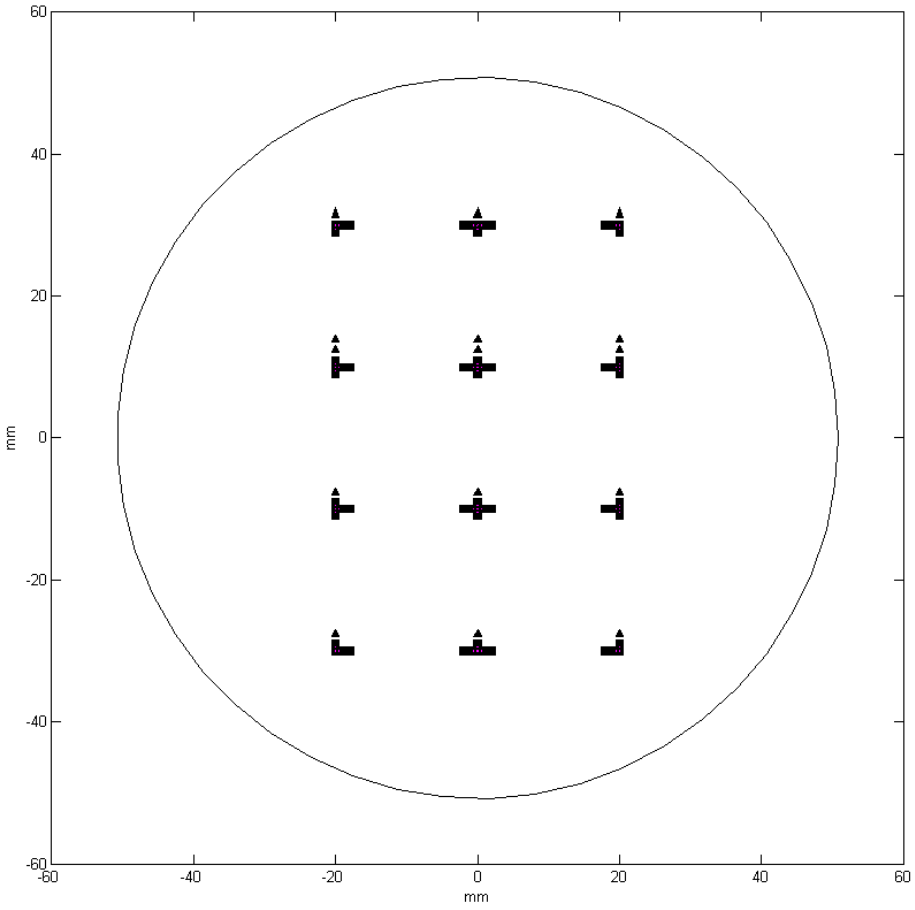

Figure 3.11: This is an overview of the fiducial marker system design. 12 markers are spread across a blank 4” wafer. Every marker has a unique shape. In this image the location of the markers corresponds to their real location on the wafer, but their size is 50× bigger, to properly show the unique shape of each marker.

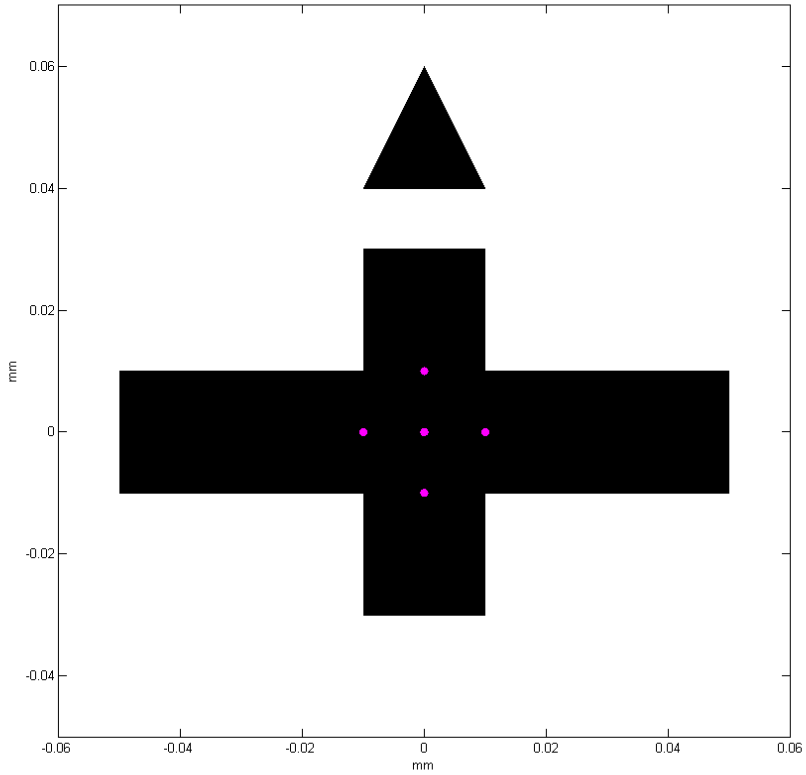

Figure 3.12: The design of a fiducial marker. The marker consists of a 20 micron thick elongated cross with a triangle that points to the “north” of the sample. These large features make the marker easily visible on all imaging platforms. The small dots in the centre of the marker are used to accurately localise the marker. For the sake of visibility, the small central dots are displayed 10× larger in this image: their real diameter is 150 nm.

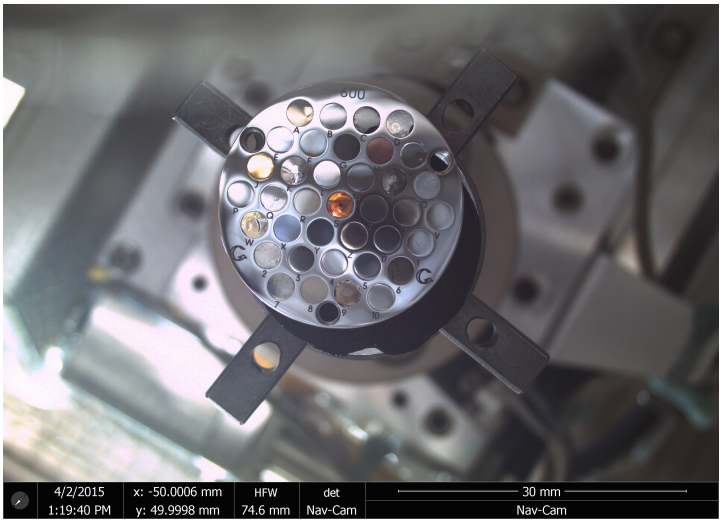

(a) Image taken with the navigation camera in a scanning electron microscope.

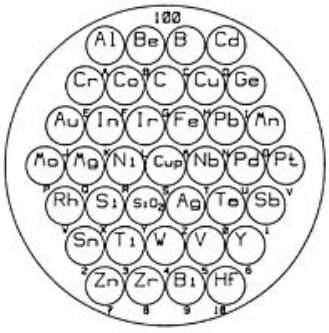

(b) Schematic drawing of the sample, to indicate the different elements.

Figure 3.13: Many materials were considered for the fabrication of the fiducial markers. This sample with 36 elements, was used to determine the material contrast of these elements in a scanning electron microscope. The diameter of the complete sample is approximately 2 cm.

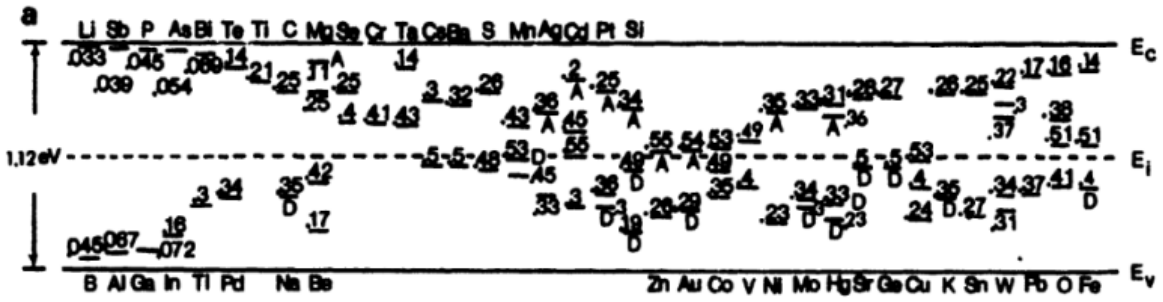

Figure 3.14: The ionisation energies for various impurity levels in silicon. Gold and platinum lie in the middle of the silicon band gap. This is one of the reasons the semi-conductor industry does not want to use these elements. Image source: Li [14].

The compliance with semi-conductor industry proved to be a difficult requirement. Materials that have a high diffusion rate and solubility in semi-conductors (e.g. Cu), are undesired in the semi-conductor industry, because contamination of this kind will spread through wafers quickly. But more importantly, the industry wants to avoid impurities in their systems that can change the physical (e.g. electrical, optical) properties of the semi-conductors. Obvious examples of these materials are dopants, such as Sb, B or P. Materials whose ionisation energies lie in the middle of the band gap of silicon and other semi-conductors, are also avoided. Impurities of this material can form a re-combination centre in the semi-conductor. Examples of these materials are Fe, Cr, Au, Pt and Cd. (See Fig. 3.14)

In the list of possible materials, there is not a single material that complies with all requirements. Gold and platinum turn out to be the best possible match. They can meet every requirement, except the compliance with the semi-conductor industry standards.

Although gold and platinum do not adhere well to a substrate if they are applied directly on top of silicon, this can be solved if a thin interlayer of chromium is used. Therefore every sample that is fabricated in this work uses an interlayer of chromium of 5 nm thick. If the height of e.g. a gold marker is indicated as 50 nm, the marker is really made from 5 nm chromium, with 45 nm gold on top.

4

Experimental approach

In the following section (4.1) the principles of the techniques that were used to fabricate the markers are explained. In the second section (4.2) the method for the validation of the marker system is treated.

4.1. Cleanroom materials and methods

The most conventional technique to build nano-structures is called the **top down approach**. This approach is used in research and the semiconductor industry because it is scalable and tunable. The fabrication always starts with a substrate. Parts of the substrate are removed and new layers of material are added in a series of steps, to produce a structure. The process can be compared to a rock were material is removed to produce a statue. Because nano-structures are extremely susceptible to particle contamination, all these processes happen in a 'dust-free' environment: a so called **cleanroom**.

Is is outside the scope of this thesis to treat all existing cleanroom techniques: Only the ones that were used for the fabrication of the markers are explained: Electron beam (e-beam) lithography, e-beam evaporation and the lift-off technique. Background on their working principles is provided. Special attention is paid to why these techniques are preferred over alternative methods and what their limitations are for this specific application.

All fabrication steps in this work were performed in the cleanrooms of the Van Leeuwenhoek Laboratory (VLL). Specific recipes and used settings can be found in appendix B of this report.

4.1.1. Electron beam lithography

Lithography is a technique used to transfer a pattern onto a substrate: First a thin layer of polymers (called **resist**) is applied to the surface of a **wafer** (a thin slice of silicon, used as substrate). Then parts of the resist are **exposed** to energetic particles (e.g. photons, electrons, ions). Due to interactions with these particles, the composition of the exposed resist changes. After the exposure the substrate is rinsed with a special solution, that is called developer. Depending on the type of resist that was used, either only the exposed or the unexposed resist will solve in the developer. (See Fig. 4.1) This step is called the **development** of the resist.

The different types of resist are called **positive** and **negative tone**. In a positive tone resist exposure will cause polymer bonds to break, softening the resist. (See Fig. 4.2a) During the development, the exposed areas are removed. In a negative tone resist however, exposure causes more cross linking, resulting in a tougher layer of polymers. (See Fig. 4.2b) During the development, only the exposed areas remain on the substrate.

Fig. 4.3 shows the **dose response curves** of a positive and negative tone resist. These curves show the thickness of developed resist, after exposure to a certain dose of energetic particles. Dose is given in units mJ/cm^2 at a given wavelength for lithography with photons or in $\mu m/cm^2$ for lithography with electrons or ions. The **sensitivity** of a resist is the minimum dose required to form the desired pattern in the resist after the development. Specifically for a positive resist, the **dose to clear**, D_0, is the dose that is required to just clear the resist in a large area for a given process.

In this work electrons were used for the exposure step. This is called **electron beam**, or e-beam, **lithography**. The advantage of e-beam lithography over lithography with photons is the fact that it is a

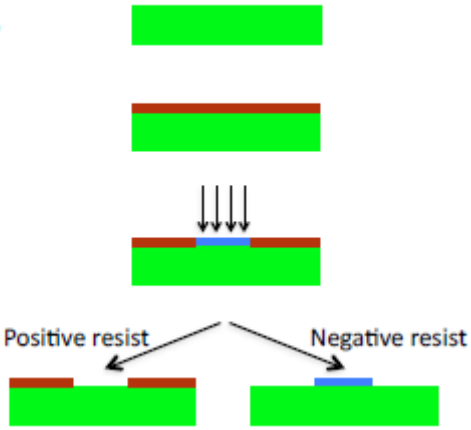

Figure 4.1: In lithography a substrate is spin coat with resist. Part of the resist is exposed to energetic particles and developed. If a positive resist is used, the unexposed areas will remain after the development, while for a negative resist the exposed areas remain. Image source: Nanotechnology lecture slides.

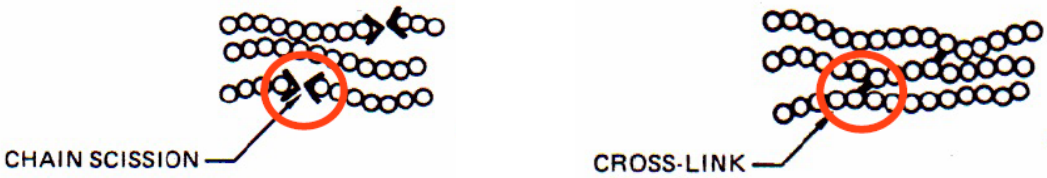

(a) In a positive tone resist, chain scissions during the exposure soften the resist.

(b) In a negative tone resist, crosslinking during the exposure makes the resist more tough.

Figure 4.2: Image source: Nanotechnolgy lecture slides.

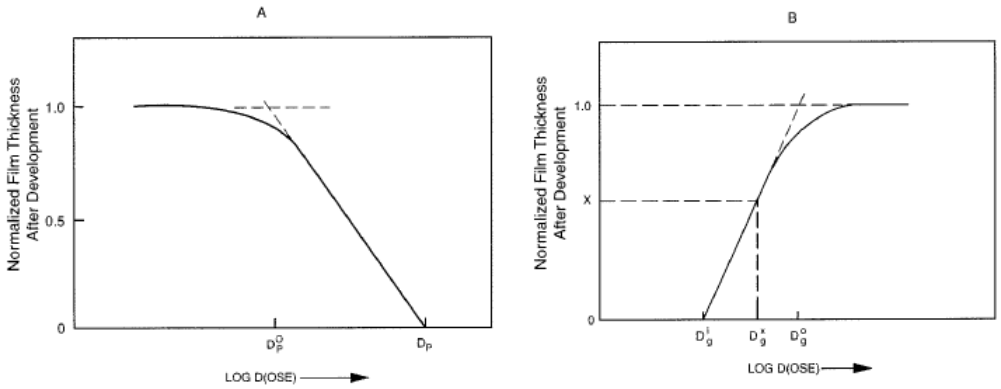

Figure 4.3: Typical response curves or sensitivity curves. a) For a positive resist. The contrast γ_p is determined from the slope. The contrast for a positive resist is solvent dependent. b) For a negative resist. The value of D_g^x, usually occurs at 0.5 to 0.7 normalized thickness. Image source: Madou [16].

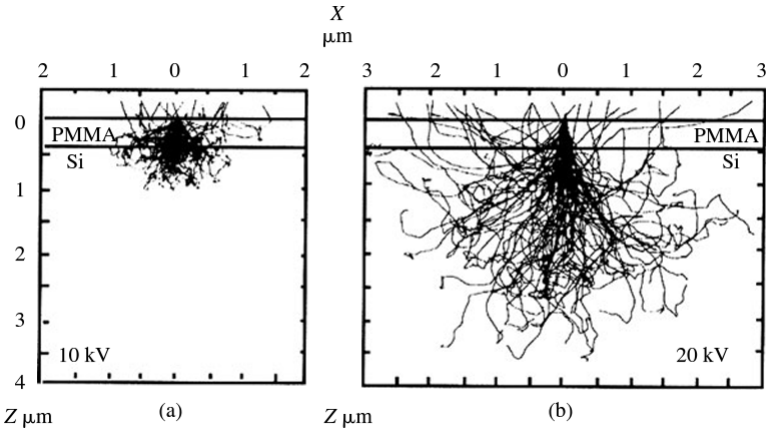

Figure 4.4: Electron scattering trajectories calculated for a tightly focused spot on a PMMA layer on silicon for a) a 10 kV beam and b) a 20kV beam. Scattering of electrons results in a much broader feature in the exposed resist at the higher voltage. This is called the proximity effect. Image source: Lindsay [15].

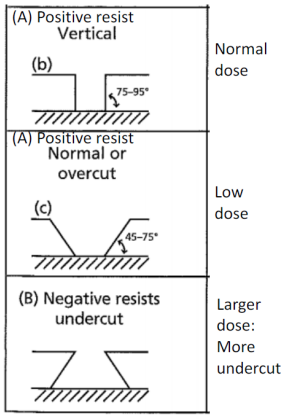

Figure 4.5: Negative resist have a naturally occurring undercut, while a positive resist has normal or overcut. Image source: Nanotechnology lecture.

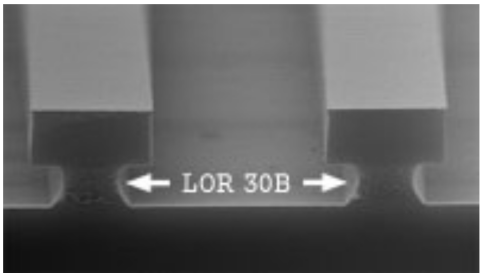

Figure 4.6: To create an undercut with a positive resist, a trick is used: A double layer of resists with different sensitivities. Image source: Nanotechnology lecture.

direct-write method: There is no need to make an expensive mask that is used as a template, because electrons are charged and they can be directed using electric and magnetic fields. This makes it easy to implement changes in the lithography design.

As explained in section 2.1.2, a beam of electrons provides a good resolution, depending on the energy of the electrons. In e-beam lithography however, the writing resolution is decreased by the scattering of primary electrons: While exposing a part of the sample, its surrounding areas will also receive an unintentional dose. This is called the **proximity effect**. (See Fig. 4.4)

If a positive resist receives a normal dose, the walls of the resist will be vertical after development. For a low dose however, the dose to clear will not have been reached and this results in slanted walls: also called **overcut**. In a negative resist the opposite happens: areas next to the exposed areas will also receive a small dose, due to the proximity effect. After development this causes receding walls: an **undercut**. The higher the dose, the larger this effect. (See Fig. 4.5) It is also possible to create an undercut while using a positive resist: To achieve this, resists with different sensitivities are layered. An example is shown in Fig. 4.6.

Some resists have the property that they behave both as a positive and a negative tone resist. *Polymethyl methacrylate* (PMMA) is such a **dual-tone resist**. The dose response curve of PMMA for both helium ion and electron beam exposure are shown in Fig. 4.7. Here it is visible that PMMA initially behaves as a positive resist, but if it is **overexposed**, the polymers will form cross-links again. If these overexposed regions are developed, the resist will have a thickness of approximately half of the initial

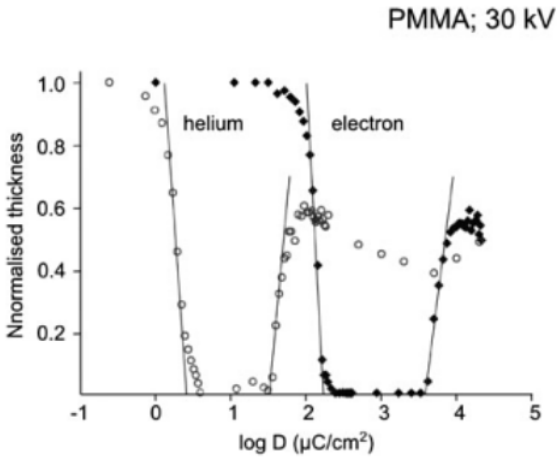

Figure 4.7: Dose response curves of PMMA for He+ and electron exposures at 30 keV. The sensitivity of PMMA scales roughly with electron accelerating voltage. The critical dose at 50kV, for example, is about twice the critical dose for 25kV exposure. So the electron dose data displayed here, is obtained from measured 100 keV data and scaled down by a factor of 100/30. Image source: Stepanova and Dew [27].

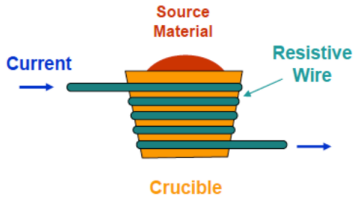

Figure 4.8: Schematic overview of the way metal are heated in thermal evaporation. Image source: Nanotechnology lectures.

resist layer thickness. PMMA was used as resist in the fabrication of the fiducial markers: its dual-tone property was used to make the small dots in the centre of the marker by overexposure.

4.1.2. Evaporation

There exist many methods to apply thin films of material on substrates. One of them is **physical vapor deposition** (PVD). Different techniques fall in the PVD category, for example: Sputtering, thermal- and e-beam evaporation. With all these techniques the substrate is placed some distance from the material source, inside a pumped vacuum chamber.

Thermal evaporation can be performed with low melting point metals as the material source. The metal is placed inside a crucible, which is heated by a current that flows through a dissipative wire. (See Fig. 4.8) The heated metal will evaporate and travel to the substrate, where the atoms will bind to the surface. Contamination can be a problem in thermal evaporation: During the heating process the container material can also evaporate and land on the sample.

Instead of heating the source material through the crucible, it can also be heated locally by a focused beam of electrons. (See Fig. 4.9) This is **e-beam evaporation**, which can be done with the same materials as used in thermal evaporation, but also with dielectrics and materials that have a higher melting point.

For both types of evaporation a low pressure inside the vacuum chamber is needed, to reduce the amount of re-directing collisions with air particles. This lack of collisions causes a **directionality**: The incident particles will all reach the substrate under the same angle. (See Fig. 4.10) If there are already structures on the substrate, this directionality can result in shadowed areas where no material is deposited. The result is called a **non-conformal layer** of material. The conformality and uniformity of the deposited film can be improved by rotating and heating the substrate during the deposition of the material.

In **sputtering** the source material is bombarded with a beam of energetic ions. Material is chipped

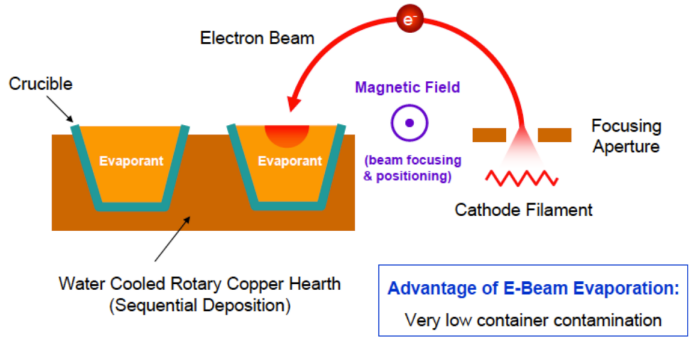

Figure 4.9: Schematic overview of the way materials are heated in E-beam evaporation. Image source: Nanotechnology lectures.

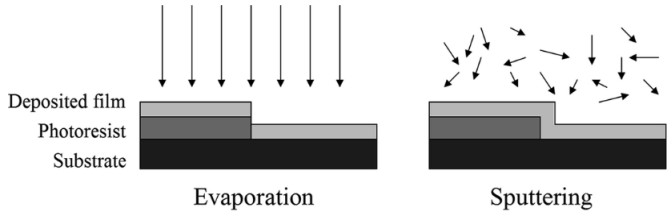

Figure 4.10: Because of the low pressure, evaporation is directional. The resulting layers are non-conformal. Sputtering however is non-directional and results in a conformal layer of deposited material. Image source: Labeed and Fatoyinbo [13].

away and flies to the sample to be coated. The material flies away in all directions, so sputtering is **non-directional**.

There exist three different **growth modes** for thin films: (See Fig. 4.11)

1. Layer-by-layer growth (Also called Frank van der Merwe mode). In this mode the deposited material will be arranged in atomically smooth, fully formed layers that are stacked on top of each other.

2. Island growth (Volmer Weber mode): The material will grow in clusters, resulting in a rough surface.

3. Mixed growth (Stranski Krastanov mode): Initially the material will grow in layers. Beyond a certain critical layer thickness islands will form on top of the layers.

The applicable growth mode depends on the surface wetting properties of the substrate and the deposited material. Because rough substrates cause extra scattering in the Rapid Nano, it is important that the surface of the fiducial markers are uniform and smooth. This should be kept in mind during the deposition of the metal.

As discussed above, the deposition of material happens at high temperature and low pressure. However, if the sample is taken out of the deposition tool, it will be at atmospheric pressure and room temperature again. This difference in pressure and temperature can cause **film stress** in de deposited layer.

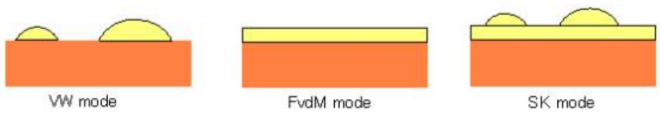

Figure 4.11: Thin films can grow in different modes: Volmer Weber mode, Frank van der Merwe mode of Stranski Krastanov mode. Image source: Nanotechnology lectures.

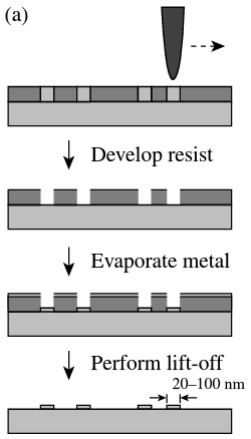

Figure 4.12: This image shows the sequence of steps required perform lift off. First a substrate is patterned with lithography. After development of the resist, metal is evaporated. Then the remaining resist and metal on top of this resist are removed. The metal that was evaporated directly on the bare substrate remains. Image source: Lindsay [15].

4.1.3. Lift off

Fig. 4.12 shows a schematic overview of a **lift off process**: First a pattern is written in resist with lithography. After development a layer of material is deposited. Then the sample is soaked in a solvent: Starting at the corners of the resist profile, the resist layer will dissolve and with it the material lying on top of the resist will be released. Only the material that was deposited directly on top of the bare substrate will stay adhered and remains after lift off.

In order for the resist to properly dissolve, the side edges of the resist profile should not be covered during the deposition step. Therefore a resist with an undercut and directional material deposition are beneficial for lift off processes. For the fabrication of the fiducial markers, the undercut was provided by a double layer of PMMA with different sensitivities. E-beam evaporation ensured a directional material deposition.

A difficulty with lift off is material **re-deposition**: Material that first lies on top of the resist, can re-deposit directly on the substrate during the removal of the resist. This material then becomes very difficult to remove from the substrate and it will contaminate the sample. Because this process is difficult to control, lift off is considered more as a research- than as an industrial production tool.

4.2. Validation of fiducial marker system

In order to validate the fiducial marker system, the re-detection rate of defects on blanks with the fiducial marker system is determined. To this end, programmed defects are applied to the blank wafer. The programmed defects consist of ellipses and rectangles of different sizes (diameters from 50 nm to 2 micron) and with different aspect ratio's (1:1, 1:2 and 1:5). They are placed in 12 fields, that are spread across the wafer. (See Fig. 4.13)

The programmed defects will be re-detected on a scanning electron microscope and an atomic force microscope, following the procedures that are described in Chapter 3, specifically the flowcharts in Fig. 3.3 and 3.5. The percentage of particles that are re-detected is calculated. If a particle is re-detected, the distance between its predicted position and its real position is measured. This distance can be used to calculate the area that needs to be searched before the defect is found.

On both platforms at least 30 particles will be re-detected, so the average difference in distance can be calculated. This average should correspond to the error in the pinpointed position that is calculated with the Monte Carlo simulations in section 3.1.5.

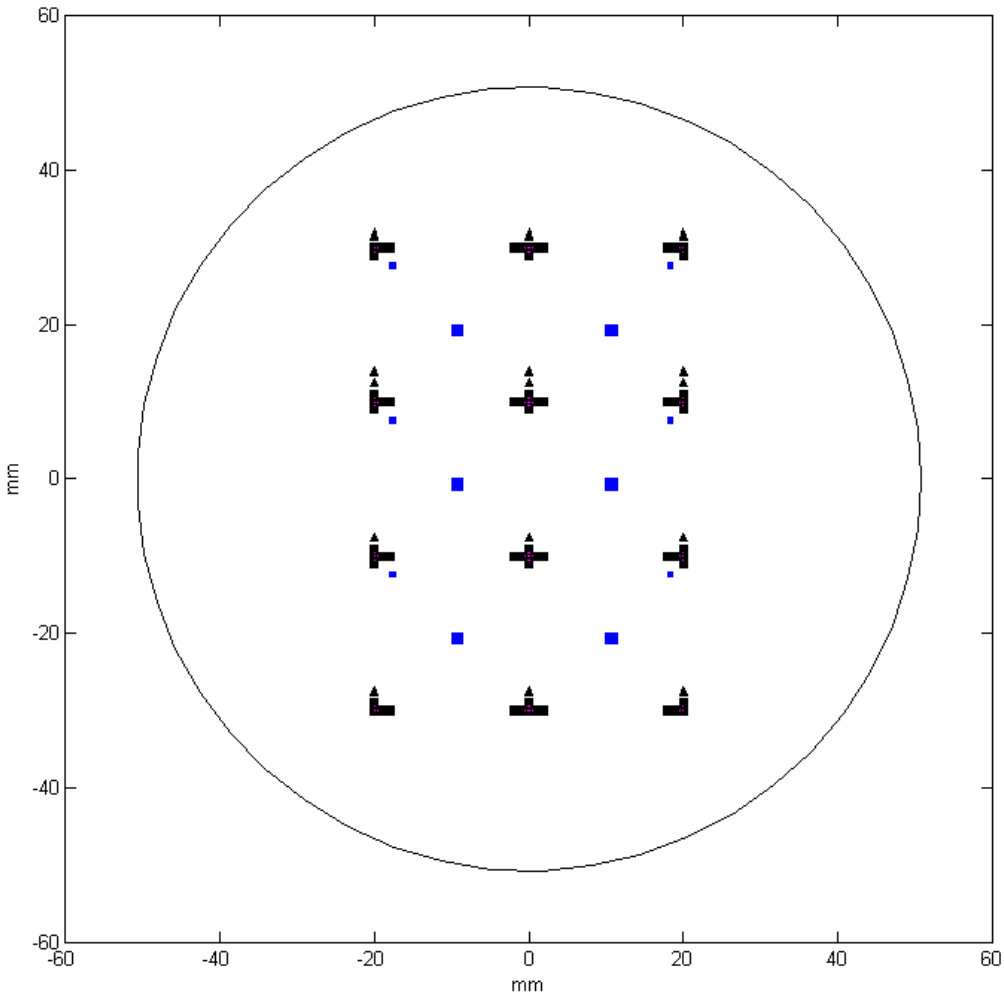

Figure 4.13: In order to validate the fiducial marker system, programmed defects are applied to the blank. These programmed defects will be re-detected in the scanning electron microscope and the atomic force microscope, so the re-detection rate with the fiducial marker system can be determined. This schematic overview shows the location of 12 fields with programmed defects (in blue) on a blank, with respect to the location of the fiducial markers.

5

Experimental results

In this chapter the results of the (computational) experiments that were performed in the context of this thesis are presented and explained.

The first section (5.1) discusses the COMSOL simulations. It explains which compromises were made to keep the computation time and memory within reasonable bounds. The simulations were made to optimise the material and the height of the markers, so they scatter less in the Rapid Nano. The optimised parameters are presented here.

Section 5.2 shows the results of the experiments where the height and material of the fiducial markers were varied. The experiments confirm the findings of the COMSOL model.

In section 5.3 the results on the visibility and positioning accuracy of the makers in the Rapid Nano, the scanning electron microscope, and the atomic force microscope are shown.

The increase in re-detection efficacy due to the fiducial marker system was quantified, by re-detecting programmed defects in a scanning electron microscope and an atomic force microscope. The results are presented in section 5.4.

Finally, the lifetime of the fiducial marker system that was used for the re-detection of the programmed defects is discussed in section 5.5.

5.1. COMSOL simulations

The COMSOL model that was described in section 2.3.1, was used to study the scatter from fiducial markers. To reduce the computation time, a two-dimensional model was used instead of a three-dimensional model. This 2D model corresponds to a cross-section of a marker that extents to infinity in the third dimension.

The modelled marker is based on the marker design that was shown in section 3.3. This means that the width of the modelled marker should be 20 µm. However, the domain size is coupled to the marker size: The bigger the marker, the bigger the computation domain. On the other hand, the mesh needs to be able to resolve the electromagnetic waves on the entire computation domain. Therefore the mesh should be finer than the used wavelength. (Usually $\lambda/6$ is used as the maximum size of the mesh elements.) If the real marker width (20 µm) is used, the domain is big in comparison to the maximum mesh size, so the needed number of mesh elements becomes very large. With so many mesh elements, the computation time and needed memory for the simulation become very large.

To keep the computation manageable, a trick was used: From Rapid Nano scans of the first fabricated fiducial markers (See section 5.3.1), it became clear that most of the scattering occurs at the edges of the markers. The light that hits the smooth surface in the middle of the marker is not scattered, but reflected. Because only the scattered light is of interest, the width of the simulated marker was reduced to a few micron. (See Fig. 5.1) This width gives a feasible number of mesh elements.

Because the corners of the marker are the features that scatter the most, the scatter from the marker can be approximated by two point sources placed at a distance (equal to the width of the marker) from each other. This is reminiscent of Young's double slit experiment and, as shown in Fig. 5.2, the light intensity in the far field also shows a diffraction pattern.

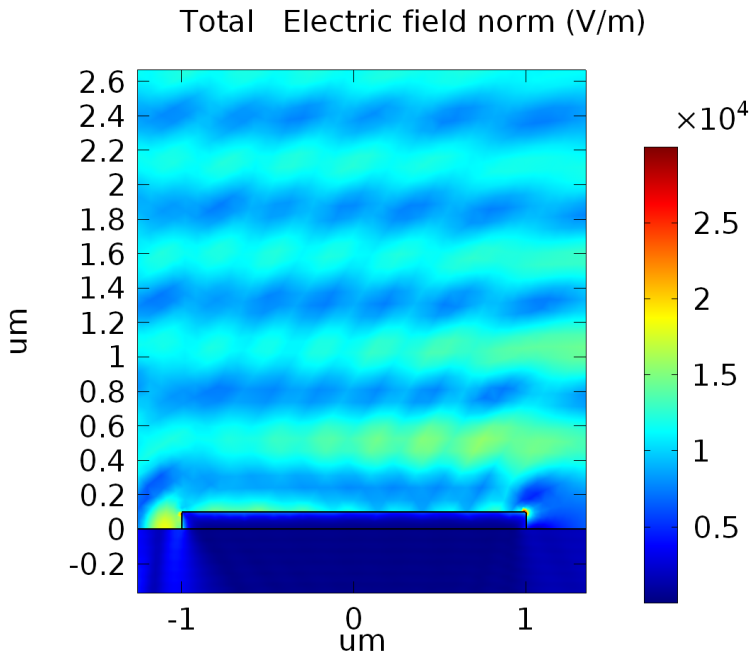

Figure 5.1: To reduce computation time in the COMSOL simulations, the markers are modelled by a 2D simulation with a reduced marker width. This image is zoomed in so that the marker, of 2 µm wide, is clearly visible. The surface plot shows the electric field norm of the total electric field. The total electric field is the sum of the background- and the scattered electric field. The highest electric field norm occurs at the upper corners of the markers. This is reminiscent of a double slit experiment.

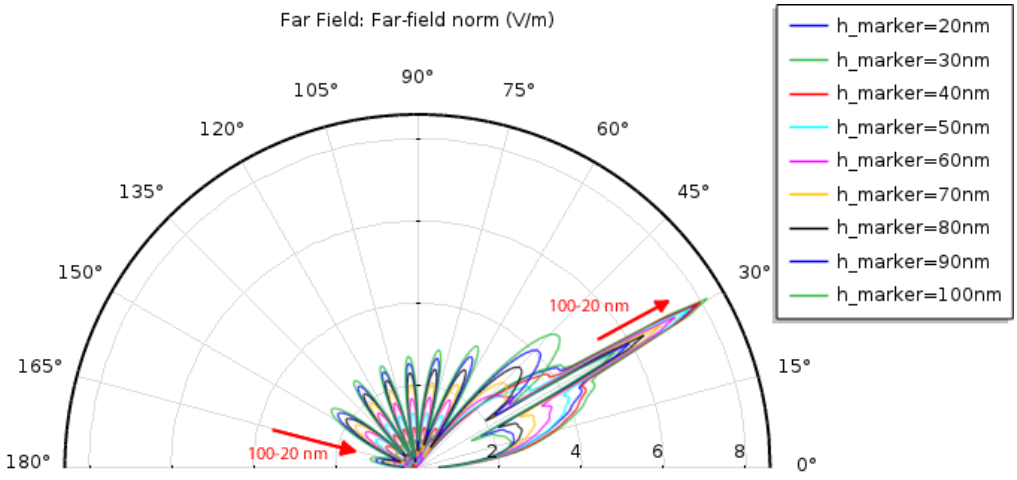

Figure 5.2: From the near field solution the far field solution is calculated. (As explained in Chapter 2) The norm of the electric field in the far field is plotted in a polar plot. The lower half plane corresponds to the electromagnetic waves that travel into the substrate. However, these waves are absorbed by a perfectly matched layer, so the corresponding far field is zero. Therefore only the upper half plane of the polar plot is shown. The incoming light has an angle of 60° with respect to the substrate normal, which corresponds to 150° in this plot. The large peak in the far field at 30° corresponds to the light that is specular reflected. The other peaks are a diffraction pattern coming from the scattered light, again reminiscent of a double slit experiment. In this simulation the marker width is set to 2 µm and the marker is made from gold. The far field norm is plotted for markers of different heights. As the height of the marker (denoted by 'h_marker') decreases from 100 nm to 20 nm, the amount of scattered light decreases, while the amount of the reflected light grows.

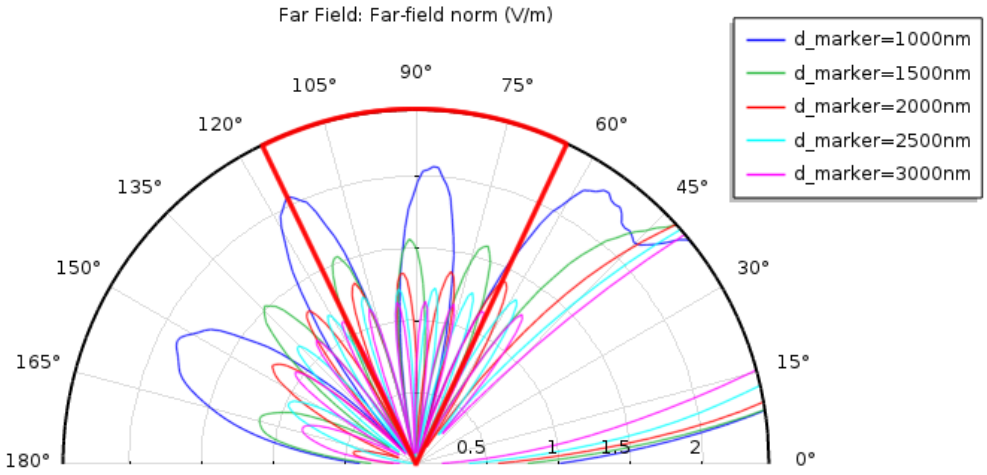

Figure 5.3: This plot shows the far-field norm for a gold marker of 50 nm high, with different simulated marker widths. The plot is zoomed in to show the small diffraction peaks more clearly, therefore the large peak caused by reflection at 30° is not visible. The diffraction pattern that is visible in the far field depends on the width of the marker: For wider markers, more and smaller diffraction peaks are visible, that are more finely spaced. The region indicated by the red lines, indicate the numerical aperture of the Rapid Nano. The far field is integrated over this numerical aperture, to quantify the scattered light that the Rapid Nano detects.

From the double slit experiment it is known that if the distance between the slits increases, the distance between the diffraction peaks will decrease. To study the effect of the marker width on the amount of scattering, the simulation was run multiple times for different marker widths, ranging from 1 to 3 micron. (See Fig. 5.3) Indeed, the same effect is visible in the scattering of the markers: The wider markers show more and smaller diffraction peaks, that are more finely spaced.

The amount of scattered light is quantified by integrating the far field over the angles that the Rapid Nano can detect. These angles are defined by the numerical aperture: NA $= n \sin \alpha$. The far field is defined in air/vacuum, which has a refractive index of 1, and the NA of the Rapid Nano is 0.42, so $\alpha = 24.8°$. This means that the far-field norm is integrated approximately from 65° to 115°. The power that is integrated over these angles in the far field, is plotted versus marker height for different marker widths in Fig. 5.4. In this plot it is visible that different marker widths yield a different amount of RN detected light. However, because the width of the simulated marker does not correspond to the real width of the markers, it is undesirable that the marker width affects the simulation outcome in this way.

To get more insight in the relation between the integrated far-field and the marker width, Fig. 5.5 shows a plot of the scattered energy per second versus marker width for different marker heights. It is clear that their relation is not linear: The plot shows some unexpected variation. This can be explained by looking at the edges of the window of integration in Fig. 5.3: At 65° and 115° the far-field norm is very dependent on the marker width. E.g. at 115° a marker width of 1000 nm gives a maximum, while a width of 2000 nm gives a minimum of the far-field norm. For different marker widths, the diffraction peak at the edges is either included or excluded from the integration. It is expected that the integrated far-field power converges as the marker width is increased, because the diffraction pattern becomes finer and finer. However, 3 micron is the largest marker width that can be computationally solved within a reasonable amount of time. From Fig. 5.5 it is not clear if the convergence has been reached yet at this point.

Therefore a new model was made, where no diffraction effect occurs: In this simulation, the left and right side of the marker are simulated independently. To achieve this separate simulation, the marker width was increased and the position was shifted to the left or the right of the computational domain. This way, the incoming light beam only hits one side of the marker. If the left side of the marker is illuminated, this is referred to as 'step up' and if the right side is illuminated, this is reffered to as 'step down'. Fig. 5.6 shows the background field of a step up simulated marker.

The results of the separate simulations for a gold and a platinum marker are plotted in Fig. 5.7. In this plot it is clearly visible that the step up side scatters less than the step down side of a marker.

This surprising difference in scatter between step up and step down can be explained in the following

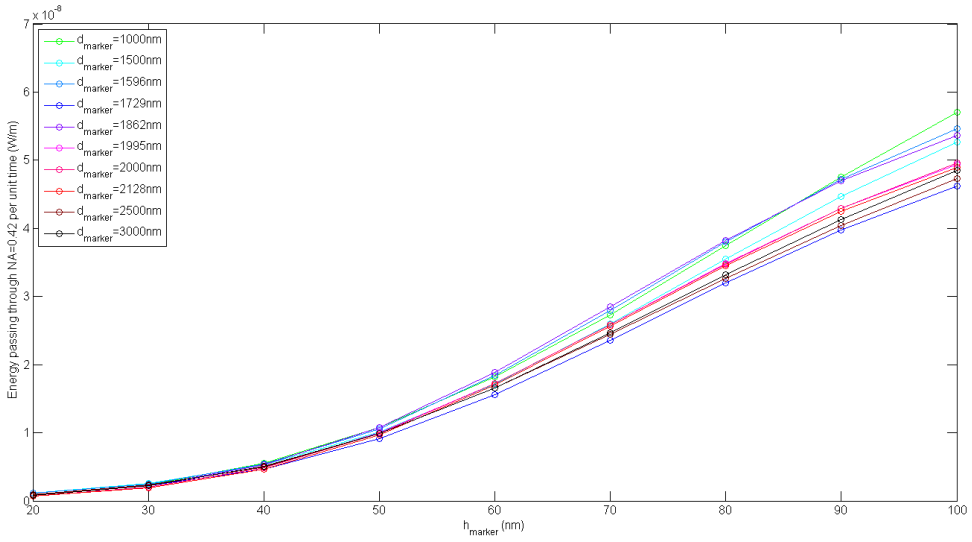

Figure 5.4: To quantify the amount of scatter that the Rapid Nano detects, the far field in the COMSOL simulation is integrated over the numerical aperture of the Rapid Nano. This integrated value corresponds to power that passes through the numerical aperture. Because this is a 2D simulation, the marker extents to infinity in the third dimension. Therefore the unit of the integrated number is W/m: The power is calculated per unit length in the third dimension. In this plot it is visible that the detected scatter increases as the marker height is larger. However, simulations with markers of different widths (corresponding to the different coloured plots) give rise to unwanted variations.

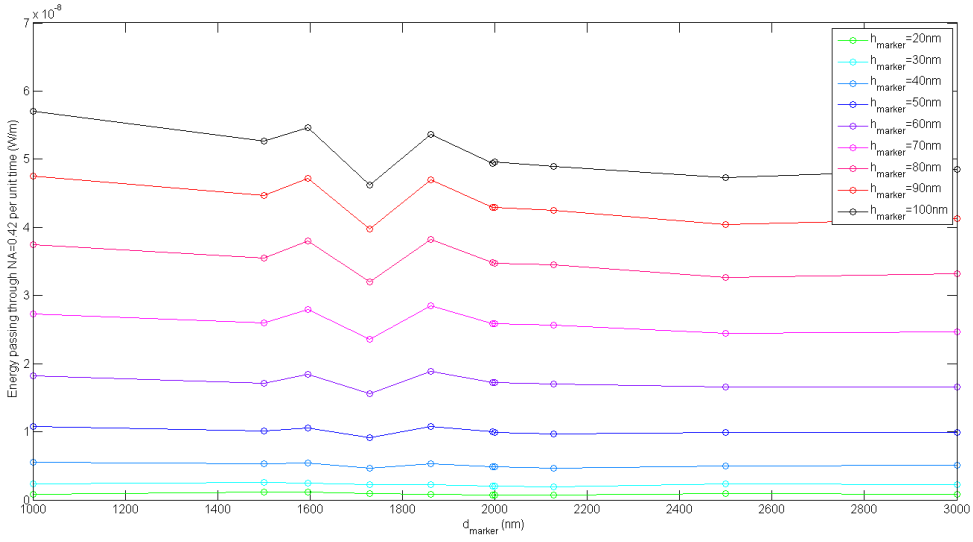

Figure 5.5: Here the power per meter that passes through the numerical aperture of the Rapid Nano is plotted versus the marker width, for different marker heights. The relation between the detected amount of scatter and the marker width is not linear, but shows deviations that are strange at first sight. These deviations can be explained by looking at the edges of the window that is used for the integration over the numerical aperture. (See Fig. 5.3) For a certain marker width a diffraction peak will be included in the integration, but if the width is changed slightly the diffraction peak will fall outside of the integration domain. Because the diffraction peaks become finer as the marker width increases, it is expected that the solutions will converge for very wide markers. However, from this plot it is not clear if the solution has fully converged for markers of 3 micron wide. For marker widths larger than 3 micron, the computation time and memory become too big to properly simulate.

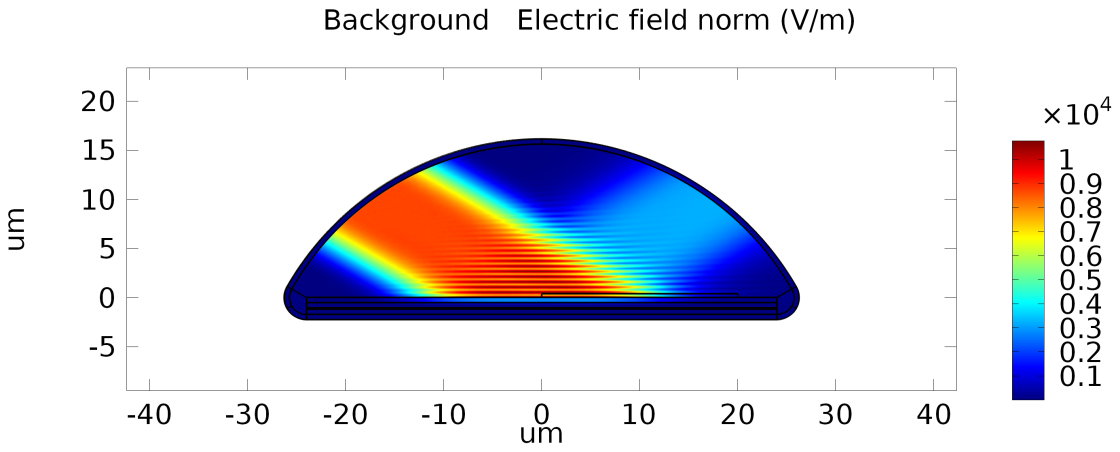

Figure 5.6: To circumvent the unwanted effect due to diffraction, the left and the right corners of the marker are simulated separately. The different corners are also called step up and step down. In these simulation only one of the corners is irradiated. This surface plot shows the background electric field norm for the step up case.

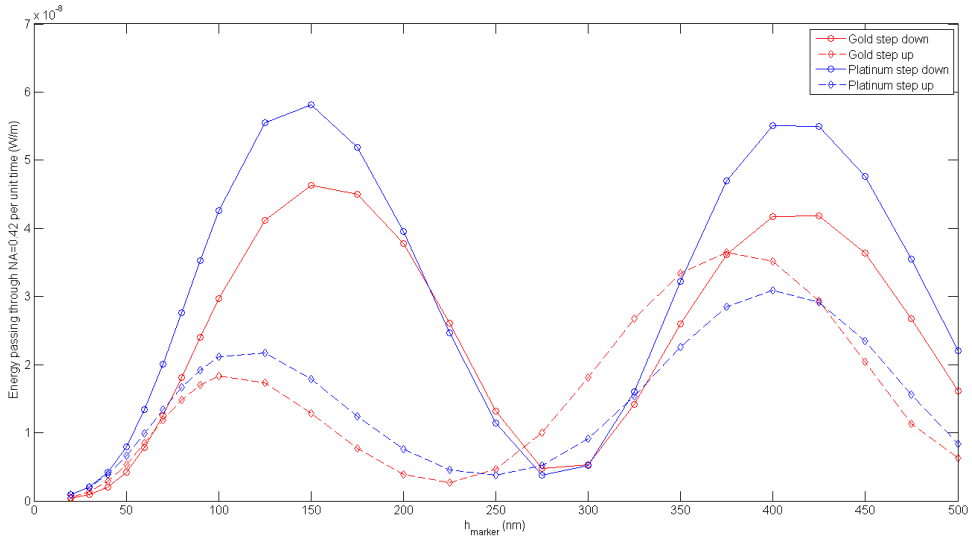

Figure 5.7: The integrated far field is plotted versus marker height, for the different corners and also for different marker materials: gold and platinum. Surprisingly, the step down corners scatter more than the step up corners.

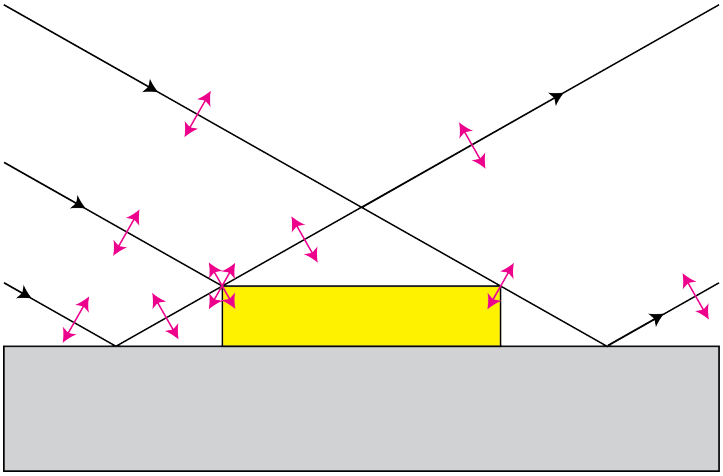

Figure 5.8: As was shown in the previous plot, the step up corner of a marker scatters less than the step down corner of the marker. This is because the electric field at the step up corner is excited in two different directions: One from the directly incoming TM-polarised wave and one from the specular reflected wave. Because these electric fields oscillate in different directions, the total electric field at the step up corner will oscillate in an 8-shape. This makes the norm of the total electric field smaller. The electric field at the step down corner however, is only excited in one direction, because this corner is shielded from waves that are specular reflected on the silicon substrate.

way: TM polarised light enters the simulation under an angle of 60°. This means that the electric field has a x- and y-component. If the light is reflected on the silicon substrate, the orientation of the electric field changes. (See Fig. 5.8) The step up corner of the marker experiences the sum of two different electric fields: One from light that directly hits the sample and the one from light that is reflected on the silicon substrate. The step down corner however only sees direct light, because the marker on its left side prevents the beam to reflect on the silicon substrate. The electric field at the step up is oscillated in two different orientation at once, while at the step down corner it is only oscillated in one direction. Therefore the norm of the electric field at the step up corner is smaller than at the step down corner.

The existence of this asymmetric scattering is confirmed with experimental results: See Fig. 5.9. These are special Rapid Nano images, because the sample is illuminated from a only single azimuth angle. The direction of the incoming light in indicated with the white arrows. It is visible that the step up edge scatters less than the step down edge.

Because the Rapid Nano normally averages the images over 9 different azimuths, the difference in scattering between step up and step down is not visible in regular RN images. Therefore the contribution of step up and step down are added, to get a straightforward number for the amount of scattering due to a marker. The results are plotted in Fig. 5.10. As a check these values are compared to the 'total' scattering due to the gold marker with different widths that was presented in Fig. 5.4. For an easy comparison, the two curves are plotted together in Fig. 5.11. The values agree quite nicely.

5.2. Minimising scattering of markers

As concluded from the COMSOL simulations in section 5.1, gold markers will scatter less into the direction of the RN detector than platinum markers, for marker heights up to 225 nm. (See Fig. 5.10) This is confirmed with experimental results: Fig. 5.12a shows Rapid Nano images of a gold marker (on the right side) and a platinum marker (on the left side). Both markers are 20 nm high. Note that these markers do not have small dots in their centre.

The simulation also predicts that, in the sub 100 nm regime, the Rapid Nano will detect less scatter from lower markers. Fig. 5.12b compares the RN images from a 50 nm high (left) and a 20 nm high (right) gold marker. At 1,00 W laser power the images from the 50 nm high marker are blurred, while the 20 nm high marker is still imaged well defined. Note that the five central dots on the 50 nm high marker are spaced more closely together than the dots on the 20 nm high marker: In the RN images they are seen as one big dot. This is the reason that the dots were spaced more widely in markers that were produced later.

As mentioned in the discussion on the marker design (section 3.3), the small dots in the centre of

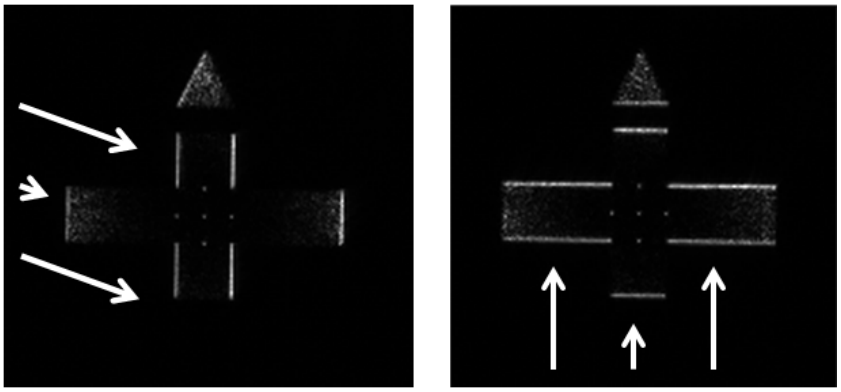

Figure 5.9: The asymmetric scattering of the step up and step down edge is confirmed in experiments. These images are made in the Rapid Nano, while the marker was illuminated from a single azimuth angle. The white arrows indicate the direction in which the incoming light hits the sample. It can be seen that the step up edge indeed scatters less than the step down edge. The plot in Fig. 5.7 shows that the difference between step up and step down is dependent on the marker height. To ensure a visible effect, these gold markers were made to be 100 nm high. To prevent saturation of the Rapid Nano detector, the shutter time was reduced to 4 ms.

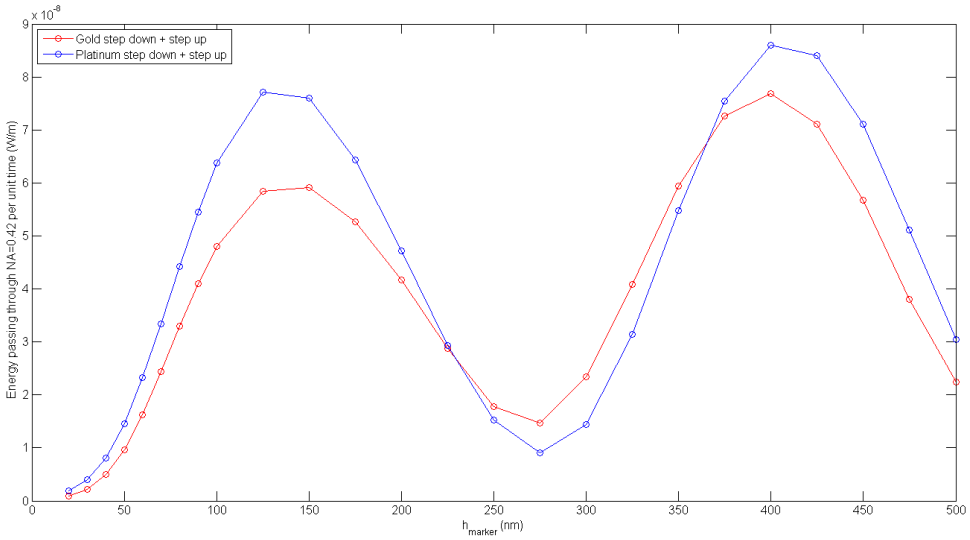

Figure 5.10: In the Rapid Nano the images are averaged over 9 different azimuth angles, so the step up and step down corners are never regarded separately. To describe the average amount of scattering on the marker edges, the contributions of step up and step down are added. Their sum is plotted in this graph. For markers up to 225 nm high, the Rapid Nano will detect less scatter from gold markers than from platinum markers. To produce a marker that scatters the least, it should be made from gold and it should be as low as possible.

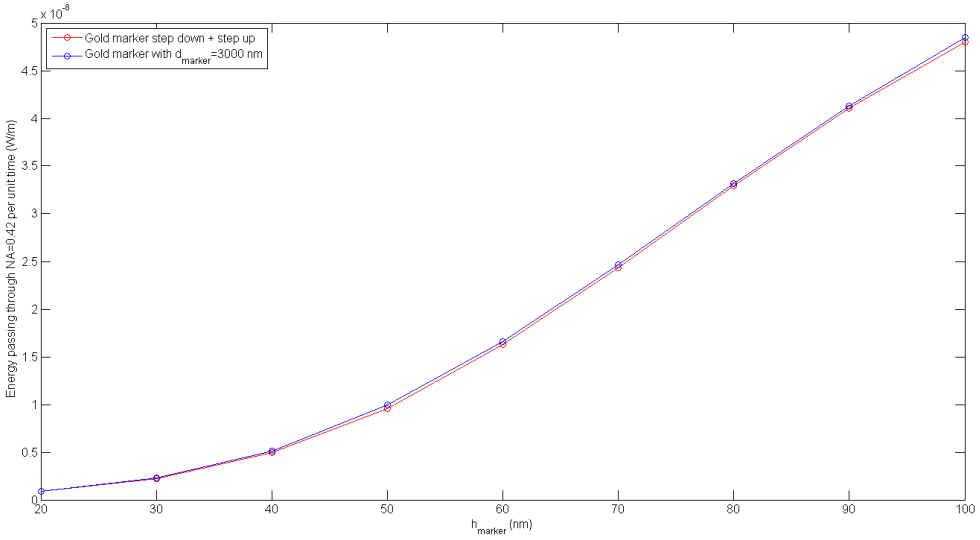

Figure 5.11: To see if the adding of the step up and step down contributions to the scattering is valid, the results from the previous plot are compared to earlier results in Fig. 5.4. In that earlier result the step up and step down corner of a less wide markers were illuminated at the same time. In this plot the summed scattering for the step up and step down corners and the total scattering from a marker of 3 micron wide are plotted. Both markers are made from gold. The results nicely match.

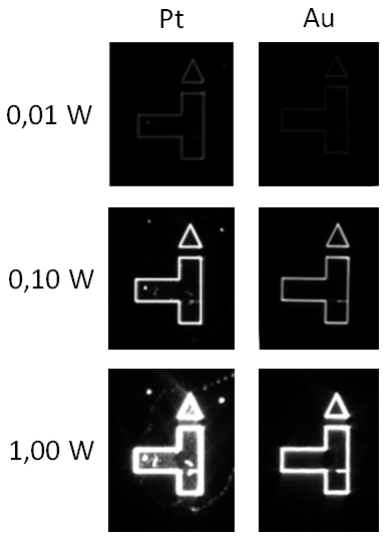

(a) Rapid Nano images of a 20 nm high platinum marker (left) and a 20 nm high gold maker (right). The gold marker scatters less than the platinum marker.

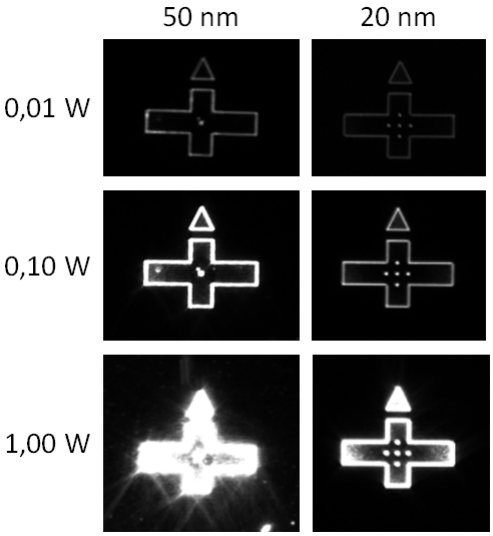

(b) Rapid Nano images of a 50 nm high gold marker (left) and a 20 nm high gold marker (right). The 20 nm high markers scatter less than the 50 nm high markers.

Figure 5.12: The conclusion from the COMSOL simulation was that the markers should be made from gold and that they should be as low as possible. These markers would scatter the least in the Rapid Nano. This conclusion is confirmed with experiments in the Rapid Nano. Here Rapid Nano images of fiducial markers from different materials and different heights are shown. The laser was operated at a power of 0.01 W, 0.10 W and 1.00 W.

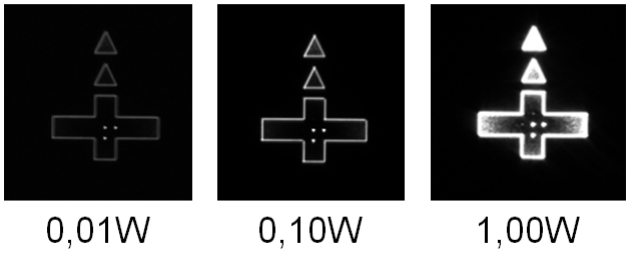

(a) Rapid Nano image.

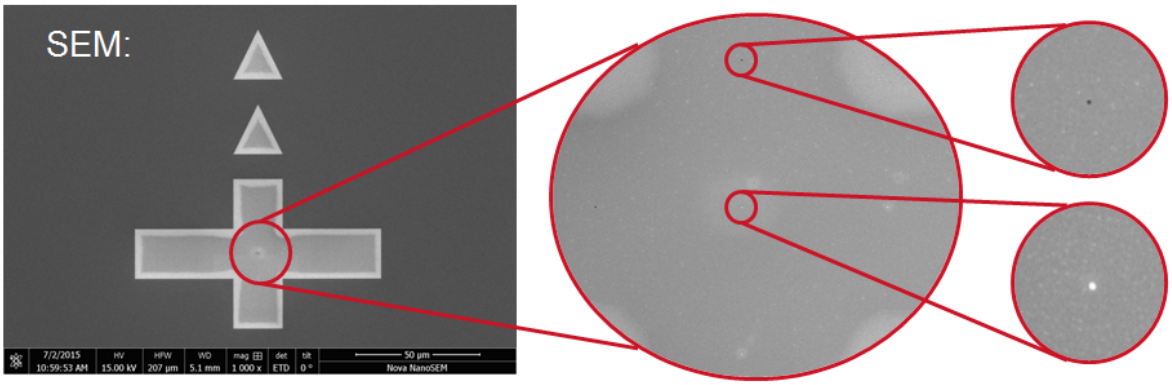

(b) Scanning electron microscope images of the same marker.

Figure 5.13: The small dots in the centre of the markers can be either pits or bumps. The scanning electron microscope images with a horizontal field width of approximately 200µm, 25µm and 4µm. These images show that 3 of the dots on the depicted marker are bumps, while the other two dots are pits. In the RN images it is visible that the bumps scatter more than the pits.

the markers are used as the reference point. They need to provide accuracy in the positioning of the marker. The AFM picture in Fig. 5.18 shows that the dots are bumps on the marker surface. A pillar of PMMA is still present under a layer of metal. Sometimes their metal “lid” of the dots is removed during the lift-off process. In that case the dot will be a pit instead of a bump. Such a pit actually scatters less in the Rapid Nano than a bump. The difference is illustrated in Fig. 5.13a. This marker contains five dots with a diameter of approximately 150 nm in its centre. In the RN images taken with a low laser power, only 3 dots are visible. At a high laser power the other two dots also become faintly visible. A SEM image of this marker (Fig. 5.13b) shows that the first three dots are bumps, while the other two are pits. The fact that pits scatter less than bumps, could be used to produce a marker that produces even less scatter in the Rapid Nano. However, it is difficult to control the removal of the metal lids during the lift-off.

5.3. Markers on imaging platforms

The markers should be easily visible and accurately localisable. In this section it is shown how the markers perform on these qualities, on all three imaging platforms.

5.3.1. Optical Dark field Microscope/Rapid Nano

Fig. 5.14 shows a marker that is imaged with the Rapid Nano. As the used laser power is increased, the amount of detected scatter also increases. However, even at 1.00 W the small dots in the centre of the marker stay well defined. Therefore the marker is visible and accurate in the Rapid Nano.

The height and material of the markers were optimised using the COMSOL simulations and experiments that were discussed in the previous sections. The marker in Fig. 5.14 is the optimised marker of 20 nm high and made from gold.

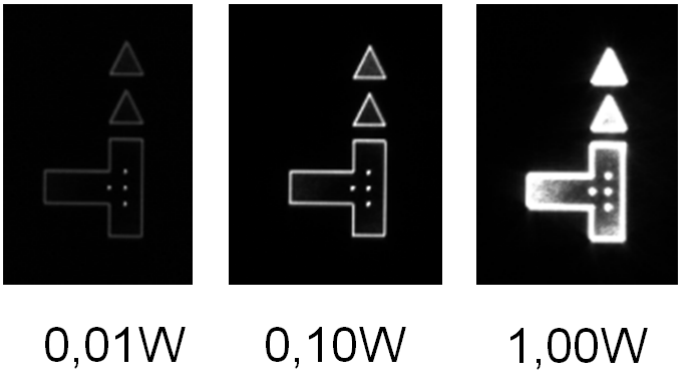

Figure 5.14: RN images of a 20 nm high gold marker. The images are made at different laser powers: 0.01 W, 0.10 W and 1.00 W. Even if the RN is operated at high power, the scatter from the marker does not saturate the CCD camera. The small dots in the centre of the marker, that are used as the reference point for the coordinate transformation, stay visible. This makes the marker easily visible and accurately localisable in the Rapid Nano.

5.3.2. Scanning Electron Microscope

5.15 shows an image of a marker, made with a scanning electron microscope. This image was made with the biggest field of view possible on this particular SEM. The ring on the outside of the image is actually the aperture of the detector. Even in this big FOV, the marker is still clearly visible. Because there are 12 markers spread across the sample, finding one of them is easy. Once a single marker is found, it will point the operator in the direction of the other markers, due to its unique shape.

The marker is also accurate: Fig. 5.16 shows zoomed in images of a marker. In this smaller FOV of a few micron, the small dots that are used as the reference point become visible.

5.3.3. Atomic Force Microscope

As discussed in chapter 3, the initial search for a marker on a blank wafer in atomic force microscopy happens with an optical microscope. Therefore the marker should also be very visible in an optical microscope. Fig. 5.17 shows an optical image of a marker. The marker is clearly visible at this large field of view and actually the small central dots on this marker are also visible at this magnification. Note that this is the first sample that was fabricated and the central dots were bigger and placed together more closely than in markers that were fabricated later. In the later markers, the small dots were no longer visible in the optical microscope.

After the marker has been found with the optical microscope, the cantilever is dropped in its vicinity and the atomic force microscope will start to scan the sample. Fig. 5.18 shows an AFM height measurement of the central dots. The small dots are clearly visible, so the height measurement can be used to accurately determine the location of the central dot.

In this AFM image it can also be seen that these dots are bumps on the surface of the markers and not pits. The PMMA is still present under the layer of gold. The dots on this marker have a diameter of approximately 500 nm. Later the diameter was reduced to approximately 150 nm.

5.4. Re-detection rate of programmed defects

As discussed in chapter 3, the re-detection rate for defects on a scanning electron microscope without a fiducial marker system is low. It is estimated that without fiducial marker system only 25% of the defects is re-detected. However, the International Technology Roadmap for Semiconductors of 2013 states that the percentage of successful re-detections should be 50% [10, Table 7]. The atomic force microscope is a slower tool than the SEM, which makes the re-detection even more challenging. Therefore it had not been attempted to re-detect defects on this platform yet.

The experiment that is described in section 4.2, is used to determine the re-detection rate of defects with a fiducial marker system. This is done on the scanning electron microscope and the atomic force microscope. During these experiments 100% of the programmed defects were re-detected on both platforms. (N=30)

Figure 5.15: Due to their big surface, the markers are easily visible in scanning electron microscope images. In a big field of view like this one, where the horizontal field width is almost 4 mm, the marker stands out against the background.

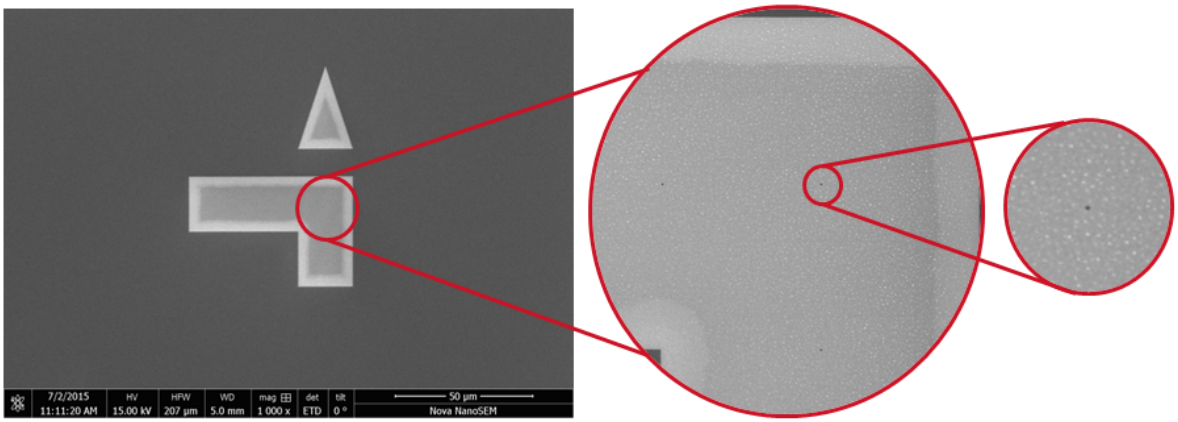

Figure 5.16: In a SEM image with a smaller FOV the small dots in the centre of the marker also become visible. Here images with a horizontal field width of approximately 200µm, 25µm and 4µm are shown. The dots have a diameter of approximately 150 nm. These small features provide the localisation accuracy that the marker needs.

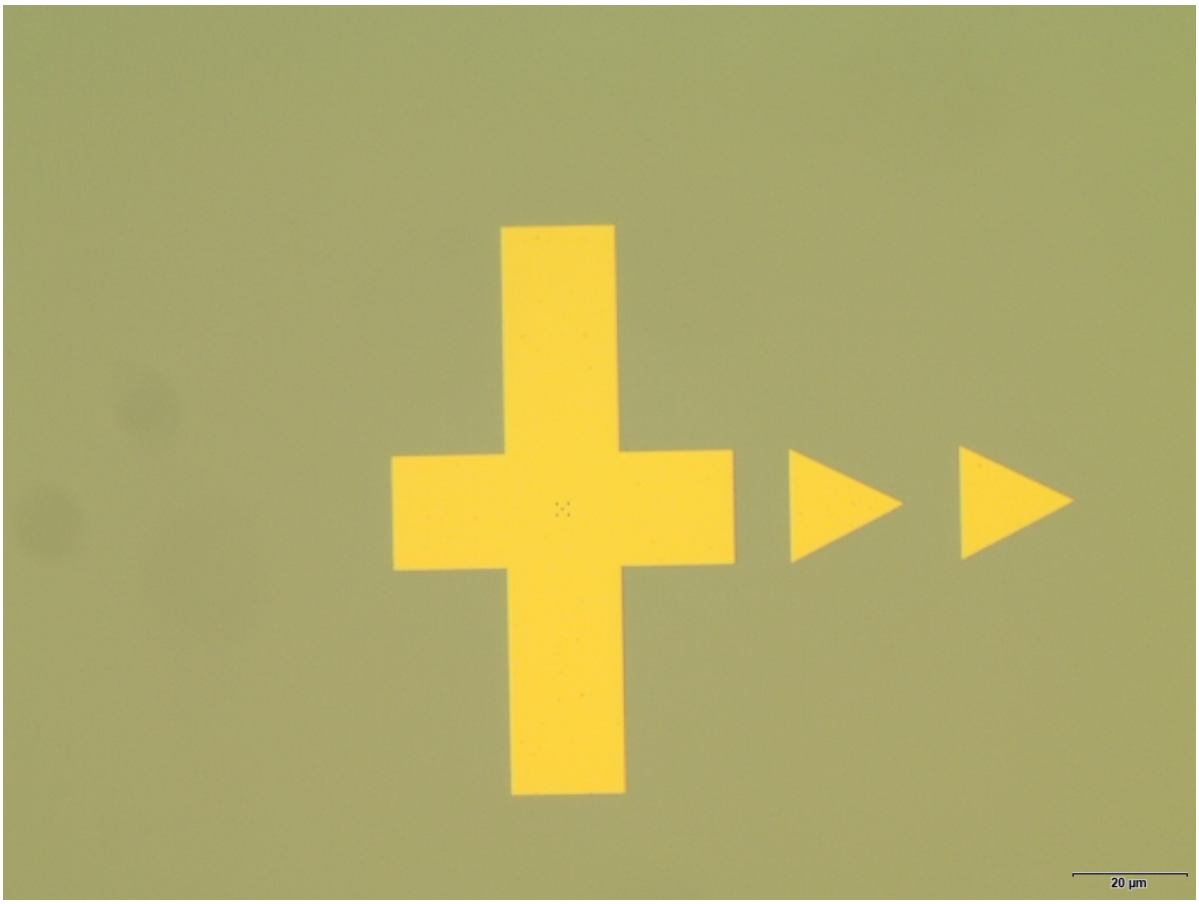

Figure 5.17: The optical microscope is used in combination with an atomic force microscope to find the markers. This image shows that thee markers are also clearly visible in an optical microscope. The five dots in the centre of this marker are also visible in this optical image. The dots on this sample are bigger and placed more close to each other than in later markers.

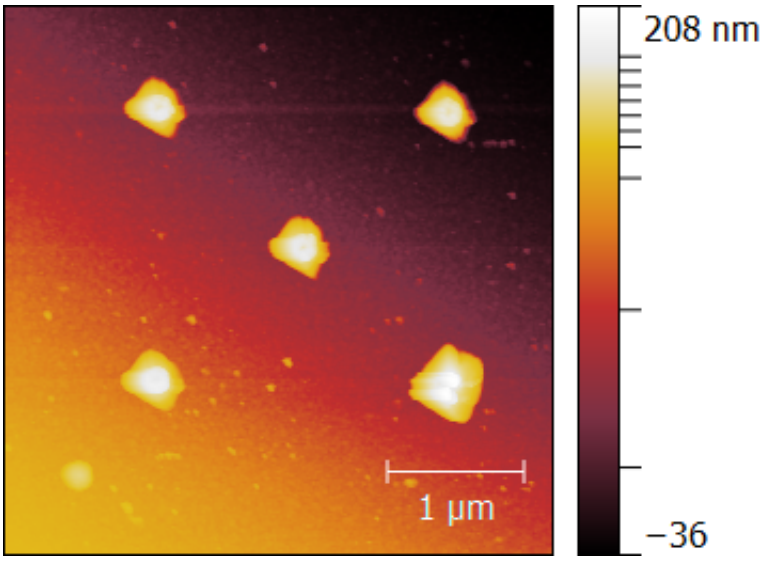

Figure 5.18: Once the markers are located with the optical microscope, the AFM tip is dropped in the vicinity of the marker and the scanning begins. This image shows an atomic force microscope height measurement of the small dots in the centre of the marker. The imaged dots lie on surface of the marker that was shown in the previous image. The position of the dots are used for the accurate localisation of the marker. The AFM was operated in tapping mode. From the height measurement it is clear that these dots are bumps on the marker surface.

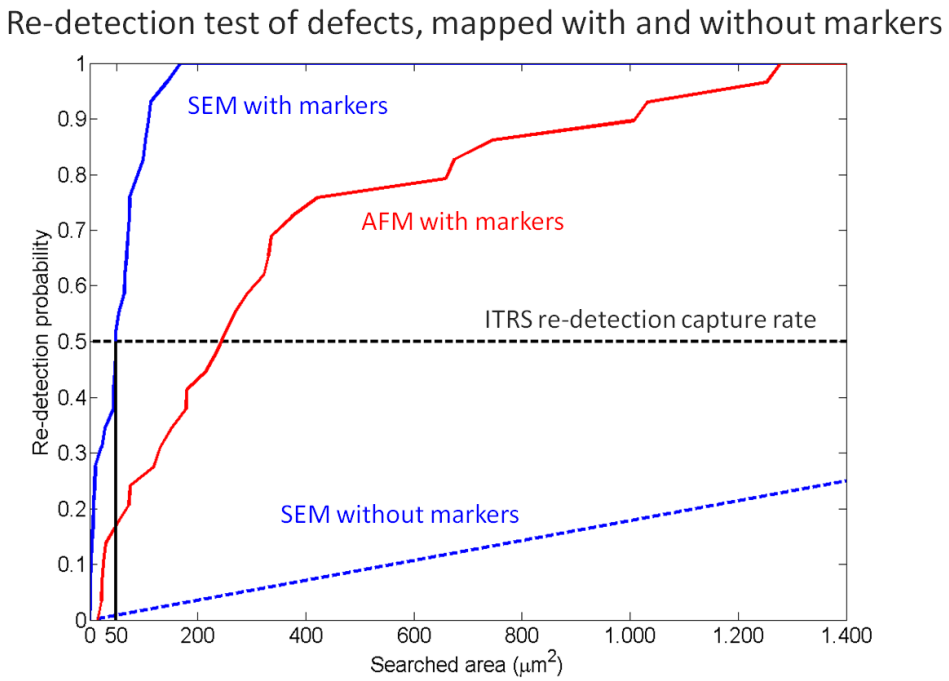

Figure 5.19: This plot shows the results of the experiments where programmed defects were re-detected in a scanning electron microscope and an atomic force microscope. The dotted lines indicate the minimum needed re-detection capture rate according to the International Technology Roadmap for Semiconductors and the estimated re-detection rate on a SEM without the fiducial marker system. The use of the fiducial marker system with the optimised 20-nm Au fiducial markers, greatly reduces the search area needed to re-detect a defect. This enhances the re-detection efficacy. It can be seen that only one standard SEM (7x7 μm^2) image per particle is needed to comply with the ITRS requirement on re-detection probability for particles down to 70 nm. The re-detection efficacy for AFM is limited in the experiments, because of a lower stage position accuracy of this particular model.

The measured distance between the predicted and real position of the defects is used to calculate the area that needs to be searched before the particle is detected, using $A = \pi \Delta r^2$. The larger the search area, the longer it takes for a defect to be re-detected. In the plot in Fig. 5.19 the percentage of re-detected particles is plotted versus this searched area. In the scanning electron microscope all the defects are found within a search area of 200 μm^2 when the fiducial marker system is used. If the slopes of the re-detection probability curves are compared, it can be concluded that the fiducial marker system improves the re-detection rate with approximately 30× on a scanning electron microscope. Note that this number is only an estimate, as there exists no real data of the re-detection of defects on blanks without a fiducial marker system.

In the plot it can be seen that the ITRS requirement of 50% re-detection is met if an area of 50 μm^2 is imaged in the SEM. This area can be imaged in a single 7×7 μm^2 SEM image. Defects need to comprise at least 10 pixels in this image to be visible. A standard SEM image is approximately 1000 pixels wide, so particles down to 70 nm would be visible in these images. Therefore only one standard SEM image per particle is needed to comply with the ITRS requirement on re-detection probability for particles down to 70 nm.

The re-detection efficacy for the atomic force microscope is lower than for the scanning electron microscope, because the AFM model that is used has a lower stage position accuracy than expected. As mentioned in section 3.1.4, it should have a repeatability of 3 μm, but the stage performs much worse. This is because the software of the machine lacks an embedded protocol to remove backslash on the stage. The stage accuracy could be improved by approaching each defect from the same x- and y-direction.

The experimental results are compared to the predicted error in the position of the defects that is calculated with the Monte Carlo Simulations in section 3.1.5. The average measured difference in the predicted and measured position of the defect on the scanning electron microscope and atomic force microscope is: $\Delta r_{\mathrm{SEM}}^{\mathrm{exp}} = 3.7 \pm 1.9$ μm and $\Delta r_{\mathrm{AFM}}^{\mathrm{exp}} = 9.4 \pm 5.2$ μm. While the average predicted difference in the simulations is: $\Delta r_{\mathrm{SEM}}^{\mathrm{sim}} = 4 \pm 0.6$ μm and $\Delta r_{\mathrm{AFM}}^{\mathrm{sim}} = 6 \pm 0.9$ μm. The predicted re-detection

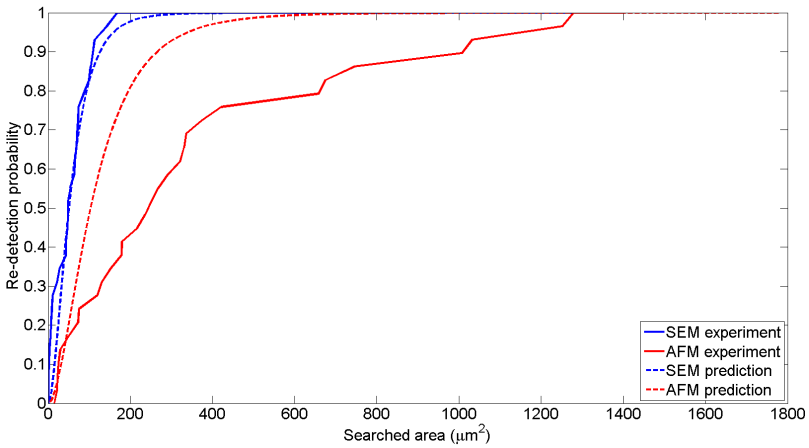

Figure 5.20: The results from the re-detection experiment are compared to the predicted values from the Monte Carlo simulation that was presented in section 3.1.5. The needed search area in the scanning electron microscope agrees with the simulation, but the atomic force microscope performs worse than expected. This is because the stage precision of the used AFM is worse than specified by the manufacturer.

probabilities from the simulation are also plotted together with the experiment results for comparison in Fig. 5.20. The results of the scanning electron microscope match quite nicely, but the AFM performs worse than expected, for the reason explained above.

5.5. Lifetime of the markers

The results from the COMSOL simulations and experiments (sections 5.1 and 5.2) show that the scatter of a marker can be reduced by decreasing the height of the marker. However, the used materials for the markers (gold and platinum) do not adhere well to a silicon substrate by themselves. Therefore an interlayer of chromium is used as a bond between the wafer and the marker. If the height of the entire marker shrinks, the available height for the interlayer also reduces. In the “low” markers of 20 nm, an interlayer of only 5 nm chromium was used. Such a thin layer of evaporated chromium does not form a closed surface. Although this layer is still sufficient for the adhesion of the gold and platinum, an unwanted consequence become visible after a couple of days: The markers start to degrade. An example is shown in 5.21. The image of this marker was made 14 days after the fabrication of the sample. This marker was initially smooth: Fig. 5.13b shows a marker on the same sample, imaged 2 days after the fabrication. But after two weeks the marker has numerous pits in its surface. This is probably caused by the porous interlayer of chromium: The gold is able to migrate through the pores into the silicon substrate.

Once the surface of the markers is covered with pits, it will cause too much scattering in the Rapid Nano. In the scanning electron microscope and the atomic force microscope the small dots in the centre of the markers become indistinguishable from the pits, so the marker system is no longer accurate. Therefore the lifetime of the marker system is limited.

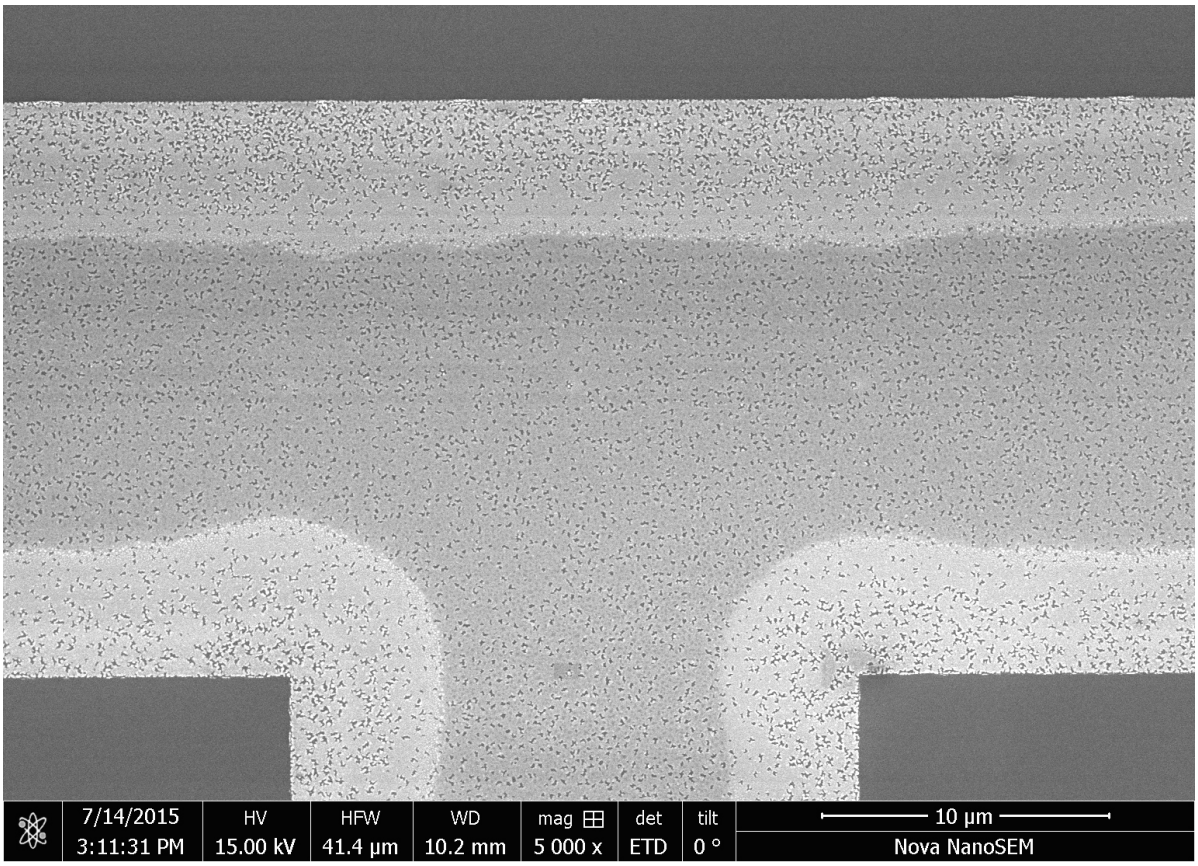

Figure 5.21: An interlayer of chromium is used to bond the gold/platinum markers to the silicon substrate. To optimise the fiducial markers, they should be as low as possible. In a very low marker the interlayer should also be thin. In this 20 nm high gold marker, an interlayer of 5 nm high was used. The thin chromium layer probably did not form a closed substrate. This enabled the gold to migrate through the pores in the interlayer. This scanning electron image was made two weeks after the fabrication of the sample. Many pits have appeared in the marker surface, making the marker unusable.

6

Conclusions & recommendations

In this final chapter, the conclusions of this Master thesis are presented. As discussed in the introduction, Chapter 1, the research objective of this Master thesis was to design, fabricate and validate a fiducial marker system for blanks. In the following sections, these three steps are discussed one by one. Some recommendations to further improve the fiducial marker system are also made. The final section 6.4 discusses a possible application of an effect that was discovered with the finite element model that was made in this thesis.

6.1. Design

A fiducial marker design was created that combines a big marker surface with small features, to provide both visibility *and* positioning accuracy in all three platforms: TNO's Rapid Nano, a scanning electron microscope and an atomic force microscope.

12 of these fiducial markers are spread across the blank wafer. Each marker has a unique shape, so they can be distinguished from one another. The design of the markers provides information about the position and orientation of the marker at a glance. Once a single marker is found, it is easy to locate the other markers.

The design for the fiducial marker system meets the requirements on size, shape and location of the markers.

In order to reduce the scattering of the fiducial markers in the Rapid Nano, the material and height of the markers were optimised within the established requirements. This was done using finite element simulations (COMSOL) and experiments. From these simulations and experiments, it can be concluded that low, gold makers scatter less than markers from platinum and higher markers.

The optimised markers are very visible in bright field, but almost invisible ("stealth") in optical dark field, the used microscopy mode in the Rapid Nano.

6.2. Fabrication

The fiducial markers were fabricated with e-beam lithography, evaporation of gold and lift off.

Unfortunately, the results of the lift off are inconstant and very dependent on the skills of the person performing the lift off. Metal that is not properly removed during the lift off, contaminates the blank. Because the Rapid Nano uses a pre- and a post-scan, this contamination is not included in the resulting defect map. However, the lift off contamination scatters a lot in the Rapid Nano: It frequently saturates the detector. If the Rapid Nano is operated at full laser power, the lift off residues can possibly shield "real" contamination that lies close to the lift off contamination from being detected. The Rapid Nano could be operated at a lower laser power to prevent the saturation, but then the smaller particles remain undetected. It is concluded that the current marker system does not meet the requirement on contamination of the blank.

The requirement on the used material is also not fulfilled: The fabricated markers are made from gold and platinum. Both materials are not compliant with processes that are used in the semi-conductor industries.

The final point of improvement for the fiducial marker system is the lifetime of the markers: To minimise the scatter from the markers, they should be as low as possible. However, in the current design of the marker an interlayer of chromium is needed for the gold to properly adhere to the silicon substrate. If this layer of chromium is too thin, i.e. only 5 nm, it will not form a closed surface. This enables the gold to migrate through the chromium layer into the silicon substrate, causing pits in the surface of the marker. The resulting rough surface increases the amount of scattering of the marker in the Rapid Nano, making the marker system unusable within 14 days.

In a next design for the fiducial marker system, lift off should be avoided as a fabrication method. It proved very difficult to find a suitable material for the markers that can be used in tools from the semiconductor industry. Therefore it should also be investigated if the markers are still visible enough in optical and scanning electron microscopes if the contrast between the marker and the silicon substrate is only provided by topographical contrast. In this case, no “prohibited” material has to be used and the lifetime of the fiducial marker system would improve at the same time.

6.3. Validation

The functioning of the fiducial marker system was validated by re-detecting programmed defects that have been mapped by the Rapid Nano. The fiducial marker system greatly enhanced the re-detection rate of defects. Without fiducial marker system a re-detection rate of 50% is considered challenging, but in the experiments with the fiducial marker system 100% of the programmed defects were re-detected on both platforms.

The experimental results on the scanning electron microscope are in agreement with the results from Monte Carlo simulations on the propagation of inaccuracy in the position of markers/defects. The atomic force microscope performed worse than expected, because the stage precision in the used AFM model is worse than specified by the manufacturer.

6.4. Asymmetric scattering in the Rapid Nano

During the finite element analysis in COMSOL, a peculiar property of the scattering in the Rapid Nano was discovered: Two opposing edges of a fiducial marker scatter differently. This asymmetry was confirmed with experimental data, which partially validates the finite element model.

This discovery could potentially be used for advanced defect classification in the Rapid Nano. E.g. the height or aspect ratio of a defect could be determined in the Rapid Nano, without the need for further inspection in a different tool. A 3D finite element model and further experiments in the Rapid Nano could be used to research the feasibility of this application.

A

errorpropagation.mat

```
close all;
clear all;
clc;

%% PARAMETERS TO CHANGE:
% number of simulations to run
numsim = 100;

% Standard deviations in measurements
sigma_RN = 0.001;    % [mm]
sigma_SEM = 2e-6;    % [m]

% Markers used to span vectorspace
a = 1;            % Choose from: 1, 4, 6, 9 and 12. (SEM pictures from 23/03/2015)
b = 9;
c = 12;


%% Importing data from real RN, SEM and AFM measurements + gaussian error
% Creating meshgrid for 2D plot
[X,Y] = meshgrid(110:0.1:160,-150:0.1:-100);      % In RN coordinates (made right-handed)

% Creating empty matrices to increase speed
x_RN_marker = zeros(1,12);
y_RN_marker = zeros(1,12);
x_SEM_marker = zeros(1,12);
y_SEM_marker = zeros(1,12);
SEM_particle = zeros(3,numsim);
x_RN_particle = zeros(size(X,1),size(X,2),numsim);
y_RN_particle = zeros(size(X,1),size(X,2),numsim);
x_SEM_particle = zeros(size(X,1),size(X,2),numsim);
y_SEM_particle = zeros(size(X,1),size(X,2),numsim);
error_x_particle_SEM = zeros(size(X,1),size(X,2));
error_y_particle_SEM = zeros(size(X,1),size(X,2));
error_particle_SEM = zeros(size(X,1),size(X,2));
markerplot1 = ones(1,12);
markerplot2 = ones(1,3);


for i=1:numsim
    % RN markers [mm]
x_RN_marker(1) = 149.613 + normrnd(0,sigma_RN);
x_RN_marker(2) = 148.829 + normrnd(0,sigma_RN);
x_RN_marker(3) = 148.029 + normrnd(0,sigma_RN);
x_RN_marker(4) = 147.230 + normrnd(0,sigma_RN);
x_RN_marker(5) = 139.654 + normrnd(0,sigma_RN);
x_RN_marker(6) = 138.861 + normrnd(0,sigma_RN);        % Markers Sample 01.
x_RN_marker(7) = 138.063 + normrnd(0,sigma_RN);
```

```
49 x_RN_marker(8) = 137.267 + normrnd(0,sigma_RN);
50 x_RN_marker(9) = 129.697 + normrnd(0,sigma_RN);
51 x_RN_marker(10) = 128.890 + normrnd(0,sigma_RN);
52 x_RN_marker(11) = 128.094 + normrnd(0,sigma_RN);
53 x_RN_marker(12) = 127.298 + normrnd(0,sigma_RN);
54
55 y_RN_marker(1) = -138.919 + normrnd(0,sigma_RN);
56 y_RN_marker(2) = -128.957 + normrnd(0,sigma_RN);
57 y_RN_marker(3) = -118.990 + normrnd(0,sigma_RN);
58 y_RN_marker(4) = -109.023 + normrnd(0,sigma_RN);
59 y_RN_marker(5) = -139.723 + normrnd(0,sigma_RN);       % Y coordinates are taken as ...
       negative to make RN coordinates right-handed.
60 y_RN_marker(6) = -129.758 + normrnd(0,sigma_RN);
61 y_RN_marker(7) = -119.787 + normrnd(0,sigma_RN);
62 y_RN_marker(8) = -109.820 + normrnd(0,sigma_RN);
63 y_RN_marker(9) = -140.512 + normrnd(0,sigma_RN);
64 y_RN_marker(10) = -130.553 + normrnd(0,sigma_RN);
65 y_RN_marker(11) = -120.584 + normrnd(0,sigma_RN);
66 y_RN_marker(12) = -110.617 + normrnd(0,sigma_RN);
67
68 % RN particles [mm]
69 x_RN_particle(:,:,i)=X+normrnd(0,sigma_RN,[size(X,1),size(X,2)]);
70 y_RN_particle(:,:,i)=Y+normrnd(0,sigma_RN,[size(X,1),size(X,2)]);
71
72 % SEM markers [m]
73 x_SEM_marker(1) = 0.0100152 + normrnd(0,sigma_SEM);        % Data from SEM pictures taken ...
       on 23/03/2015
74 x_SEM_marker(4) = 0.00951667 + normrnd(0,sigma_SEM);
75 x_SEM_marker(6) = -0.000145847 + normrnd(0,sigma_SEM);
76 x_SEM_marker(9) = -0.009966 + normrnd(0,sigma_SEM);
77 x_SEM_marker(12) = -0.0104906 + normrnd(0,sigma_SEM);
78 y_SEM_marker(1) = -0.0145448 + normrnd(0,sigma_SEM);
79 y_SEM_marker(4) = 0.0154331 + normrnd(0,sigma_SEM);
80 y_SEM_marker(6) = -0.004730226 + normrnd(0,sigma_SEM);
81 y_SEM_marker(9) = -0.014899 + normrnd(0,sigma_SEM);
82 y_SEM_marker(12) = 0.0150891 + normrnd(0,sigma_SEM);
83
84
85 %% Finding transformation matrix T using marker coordinates
86 % SEM
87 M = [x_RN_marker(a) y_RN_marker(a) 1 0 0 0; ...
88      0 0 0 x_RN_marker(a) y_RN_marker(a) 1; ...
89      x_RN_marker(b) y_RN_marker(b) 1 0 0 0; ...
90      0 0 0 x_RN_marker(b) y_RN_marker(b) 1; ...
91      x_RN_marker(c) y_RN_marker(c) 1 0 0 0; ...
92      0 0 0 x_RN_marker(c) y_RN_marker(c) 1];
93
94 u_SEM = [x_SEM_marker(a); y_SEM_marker(a); x_SEM_marker(b); y_SEM_marker(b); ...
       x_SEM_marker(c); y_SEM_marker(c)];
95 v_SEM = M\u_SEM;
96 T_SEM = [reshape(v_SEM,3,2)';0 0 1];
97
98
99 %% Finding location of the particle from RN coordinates
100 for k=1:size(X,1)
101     for l=1:size(X,2)
102         SEM_particle = T_SEM*[x_RN_particle(k,l,i); y_RN_particle(k,l,i); 1];
103         x_SEM_particle(k,l,i) = SEM_particle(1);
104         y_SEM_particle(k,l,i) = SEM_particle(2);
105     end
106 end
107 end
108
109 %% Calculating standard deviation in particle location
110 for k=1:size(X,1)
111     for l=1:size(X,2)
112         % SEM [m]
113         error_x_particle_SEM(k,l) = sqrt(std(x_SEM_particle(k,l,:))^2 + sigma_SEM^2);
114         error_y_particle_SEM(k,l) = sqrt(std(y_SEM_particle(k,l,:))^2 + sigma_SEM^2);
115         error_particle_SEM(k,l) = ...
              sqrt(error_x_particle_SEM(k,l)^2+error_y_particle_SEM(k,l)^2);
```

```
116         end
117     end
118
119     three_sigma_SEM = 3.*error_particle_SEM;
120
121     %% 2D error plot
122
123     figure()
124     surf(X,Y,three_sigma_SEM,'EdgeColor','None');
125     hold on
126     % Make markers visible
127     scatter3(x_RN_marker,y_RN_marker,markerplot1*max(max(three_sigma_SEM)),'ks','filled')
128     scatter3([x_RN_marker(a) x_RN_marker(b) x_RN_marker(c)],[y_RN_marker(a) y_RN_marker(b) ...
            y_RN_marker(c)],markerplot2*max(max(three_sigma_SEM)),'ws','filled')
129     view(2);
130     xlabel('RN x coordinate (mm)')
131     ylabel('RN y coordinate (mm)')
132     colorbar
133     box on
134     title('3 \sigma number in position of particle in SEM')
```

B

Clean room recipes

The following recipes and settings were used for the fabrication of the fiducial marker system.

B.1. Resist

A double layer of *Polymethyl methacrylate* (PMMA) is used as resist for the e-beam lithography. The following recipe is used:

1. The first layer consists of PMMA with a molecular weight of 495k, that is diluted in 4% anisole (PMMA 495 4A). It is baked for 10 minutes directly after the spin coating.
2. The second layer consists PMMA 950 A3 and is baked for an additional 15 minutes.

Both layers are spin coated at 4000 rpm and baked on a hot plate at a temperature of 175°C.

B.2. E-beam lithography

The e-beam lithography is performed with Vistec's EBPG5000plus Electron-Beam Lithography System. The design is defined in a GDSII file that contains three separate layers. Table B.1 gives the settings that were used in the writing of each layer.

Table B.1: Used settings for the layers in the e-beam lithography pattern.

Structures on layer	**Dose (μC/cm^2)**	**Resolution and Beam Step Size (nm)**
Large area of the fiducial markers	1500	10
Small dots in centre of the marker	50000	4
Programmed defects	1500	5

B.3. Development

After the e-beam lithography the resist is developed in:

1. 4-methyl-2-pentanone (MIBK) with 2-propanol (IPA) diluted 1:3, for 60 seconds.
2. IPA, for 30 seconds.

B.4. Lift off

After the metal evaporation, lift off is performed in:

1. Acetone that is heated to 54°C for 2 hours.
2. An additional 5-6 hours in the same acetone that is taken out of the heat bath.

During the lift off the glassware should be covered with aluminium foil, to prevent the acetone from evaporating. To aid in the lift off the sample can be sonicated, or a syringe can be used to flow acetone over the surface sample. The sample should not be dried before all the gold has lifted off.

Bibliography

[1] P.A. Bobbert and J. Vlieger. Light scattering by a sphere on a substrate, 1986. ISSN 03784371.

[2] P.A. Bobbert, J. Vlieger, and R. Greef. Light reflection from a substrate sparsely seeded with spheres - comparison with an ellipsometric experiment, 1986. ISSN 03784371.

[3] Tom Boettiger, Peter Buck, Sankaranarayanan Paninjath, Mark Pereira, Rob Ronald, Dan Rost, and Bhamidipati Samir. Automatic classification of blank substrate defects. 9235:92351J, 2014. doi: 10.1117/12.2069678. URL http://proceedings.spiedigitallibrary.org/proceeding.aspx?doi=10.1117/12.2069678.

[4] Don Clark. Intel Rechisels the Tablet on Moore's Law. *Wall Street Journal Digits Tech News and Analysis*. URL http://blogs.wsj.com/digits/2015/07/16/intel-rechisels-the-tablet-on-moores-law/.

[5] Comsol. COMSOL v5.0 Wave Optics Module User's Guide, 2014.

[6] Comsol. Introduction to the Wave Optics Module, 2014.

[7] a. J. Cox, Alan J. DeWeerd, and Jennifer Linden. An experiment to measure Mie and Rayleigh total scattering cross sections. *American Journal of Physics*, 70(6):620, 2002. ISSN 00029505. doi: 10.1119/1.1466815.

[8] Stéphane Cuenot, Christian Frétigny, Sophie Demoustier-Champagne, and Bernard Nysten. Surface tension effect on the mechanical properties of nanomaterials measured by atomic force microscopy. *Physical Review B*, 69(16):1–5, 2004. ISSN 1098-0121. doi: 10.1103/PhysRevB.69.165410.

[9] David Jeffrey Griffiths and Reed College. *Introduction to electrodynamics*, volume 3. prentice Hall Upper Saddle River, NJ, 1999.

[10] International Technology Roadmap for Semiconductors. Yield Enhancement, 2013.

[11] Jung Hyeun Kim, Sheryl H Ehrman, and George W Mulholland. Polarized light scattering from metallic particles on silicon wafers. In *Proc. SPIE 4449*, volume 290, pages 281–290, 2001. doi: 10.1117/12.450105. URL http://physics.nist.gov/Divisions/Div844/publications/germer/SPIE4449-39.pdf.

[12] Patrick D. Kinney and Yuri Uritsky. Locating defects on wafers for analysis by SEM/EDX, AFM, and other microanalysis techniques. *Proceedings of SPIE*, 3509:204–209, 1998. ISSN 0277786X. doi: 10.1117/12.324413. URL http://proceedings.spiedigitallibrary.org/proceeding.aspx?articleid=965356.

[13] Fatima H Labeed and Henry O Fatoyinbo. *Microfluidics in Detection Science*. RSC Detection Science. The Royal Society of Chemistry, 2014. ISBN 978-1-84973-638-1. doi: 10.1039/9781849737609. URL http://dx.doi.org/10.1039/9781849737609.

[14] Sheng S Li. *Semiconductor physical electronics*. Springer Science & Business Media, 2012.

[15] Stuart Lindsay. *Introduction to nanoscience*. OUP Oxford, 2009.

[16] Marc J Madou. *Fundamentals of microfabrication: the science of miniaturization*. CRC press, 2002.

[17] Gordon E. Moore. Cramming more components onto integrated circuits. *Proceedings of the IEEE*, 86(1):82–85, 1998. ISSN 00189219. doi: 10.1109/JPROC.1998.658762.

[18] NIST. SCATMECH: Polarized Light Scattering C++ Class Library. URL http://pml.nist.gov/Scatmech/html/index.htm.

[19] a. Okamoto, H. Kuniyasu, and T. Hattori. Detection of 30&40-nm Particles on Bulk-Silicon and SOI Wafers Using Deep UV Laser Scattering. *IEEE Transactions on Semiconductor Manufacturing*, 19(4):372–380, 2006. ISSN 0894-6507. doi: 10.1109/TSM.2006.884600.

[20] M. N. Polyanskiy. Refractive index database. URL http://refractiveindex.info/.

[21] David M Pozar. *Microwave engineering*. John Wiley & Sons, 2009.

[22] Christophe J. Roudin, Patrick D. Kinney, and Yuri S. Uritsky. New sample preparation method for improved defect characterization yield on bare wafers. In *SPIE 3884*, 1999. doi: 10.1117/12.361331. URL http://proceedings.spiedigitallibrary.org/proceeding.aspx?articleid=912759.

[23] S Roy, A C Assafrão, S F Pereira, and H P Urbach. Coherent Fourier scatterometry for detection of nanometer-sized particles on a planar substrate surface. *Optics express*, 22(11):304–313, 2014. ISSN 10944087. doi: 10.1364/OE.22.013250. URL http://www.opticsinfobase.org/oe/fulltext.cfm?uri=oe-22-11-13250&id=286502.

[24] S Roy, K Ushakova, Q. van den Berg, S F Pereira, and H P Urbach. Radially Polarized Light for Detection and Nanolocalization of Dielectric Particles on a Planar Substrate. *Physical Review Letters*, 114(10):103903, 2015. doi: 10.1103/PhysRevLett.114.103903.

[25] Phil Russell, Dale Batchelor, and John Thornton. SEM and AFM : Complementary Techniques for High Resolution Surface Investigations. *Veeco Instruments Inc.*, pages 9–12, 2001.

[26] Heiko Stegmann. Voltage Contrast in Microelectronic Engineering, 2013.

[27] M Stepanova and S Dew. *Nanofabrication: Techniques and Principles*. SpringerLink : B{ü}cher. Springer Vienna, 2011. ISBN 9783709104248. URL https://books.google.nl/books?id=ZEPzoCZ8xegC.

[28] J. K. Stortelder, J. C. J. van der Donck, S. Oostrom, P. van der Walle, O. Brux, and P. Dress. Particle qualification procedure for the TNO EUV reticle load port module of the HamaTech MaskTrackPro cleaning tool. *SPIE Advanced Lithography*, 7969:79691Q, 2011. ISSN 0277786X. doi: 10.1117/12.879370. URL http://spiedigitallibrary.org/proceeding.aspx?doi=10.1117/12.879370.

[29] Jacques van der Donck, Rob Snel, Jetske Stortelder, Alfred Abutan, Sjoerd Oostrom, Sander van Reek, Bert van der Zwan, and Peter van der Walle. Particle detection on flat surfaces. In *Proc. of SPIE*, volume 7969, 2011. doi: 10.1117/12.879435. URL http://spiedigitallibrary.org/proceeding.aspx?doi=10.1117/12.879435.

[30] Peter Van der Walle, Pragati Kumar, Dmitry Ityaksov, Richard Versluis, Diederik J Maas, Jochem Janssen, and Jacques C J Van Der Donck. Increased particle inspection sensitivity by reduction of background scatter variance. *SPIE 8681*, 8681(April):1–6, 2013. ISSN 0277786X. doi: 10.1117/12.2011092.

[31] Peter van der Walle, Sandro Hannemann, Daan van Eijk, Wouter Mulckhuyse, and Jacques C. J. van der Donck. Implementation of background scattering variance reduction on the rapid nano particle scanner. In *SPIE 9050, Metrology, Inspection, and Process Control for Microlithography XXVIII, 905033*, number April, 2014. doi: 10.1117/12.2048684. URL http://proceedings.spiedigitallibrary.org/proceeding.aspx?doi=10.1117/12.2048684.

[32] Gorden Videen. Light scattering from a sphere on or near a surface, 1991. ISSN 1084-7529.

[33] Ch Wong, P. E. West, K. S. Olson, M. I. Mecartney, and N. Starostina. Tip dilation and AFM capabilities in the characterization of nanoparticles. *Jom*, 59(1):12–16, 2007. ISSN 10474838. doi: 10.1007/s11837-007-0003-x.

[34] Andrew T Young. Rayleigh scattering. *Physics Today*, 35(January):42–48, 1982. ISSN 00319228. doi: 10.1063/1.2890003.